**Creating a Multi-Model Artificial Intelligence Framework to Predict the Operational Availability of a Laboratory-Scale Ship Machinery Plant**

by

Stephen A. Olson

A dissertation submitted in partial fulfillment
of the requirements for the degree of
Doctor of Philosophy
(Naval Architecture and Marine Engineering)
in the University of Michigan
2024

Doctoral Committee:

Professor of Practice Timothy J. McCoy, Co-Chair
Professor Matthew D. Collette, Co-Chair
Associate Professor Branko Kerkez
Associate Professor David Singer

Stephen A. Olson
olsonsao@umich.edu
ORCID iD: 0009-0004-5062-8346

In memory of my grandfather:

**Gerald J. McDonald**

1937-2023

# ACKNOWLEDGEMENTS

I would like to thank the Office of Naval Research for funding and technical guidance under grant N00014-21-1-2795 directed by Dr. Paul Hess and Dr. Jessica Dibelka. I would like to thank my research advisors and dissertation committee co-chairs Professor of Practice Timothy McCoy and Professor Matthew Collette for providing me with this opportunity and the invaluable guidance along the way. The fulfillment of this PhD would not have been possible without their continuous support and expert field knowledge. They both have had a critical role in shaping the student, researcher, engineer and professional I am today. I am forever grateful for their guidance over the last four years. I would also like to thank my dissertation committee members Professor Branko Kerkez and Professor David Singer. Their perspective and advice was a crucial contributor to the success of this research and the rounded experience I was able to achieve throughout my time at Michigan. I would like to thank the undergraduate and graduate students who worked in the laboratory to support the build and data acquisition processes. The support of the students across the past four years had a significant role in the completion of the hardware laboratory systems and in the acquisition of laboratory data.

Finally, I would like to say thank you to my family. Mom and Dad, I know that everything you do has made achievements like this possible, and I can't say thank you enough for all your support along the way. Ericka, I couldn't ask for a better partner in life, and I appreciate everything you've done to support me over the last four years. I love you all very much.

# TABLE OF CONTENTS

# LIST OF FIGURES

FIGURE

# LIST OF TABLES

TABLE

# LIST OF ABBREVIATIONS

**RTF** Run to Failure

**MEL** Marine Engineering Laboratory at the University of Michigan

**RUL** Remaining Useful Life

**SOH** State of Health

**MLSMP** University of Michigan Laboratory-scale Ship Machinery Plant

**VFD** Variable Frequency Drive

**RUL** Remaining Useful Life

**AI** Artificial Intelligence

**ML** Machine Learning

**DT** Digital Twin

**RTF** Run to Failure

**SISO** Single Input Single Output (control loop)

**LSTM** Long Short-term Memory

**MSB1** Main Switchboard 1

**MSB2** Main Switchboard 2

**SSB1** Secondary Switchboard 1

**SSB1** Secondary Switchboard 2

**WOT** Wide Open Throttle

# ABSTRACT

In interests of autonomous and unmanned operation of seagoing vessels by both commercial entities and the United States Government, significant research has been conducted for safe navigation and cybersecurity. This research has contributed to the reduction of required onboard personnel. However, research directed toward reducing required underway personnel ensuring reliable operation of shipboard machinery systems is limited. Machinery reliability has become a primary restriction for unmanned and autonomous operation. Due to complexities driven by plant machinery size and inter-connectivity of systems, traditional methods for improved reliability such as redundancy and component design for high reliability are insufficient to provide necessary reliability for achieving unmanned and autonomous operation of vessel machinery plants over desired duration of deployment. Given the inability to address component faults and failures, a need exists to focus research efforts on operational resilience, or the ability to continue operation in fault prone and present environments.

To improve operational resilience, this work proposes use of Artificial Intelligence (AI) to perform prognostics and diagnostics on plant machinery systems to understand state of health and predict vessel operational availability. With knowledge of system capabilities until failure, fault mitigation techniques may be employed. These techniques include modification to mission operations or more complex applications such as control based fault mitigation to maintain operational capabilities. Heretofore, research for ship machinery system prognostics and diagnostics have been focused at component and subsystems levels to acquire input data from hardware. Applications of prognostics and diagnostics at the system level are prevalent in literature in instances with input data obtained from software simulation models of hardware systems. Due to the lack of hardware based failure data, prognostics and diagnostics of ship machinery plants is largely unexplored. In this work, a laboratory scale ship machinery plant (MLSMP) is designed, constructed and leveraged to obtain lacking run to failure (RTF) data. The MLSMP consisted of a cooling system, fuel system, emulated diesel generator sets, energy storage system, electrical system, mission system, propulsion system, and real time control and data acquisition system. The MLSMP was used to obtain 100 RTF profiles for common faults and failures of machinery systems and illustrate three potential control mitigation strategies for the fault prone environment.

The constructed dataset served as input data to explore potential AI models, including the selected Long Short-term Memory (LSTM) Recurrent Neural Network (RNN) model. These models aimed to detect individual system failures and predict when a system would fail to support operational mission demands, which are utilized to create a multi-model prediction algorithm for the MLSMP. The developed plant-level algorithm is tested and evaluated using the 100 RTF profiles to demonstrate successes and predict accuracy concerning input parameter selection. The LSTM model performed well in the diagnostic and prognostic tasks for the cooling system. The models performed well for the more complex fuel system, although errors increased as system complexity increased.

Efforts under this PhD research provide a significant step towards the operation of unmanned and autonomous operation of ship machinery plants. These efforts include the construction of a laboratory based ship machinery plant, obtaining run to failure data for the laboratory based plant, constructing and evaluating an LSTM driven multi-model framework for prognostics and diagnostics of the MLSMP, and showcasing the potential for unconventional control methods to maintain operational availability in the presence of machinery system faults.

# CHAPTER 1

# Introduction

Autonomous and unmanned operation of marine surface vessels is of significant interest to both commercial entities and the United States Government. Benefits driving the desire for autonomous and unmanned operation include a reduction in operational cost, improved safety, reduced emissions, and expansion of platform mission capabilities. Current research for autonomous and unmanned vessel operation has primarily focused on safe navigation and cybersecurity to enable the reduction of onboard personal. However, the importance of machinery plants capable of reliable operation in the absence of human intervention has received limited attention and remains a largely unexplored area [4]. Vessel machinery plants consist of several interconnected and interdependent systems to achieve the functionality required to support mission demands (propulsion loads, hotel loads, communication, etc.). Components within these systems degrade throughout their service life and many components requiring frequent preventative and corrective maintenance within a single deployment period by onboard personnel.

Due to the complexity driven by plant machinery size and inter-connectivity of systems, traditional methods for improved reliability such as redundancy and component design for high reliability, are insufficient in providing the necessary reliability to achieve unmanned and autonomous operation of vessel machinery plants over the desired long duration of deployment. Provided with the inability to remove component faults and failures, this work proposes a focus on operational resilience, or the ability to continue operation in a fault prone and present environment. To improve operational resilience, in the interest of unmanned and autonomous operations, this work proposes the use of artificial intelligence (AI), with the selection of a long short-term memory (LSTM) Recurrent Neural Network (RNN), to perform prognostics and diagnostics on plant machinery systems to understand and predict vessel operational availability. Provided with knowledge of system capability until failure, fault mitigation techniques can be employed. Basic techniques may include modifying mission operations or adjusting deployment periods to allow for preventative and corrective mainte-

nance. Advanced techniques may include the use of adaptive real time control of machinery plant systems to mitigate faults and maintain operational capabilities.

Efforts under this PhD research provide a significant step towards the operation of unmanned and autonomous operation of ship machinery plants. These efforts include the construction of a laboratory based ship machinery plant, obtaining run to failure data for the laboratory based plant, constructing and evaluating an LSTM driven multi-model framework for prognostics and diagnostics of the laboratory based machinery plant, and showcasing the potential for unconventional control methods to maintain operational availability in the presence of machinery system faults. The background and motivation for these efforts are defined further in the subsequent chapter, followed by an overview of the research process and an overview of the key contributions.

## 1.1 Background Work and Motivation

Using stochastic reliability assessment methods previous studies [4–6] have quantified the shortcomings of ship machinery systems for successful operation in the unmanned and autonomous environment. The assessments provide clear evidence that traditional manned machinery systems are unable to reliably operate without human support over a long mission duration. In effort to close this knowledge gap Olson [7] used a stochastic Monte-Carlo simulation to evaluate varied machinery system architectures with modifications inspired by systems with ultra-high reliability in other domains. However the unique marine environment with high system complexity (size and interconnectivity) and long operational periods (weeks to months) did not allow modifications to system architectures to meet the demands of the marine operating environment. Additionally, Olson [7] studied long-duration mission performance in the face of machinery system failures. Olson [7] postulated a mission profile and conducted Monte-Carlo simulations to determine the probability that the ship could accomplish one or all of its assigned missions. A primary limitation of this work was the binary nature of the failures. A component did not consider the actual and typical degradation in performance but was classified as either 'healthy' or 'failed'. This rigid classification did not allow for the potential of active fault mitigation in a partially failed or failed system. These limitations require the need to better understand the degradation profile of common faults and failures within machinery plants and potential control mitigation strategies for machinery operation in the presence of common faults.

Given the inability to remove failures in design for this environment, successful unmanned operations will hinge on the ability to detect system faults, degradation in plant performance and predict the future operational availability of the machinery plant. Provided with accurate

knowledge of the current and future state of machinery plant health, mitigation techniques can be employed to avoid catastrophic plant failures caused by a degradation in component and system health. This is a different approach to that of the aviation or space domains where ultra-high reliability equipment or multiple redundant systems are utilized to eliminate fault impacts on performance altogether. The approach being proposed in this research is to allow individual component faults to occur and to manage the consequences of their occurrence either through redundant systems or through mission limitations.

To understand the current condition monitoring or health monitoring efforts by the United States Navy, a primary entity heavily pursuing autonomous and unmanned vessels, a review of their ICAS system was conducted. The ICAS system is the primary condition monitoring system utilized by the United States Navy [8]. The purpose of ICAS is to provide information about the current health of system components in effort to shift from preventative maintenance conducted based on a calendar schedule to condition based maintenance conducted on an as needed based on the current health of the given system or component. The program is successful in avoiding common critical failures through the usage of rule based restrictions and warnings [9, 10]. However, given the complexity and diversity of all systems onboard these vessels the ICAS system does not provide the ability to predict future failures and does cannot sufficiently support an autonomous system.

Non-intrusive load monitoring (NILM) provides a potential path to implement the necessary prognostic capabilities needed for the autonomous and unmanned environment. NILM utilizes a single non-intrusive current and voltage sensor placed on a single transmission line feeding a distribution panel, which supports many varying loads. This data can be disaggregated and analyzed in time to provide notification of potential system faults or abnormalities [11]. In recent years there has been several successful applications of NILM to the marine domain. Examples include, detection of mechanical coupling failure [11], ventilation system faults [12], and grey water system faults [13]. Additionally, real world deployment has been shown successful on a United States Coast Guard Cutter [14]. While these examples provide a clear proof of concept for NILM, all required an extensive amount of research for every individual application and shows limited promise for repeatability across similar systems. Given the complexity and diversity of surface vessel systems using NILM across all machinery systems becomes infeasible.

Applications of prognostics in other domains have recently leveraged AI, enabling a more flexible framework across various components and systems [15]. On hardware systems, prognostics has been primarily limited to the component level applications. Component level applications include transformer fault detection [16] and machine bearing RUL predictions [17]. At the system level, simple hardware systems explore the use of AI for optimal op-

erational state prediction as a first step towards understanding system level interactions through the use of data driven methods. An example is the use of a wind turbine hardware testbed to predict optimal operating state [18] using a Convolutional Neural Network (CNN) driven approach. Leveraging data from software models of hardware systems, further advancements in prediction algorithms have been made when compared to applications on physical hardware systems. An example of a software system model is NASA's gas turbine model [19], which generates run to failure (RTF) data for a range of common failure modes. This example model has become widely utilized as input data for testing data driven fault diagnostics and failure prediction algorithms [20, 21]. These applications of prognostics for both real world systems and model systems are contingent on rich datasets, and for real world systems pose a constant bottleneck [22].

In effort to reduce the amount of required real world data needed, a digital model can be tied to a physical system to create a digital twin (DT). The "digital twin" is popular in current academic research and provides some potential to expand the time horizon of current prognostic methods and account for the complexity of the interdependent marine systems. The digital twin provides a model replicating a physical system, which can be leveraged for usages including prediction of the response to a system given an unexpected event prior to the occurrence of the event. Using physics based models, digital twins have been constructed and updated by optimal decision trees to track structural damage for a 12ft unmanned aerial vehicle [23]. Additional examples of digital twin technology within the marine domain include condition monitoring for failure avoidance [24–26]. Furthermore, a recent literature review found applications of digital twin across several domains which show [27] initial implementation for maintenance optimization. Model integration and a formal maintenance framework based on model outputs, however, form two key barriers of digital twin for maintenance optimization [28]. As shown in recent research, a "digital twin" approach requires extensive knowledge of all system parameters, system operating profiles and an extensive model to be constructed. Given these requirements the "digital twin" is restricted by the time and design intensive efforts required to serve as an enabler of unmanned and autonomous and machinery system operation in the marine environment.

In this work the limitations of software based data or data from a single hardware system is resolved by the use of data from a laboratory scale ship machinery plant. The laboratory scale ship machinery plant emulates dynamics and cross couplings between systems within the plant that is seen on current ocean going ship machinery plants with additional functionality to inject and operate the plant to failure through virtual linkages. These virtual linkages enable fault and failure injection and system coupling that are not physically provided, allowing the repetitive injection of faults and failures without damaging physical hardware.

## 1.2 Research Overview

Data driven applications, such as AI, for prognostic and diagnostic tasks use large input datasets to train, validate and test potential models. To provide the necessary dataset a notional laboratory-scale ship machinery plant or MLSMP is proposed, designed, and constructed. The MLSMP provides hardware and software based system to system connections to enable the injection of common faults and failures with increasing severity in time until the plant fails. Failures are defined as a point where the MLSMP is unable to provide the necessary functionality for a desired operation (mission and propulsion load). The software based linkages enable the injection of faults until failure, without physical damage to components, providing an environment to record repetitive run to failure profiles. The MLSMP provides a second key capability to explore potential fault mitigation techniques in the laboratory environment. Three exemplary simulations are provided to showcase this capability. A simple diagnostic and prognostic task was completed for a singular subsystem within the cooling system to confirm initial feasibility prior to plant level applications. To explore the application of AI for detection of common faults and prediction of future plant operational availability for the MLSMP a large dataset with common run to failure profiles was required. A software model of the MLSMP was constructed and integrated with a model of clogging from literature. The model simulated a distribution of clogs and leaks for the cooling and fuel systems, providing control points to repeat the distributed run to failure profiles in hardware. A dataset of 100 run to failure (RTF) profiles, for the MLSMP was obtained by simulating the software control points on the hardware machinery plant through a real time automated control code. Each run to failure profile consists of up to 10 sequence-points, where each sequence point contains three unique sets of data at three set loading points for the propulsion and mission systems. The constructed dataset was used as input data to explore potential AI models and select a long short-term memory (LSTM) Recurrent Neural Network (RNN) driven model for the detection of individual system faults and the prediction of when an individual system would no longer provide the necessary functionality to support the necessary operational mission demands on the respective system. The applications of diagnostics and prognostics are used to form a multi-model diagnostic and prognostic prediction algorithm for the MLSMP. The formed plant level algorithm is tested and evaluated through the 100 RTF profiles to showcase the algorithms successes and prediction accuracy with respect to input parameter selection.

## 1.3 Research Contribution

In this PhD research, a novel laboratory scale ship machinery plant is designed, constructed and leveraged for acquisition of a run to failure dataset and as a simulation space to explore the potential of unconventional real time control methods for fault mitigation and avoidance. The run to failure dataset contains 100 failure profiles with common faults and failures injected into the laboratory systems, indicative of common faults and failures seen in real world applications. An LSTM driven multi-model diagnostic and prognostic framework is formed and tested using the collected laboratory scale run to failure dataset. The primary contributions of this research can be summarized as follows:

1. A laboratory scale ship machinery plant (MLSMP) was designed, constructed and validated with the necessary physical and virtual system interconnections to accurately represent plant dynamics and common faults of machinery plants found on vessels in the real world. The lab based plant, contains unique virtual linkages, in addition to physical system to system linkages, to enable to injection of common faults and failures within the machinery plant. The injected of faults and failures into the physical hardware plant provided the novel ability to increase the severity of the desired faults until plant failure occurs, without causing physical damage to the components or systems within the laboratory enabling the ability to collect repetitive run to failure datasets. The MLSMP provides a second capability to explore alternative fault mitigation techniques through real time system control. Hardware simulations of the MLSMP provide insight into the potential to improve operational resilience in an unmanned ship machinery environment environment through unconventional control mitigation techniques.

2. A run to failure (RTF) dataset was modeled in software and simulated in hardware through an automated process to build an archive of 100 RTF profiles to serve as input data for the exploration of data-driven diagnostic and prognostic algorithms and their ability to detect common faults and to predict when the vessel machinery plant will be unable to support a given operational profile. The RTF model incorporated common faults and failures for the cooling and fuel systems, clogs and leaks, and leveraged an existing model of real world clogs from literature to build a software model which simulated the buildup of particles on filters in time for the cooling system and fuel high and low pressure systems.

3. Unconventional control mitigation techniques are explored through a group of plant level hardware simulations using the MLSMP. This process illustrates the potential of real time control to improve operational resilience in a fault prone environment.

4. A multi-model LSTM driven framework is developed and evaluated for the ability to perform prognostic and diagnostic tasks to determine the current state of health for the MLSMP and predict future plant operational availability over a deployment period, until failure. The novel multi-model LSTM driven framework, evaluated using failure data from the MLSMP, provides a step forward in improving operational resilience for unmanned and autonomous vessels in a laboratory environment.

# CHAPTER 2

# Novel Multiphysics Laboratory Ship Machinery Plant

## 2.1 Introduction

A novel multi-physics physical hardware system has been built to obtain failure data for machinery systems to address the existing knowledge gap that currently prevents successful operation of marine machinery systems in absence of human intervention. The laboratory systems are consistent with standard commercial architectures and incorporate systems with high criticality and risk associated with failures. The fluid systems are linked with the electrical system providing real-world interactions between multi-physics systems, similar to what is found aboard modern ships. The fuel system is linked using software to the electrical generation system to provide real time dynamic response of the generation system based on the rail pressure of the fuel system. In a similar manner, the cooling system receives a software link to emulate the losses for all systems within the machinery plant. Both Fuel and cooling systems are physically linked to the electrical system through as their supply pumps draw power from the electrical system. These links provide multiple back-and-forth interactions between the various systems similar to what would occur in an actual shipboard environment. This selection provides a hardware system capable of emulating real world ship operation and trigger common failures over time, to record system data, which will serve as necessary inputs into machine learning models and the larger prognostics framework. The following sections of this chapter detail the constructed physical systems within the laboratory followed by a final section showcasing the laboratory system capabilities through exemplary hardware simulations. A high level overview of the eight sections within this chapter is provided in the following paragraph.

The first section, Section 2.2, of this chapter discusses the electrical power distribution system within the laboratory. The section details the main input connection to utility power and the distribution panels within the laboratory that are representative of ship

switchboards and a singular commercial panel for energy distribution to power our emulated diesel generators and energy storage system which are discussed in the second section of this chapter, Section 2.3. The following two sections, Section 2.4 and Section 2.5 define the cooling and fuel systems within the laboratory machinery plant, which are necessary support systems for the energy generation systems and large machinery plant loads. The large machinery plant loads consist of a two propulsion systems discussed in Section 2.6 and two mission systems discussed in Section 2.7. The machinery plant is controlled through an embedded control system that has the ability to both control the plant in real time and acquire data, this system is discussed in Section 2.8. The final section, Section 2.10, of this chapter showcases the capabilities of the laboratory scale ship machinery plant through two exemplary simulations. The final multi-physics hardware system defined throughout this chapter is referred to as the University of Michigan laboratory-scale ship machinery plant or (MLSMP).

## 2.2 Electric Power Distribution

The laboratory electrical system architecture is consistent with architectures found on most fully electric commercial ships and is shown in Figure 2.1.

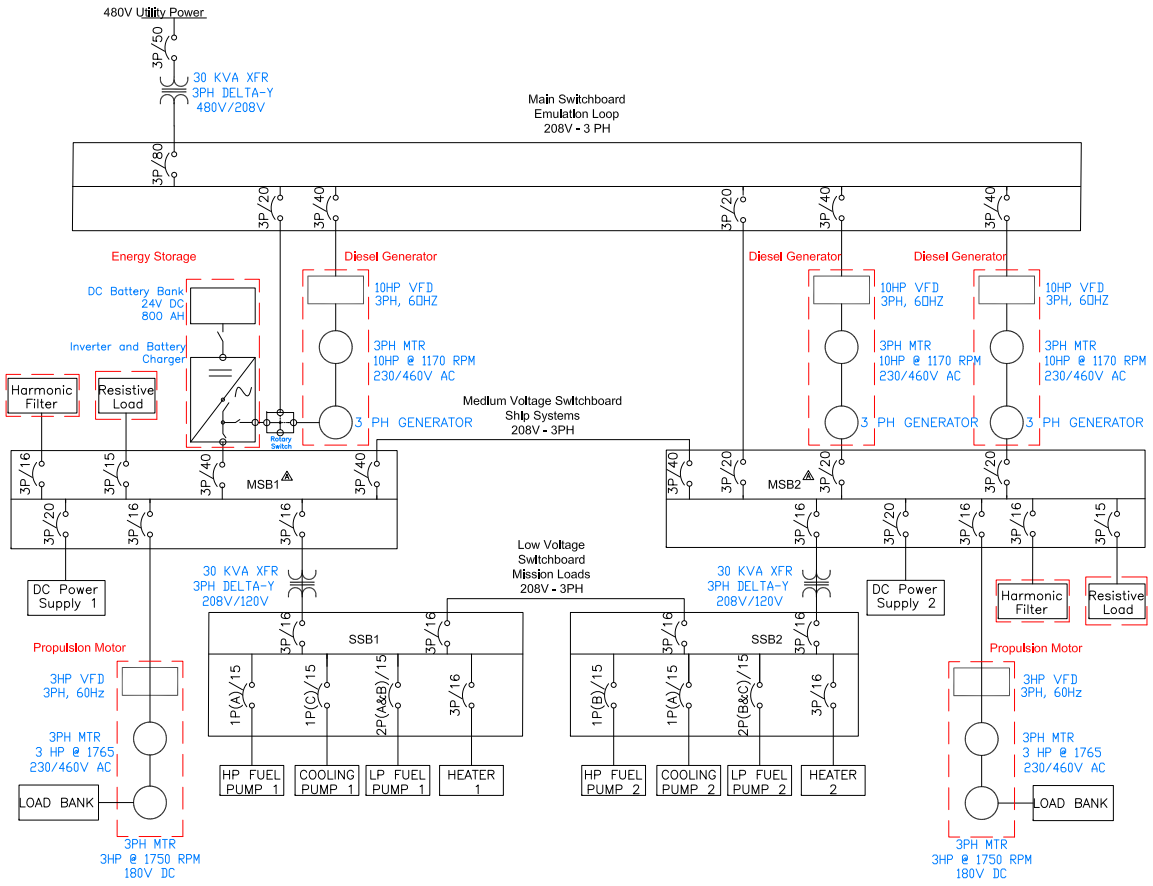


Figure 2.1: Electrical One Line Diagram

As shown above in Figure 2.1, the electrical grid within the laboratory consists of 5 main distribution panels: a commercial panel, main switchboard 1 and 2 (MSB1 and MSB2), and secondary switchboard 1 and 2 (SSB1 and SSB2). The commercial panel is powered through a single, three phase 480 Vac 50A utility connection. The utility connection is first isolated using a delta-wye isolation transformer prior to connection to the commercial panel. The commercial panel which is not part of the emulated shipboard system, is used to provide power to drive the three emulated generator sets (defined in Subsection 2.3.2), shore connections to MSB2 and to the inverters allow operation without the generator sets online and enable charging of the energy storage system. MSB1 and MSB2 serve as the main ship switchboards providing power to three phase loads and power through delta-wye transformers to the secondary switchboards. The secondary switchboards (SSB1 and SSB2) provide service to single phase loads that consist primarily of the fuel and cooling pumps. MSB1 is connected to the energy storage system and emulated generator set 1. MSB2 is connected to emulated generator set 2 and 3. A visual overview of as built MSB1 and MSB2 is shown below in Figure 2.2.

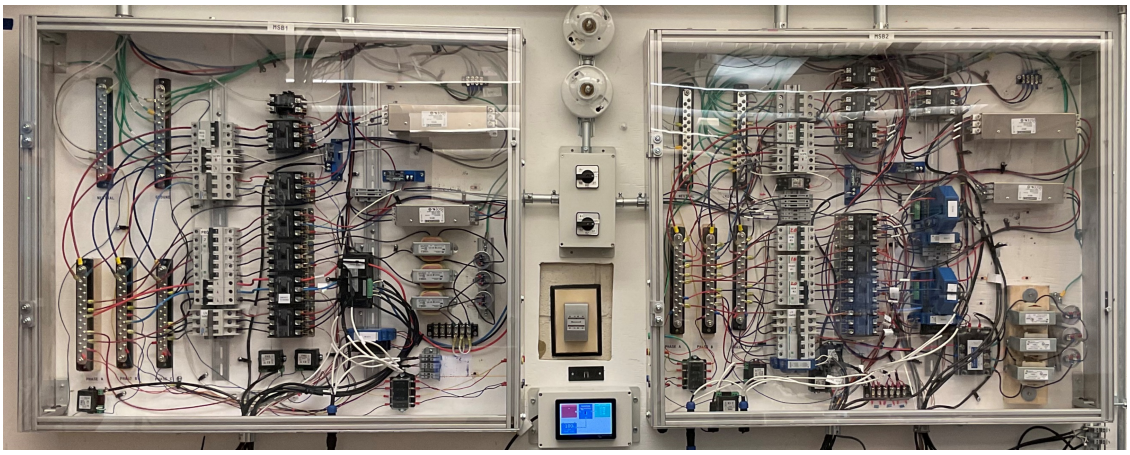

Figure 2.2: Main Switchboard 1 and 2

As shown above in Figure 2.2 the main switchboards contain a three phase distribution system with breakers and controllable relays. The switchboards also contain current and voltage sensors along with harmonic filters and EMI filters. A similar construction is used for the secondary switchboards and is shown below in Figure 2.3.

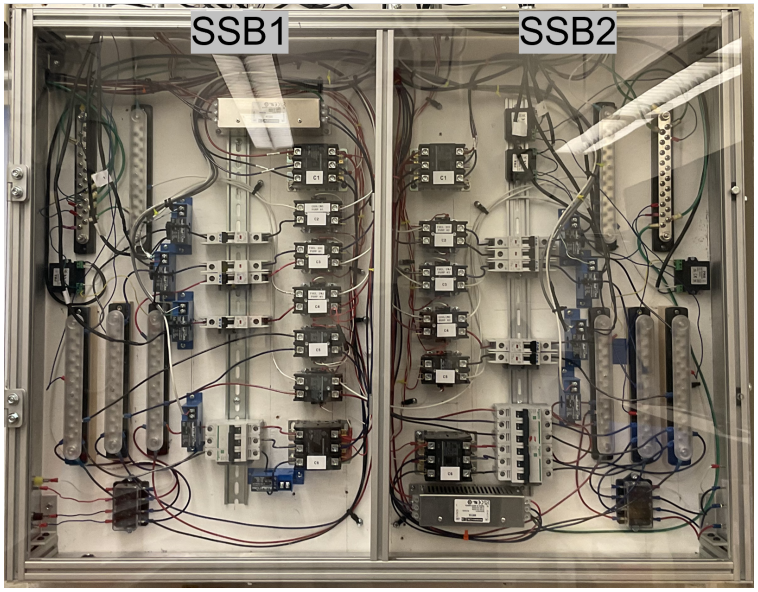


Figure 2.3: Secondary Switchboards 1 and 2

The sensor signals from all four switchboards and the relay control outputs are integrated through the embedded control system discussed in Section 2.8. The electrical system signals are summarized below in Table 2.1.

Table 2.1: Electrical System Signal List

| Component | Signal | Units |
|---|---|---|
| Utility Input | 3 Phase (A,B,C) - Voltage | Vac RMS |
| Utility Input | 3 Phase (A,B,C) - Amps | A RMS |
| Utility Input | Neutral | A RMS |
| Utility Input | Ground | A RMS |
| MSB1 | 3 Phase (A,B,C) - Voltage | Vac RMS |
| MSB1 | 3 Phase (A,B,C) - Voltage | Vac waveform |
| MSB2 | 3 Phase (A,B,C) - Voltage | Vac RMS |
| MSB2 | 3 Phase (A,B,C) - Voltage | Vac waveform |
| SSB1 | 3 Phase (A,B,C) - Voltage | Vac RMS |
| SSB1 | 3 Phase (A,B,C) - Voltage | Vac waveform |
| SSB2 | 3 Phase (A,B,C) - Voltage | Vac RMS |
| SSB2 | 3 Phase (A,B,C) - Voltage | Vac waveform |
| Electrical Relay | SSB1 to SSB2 | I/O |
| Electrical Relay | Shore Tie | I/O |
| Electrical Relay | Main Input | I/O |
| Electrical Relay | Resistive Load 1 | I/O |
| Electrical Relay | Resistive Load 2 | I/O |
| Electrical Relay | MSB1 to SSB1 | I/O |
| Electrical Relay | MSB2 to SSB2 | I/O |
| Electrical Relay | MSB1 to MSB2 | I/O |

## 2.3 Emulated Generator Sets and Energy Storage

### 2.3.1 Overview

Four energy sources have been constructed within the laboratory to provide connections to MSB1 and MSB2 representative of power profiles onboard real world all electric AC ships. The systems consist of three emulated generator sets and a battery-based energy storage system. Two emulated generator sets are connected to MSB2 and provide the ability to operate in parallel or as a sole power source. The energy storage system and emulated generator set 1 are connected to MSB1 and provide the ability to power the switchboard in multiple configurations. The configuration details of the emulated diesel generator sets and energy storage systems are provide below in the following two subsections.

### 2.3.2 Emulated Generator Sets

The laboratory contains three emulated generator sets, which can simulate the dynamics of any diesel engine or gas turbine engine onboard real world vessels. To emulate the desired combustion engine or gas turbine, the physical hardware system is coupled with a real time controller to produce the desired system dynamics. The physical system uses a variable frequency drive (VFD) to drive an induction machine, which is coupled to a three phase synchronous alternator providing power to the main switchboards. The VFD receives an input from a SISO (single input single output) open loop controller running in real time, which models the desired dynamics (gas turbine or diesel engine). The control loop uses the applied load torque provided from the VFD as the control input to update the generator frequency command in real time with respect to changes in system load. This approach followed past modeling approaches found in [29–34]. The open loop controller is shown visually in Figure 2.4 with parameters defined below in Table 2.2.

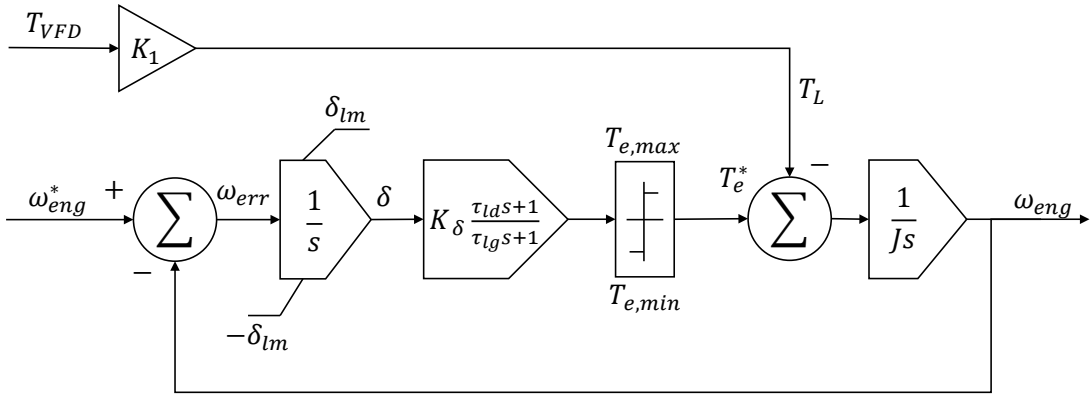


Figure 2.4: Diesel Generator Emulation Control

Table 2.2: Diesel Generator Emulation Control

| Parameter | Definition |
|---|---|
| $I_{gen}$ | Generator Current Demand (A) |
| **J** | Engine Inertia (kg-m2) |
| $K_1$ | Generator Current Load to Engine Torque Conversion Factor (Nm/A) |
| $K_\sigma$ | Controller Proportional Gain for Diesel Response Dynamics (Nm) |
| $\tau_L$ | Torque Load from Generator (Nm) |
| $T_{(e,min)}$ | Engine Torque Lower Bound (Nm) |
| $T_{(e,max)}$ | Engine Torque Limit (Nm) |
| $\delta_{lm}$ | Limit for Integrated Error (-) |
| $\tau_{ld}$ | Time Constant for Engine Response Dynamics (s) |
| $\tau_{lg}$ | Time Constant for Engine Response Dynamics (s) |
| $\omega_{eng}$ | Engine Speed (Rad/sec) |
| $\omega_{eng}$ | Engine Set Speed (Rad/sec) |
| $\omega_{err}$ | Difference Between Engine Set Speed and Current Speed (Rad/sec) |

The open loop controller shown in Figure 2.4 accounts for the transient response of real world gas turbines or diesel generators that arise as a results of generator inertia, fuel system dynamics and generator control systems. A visual of the system response to a step in load for both the constructed MATLAB Simulink model and the actual hardware system is shown below in Figure 2.5.

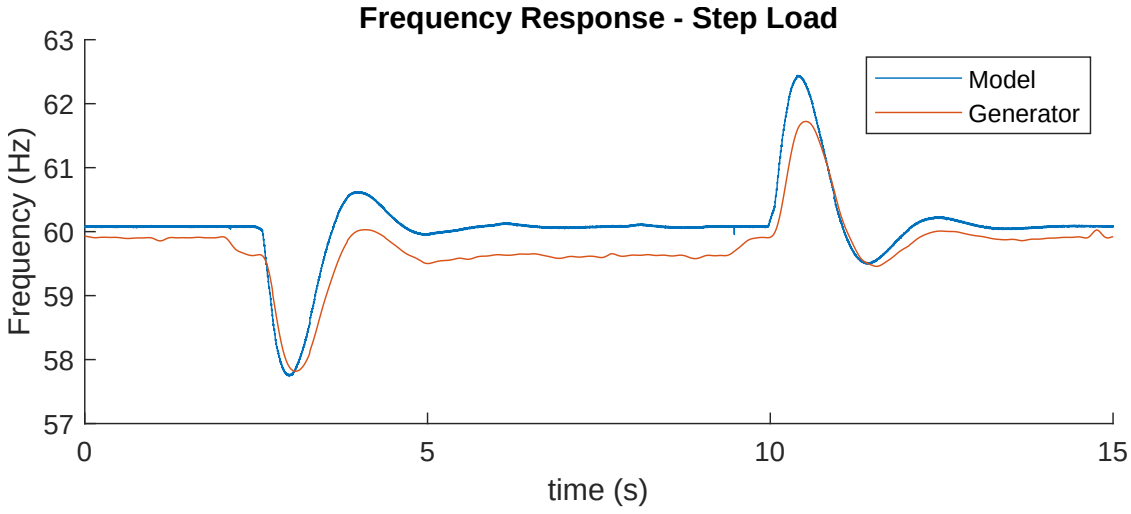


Figure 2.5: Diesel Generator Model and Hardware Example Response

As shown above in 2.5 the hardware system is able to closely match the dynamic profile

in the event of a step on and off in system loading of 40 % of generator nameplate capacity.

The ability to emulate a real world diesel or gas turbine generator set through the use of an embedded control system, VFD, induction machine and synchronous three phase alternator provides the capability to model in hardware any physical generator system. This configuration also provides ability to model in hardware common faults and failures for energy generation systems and the subsequent plant level response without a damaging the physical hardware system. The losses of a diesel generator set are also emulated in the machinery plant by placing the corresponding waste heat losses into the cooling system through a virtual linkage discussed in Section 2.4. A summary of the signals hardware I/O signals for emulated diesel generator set 1 is shown below in Table 2.3. The signals shown for generator set 1 are identical for generator set 2 and generator set 3.

Table 2.3: Emulated Generator Set 1 Signal Summary

| **Component** | **Signal** | **Units** |
|---|---|---|
| 3 Phase Alternator | 3 Phase (A,B,C) - Voltage | Vac RMS |
| 3 Phase Alternator | 3 Phase (A,B,C) - Amps | A RMS |
| 3 Phase Alternator | 3 Phase (A,B,C) - Voltage | Vac waveform |
| 3 Phase Alternator | 3 Phase (A,B,C) - Amps | A waveform |
| VFD | Load Torque Applied | % of Max Torque |
| VFD | Start / Stop | I/O |
| Relay | Gen1 to Bus | I/O |
| AVR | Voltage Setpoint | Vac RMS |

### 2.3.3 Energy Storage and Inverter System

The energy storage system shown visually in Figure 2.6 consists of three commercial inverter and charger units connected to MSB1 in a wye convention and programmed to operate as a three phase system. The three units have a common DC link to a 24V, 400 AH battery bank. The battery bank is capable of providing 9.6 kWh of power and an instantaneous output of 9 kVA. The energy storage system is programmed with four main operation modes defined below.

- Mode 1 (UPS): The energy storage system is on standby and instantaneously (within 20ms) takes over supply of the connected loads in the event generator 1 is disconnected or power quality is out of tolerance.

- Mode 2 (UPS and Assist): In addition to the functionality of Mode 1, Mode 2 provides power assist to the connected loads in parallel to generator 1 for load cases greater than 90 % of generator capacity and for sharp changes in load.
- Mode 3 (charge only): Allows the energy storage system to recharge through connection to the utility panel, without output to MSB1 or connection to generator 1.
- Mode 4 (charge % support): This mode provides the functionality of Mode 2 with an additional ability for the energy storage system to charge from the connected generator as needed to maintain the battery bank state of charge.

The four configuration modes for the energy storage system provide flexible functionality for a large variety of machinery plant simulations and are referred to in subsequent sections and chapters of this thesis.

A summary of the signals hardware I/O signals for the energy storage system is provided in Table 2.4.

Table 2.4: Energy Storage Signal Summary

| **Component** | **Signal** | **Units** |
|---|---|---|
| Battery Bank | DC Current | A DC |
| Battery Bank | Temperature | Deg C |
| Battery Bank | Voltage | Vdc |
| Inverter | 3 Phase (A,B,C) - Voltage | Vac RMS |
| Inverter | 3 Phase (A,B,C) - Amps | A RMS |
| Inverter | 3 Phase (A,B,C) - Voltage | Vac waveform |
| Inverter | 3 Phase (A,B,C) - Amps | A waveform |
| Inverter | Relay Inverter to Bus | I/O |

### 2.3.4 Visual Summary

A visual of the emulated generator sets and energy storage system within the laboratory is shown below in Figure 2.6.

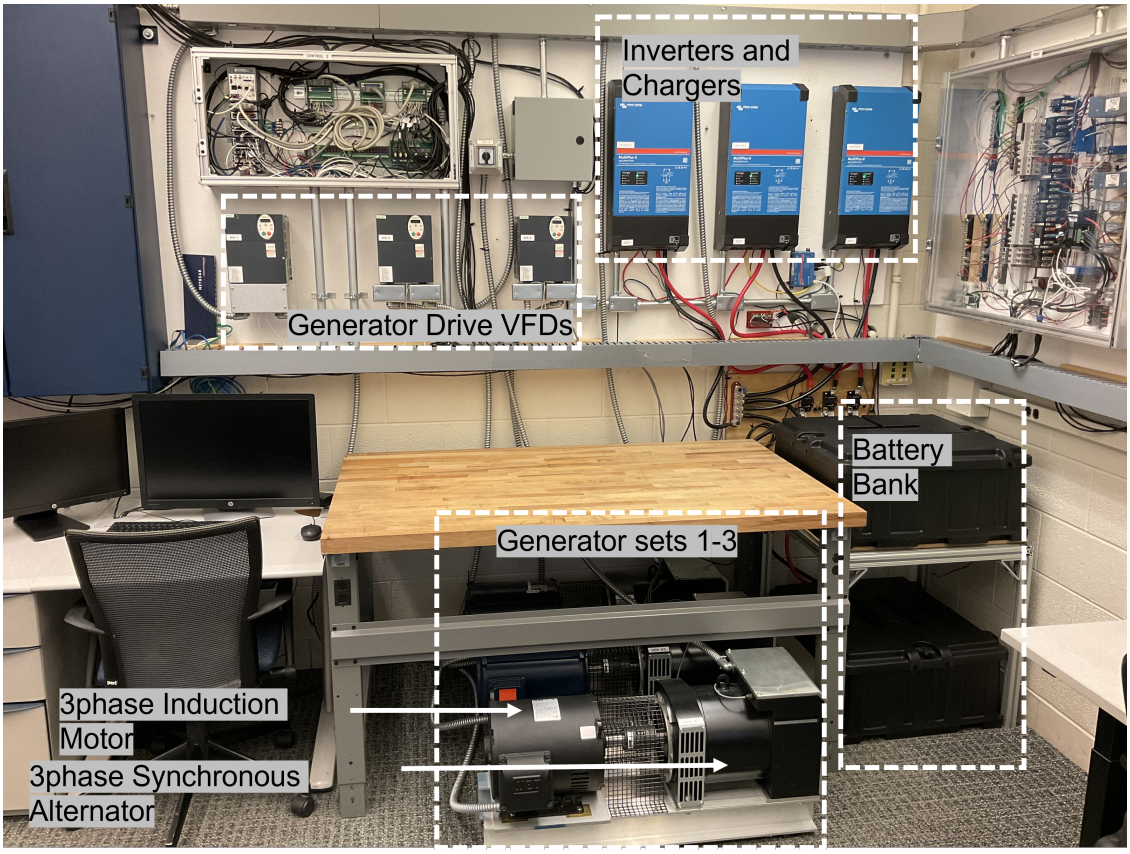


Figure 2.6: Emulated Diesel Generator Sets and Energy Storage

As shown above in Figure 2.6, the three emulated diesel generator sets are located below the table and are powered by VFDs mounted to the wall in the upper left hand side of the image. The energy storage chargers and inverters are wall mounted in the upper right hand side of the image, with connection to the battery bank located in the black boxes on the right hand side of the image.

The energy storage and emulated generators are connected through virtual links in real time to support cooling and fuel systems. This coupling provides the ability to inject common fuel and cooling system faults and observe the subsequent electric plant response. The cooling and fuel support systems are defined in the next two sections of this chapter.

## 2.4 Cooling System

### 2.4.1 Overview

The cooling system represents the necessary support system that would exist in an all electric ship machinery plant to provide waste heat dissipation for water cooled systems and their

losses. A few examples of water cooled equipment onboard a real would ship machinery plant include: propulsion system drives, diesel generator sets, air compressors, air conditioning plants, and gas turbines. The cooling system in the laboratory setting, consists of two parallel flow paths which can be configured as a dual-redundant system. The cooling system diagram is shown below in Figure 2.7.

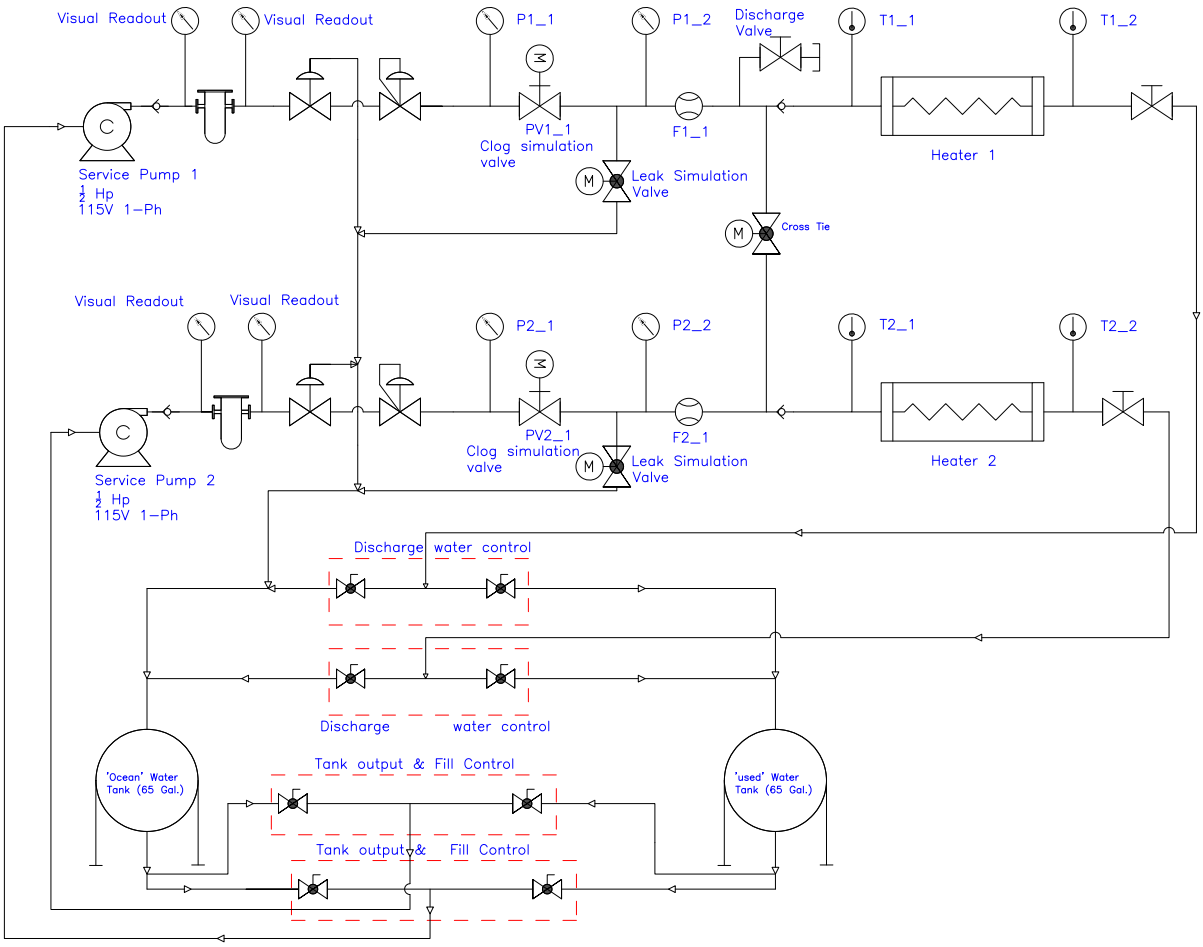


Figure 2.7: Cooling System - Diagram

The two parallel flow paths are serviced by two centrifugal pumps, where service pump 1 is connected to SSB1 for power providing flow to flow path 1 and service pump 2 is connected to SSB2 for power providing flow to flow path 2. Each flow path draws from a "ocean" water tank and discharges the waste water into a "used" water tank. Both flow paths have a proportional valve which provides the ability to place variable restrictions to flow in real time, representative of real world cooling system clogs. Each flow path also contains a controllable valve to inject a binary leak into the system.

The cooling system dissipates waste heat generated by two three phase restive heaters

that are each individually controlled with a variable frequency drive. The real time input of waste heat into the cooling system is emulated through a virtual control system linkage defined in Subsection 2.4.3. The embedded control system takes into account loading on the generator, propulsion systems, and mission systems. The respective waste heat loss, given real time plant loading is injected into the cooling system using a three phase restive water heater and a variable frequency drive for control of the injected waste heat. A list of signals for the cooling system is provided below in Table 2.5.

Table 2.5: Cooling System Signals and Controls

| **Variable** | **Path** | **Parameter** |
|---|---|---|
| P1-1 | 1 | Pressure before clogs and leaks |
| P1-2 | 2 | Pressure before clogs and leaks |
| P2-1 | 2 | Pressure after clogs and leaks |
| P2-2 | 2 | Pressure after clogs and leaks |
| T1-1 | 1 | Inlet temperature to heater1 |
| T1-2 | 1 | Outlet temperature to heater1 |
| T2-1 | 2 | Inlet temperature to heater2 |
| T2-2 | 2 | Outlet temperature to heater2 |
| T-Ocean | - | Ocean tank temperature |
| T-Waste | - | Waste tank temperature |
| PV1-1 | 1 | Proportional valve for clog simulation |
| PV2-1 | 2 | Proportional valve for clog simulation |
| L1 | 1 | Controllable ball valve for Leak simulation |
| L2 | 2 | Controllable ball valve for Leak simulation |
| CT1 | 1 | Current transducer on pump 1 |
| CT2 | 2 | Current transducer for pump 2 |

As shown in Table 2.5 the cooling system and its' two parallel flow paths has rich group of input and output signals to enable virtual linkages between other plant systems and enable data acquisition for prognostic implementation. The injection of cooling system faults (leaks and clogs) and the emulated waste heat is further defined in the following two sections followed by a summary of the cooling system capabilities.

### 2.4.2 Fault Injection

To inject common faults and failure onboard real world vessels a proportional valve and controllable ball valve were added to both flow paths within the cooling system. The ball valve provides the ability inject binary leaks (leak or no leak). The leak size is set by a manual ball valve prior to the controllable valve. This set point is constant throughout all work in this thesis. The injection of leaks can be triggered through two main modes: Manually through the user HMI or at a desired time during a simulation through a spreadsheet containing timed control system commands.

Two proportional valves are used to inject clogs into both flow paths. The proportional valves can be controlled as a linear function of cross sectional area from fully open to closed. The control to the valves can be sent in three modes: a manual mode set by the user through the HMI interface, a constant mode read from a loaded spreadsheet, or in a dynamic mode with parameters set in a loaded spreadsheet. The three modes enable the ability to run large simulation batches at a constant clog rate or a dynamically changing clog rate and also provides the ability for a user to simply set the clog through the user HMI.

### 2.4.3 Emulated Waste Heat

To provide a virtual linkage for waste heat based on plant load, the heater control command is provided as a percentage of maximum system losses. The waste heat for both systems is a function of the generator load (% load torque), energy storage output (kW), mission system power consumption (kW), and propulsion system power consumption (kW) in time. The respective component losses for each heater is shown below in Equation 2.1 and Equation 2.2 with variables defined in Table 2.6.

$$H1_{load(\%)} = f(G1_{Torque}, G2_{Torque}, E_{kW}, P1_{kW}, M1_{kW}) \tag{2.1}$$

$$H2_{load(\%)} = f(G3_{Torque}, P2_{kW}, M2_{kW}) \tag{2.2}$$

Table 2.6: Waste Heat Emulation

| Variable | Parameter | Unit |
|---|---|---|
| $G1_{Torque}$ | Generator 1 Drive Torque | % of max |
| $G2_{Torque}$ | Generator 2 Drive Torque | % of max |
| $G3_{Torque}$ | Generator 3 Drive Torque | % of max |
| $G1_{kW}$ | Generator 1 Output | kW |
| $G2_{kW}$ | Generator 2 Output | kW |
| $G3_{kW}$ | Generator 3 Output | kW |
| $E_{kW}$ | Energy Storage Input and Output | kW |
| $P1_{kW}$ | Propulsion System 1 - power consumption | kW |
| $P2_{kW}$ | Propulsion System 2 - power consumption | kW |
| $P1_{kW-max}$ | Propulsion System 1 - max power consumption | kW |
| $P2_{kW-max}$ | Propulsion System 2 -max power consumption | kW |
| $M1_{kW}$ | Mission System 1 - power consumption | kW |
| $M2_{kW}$ | Mission System 2 - power consumption | kW |

The waste heat losses for the propulsion and generator systems leverage lookup tables. The lookup tables take input of percentage load and provide the respective percentage of losses given plant loading. The lookup tables have been developed from real world propulsion and generator set load to loss curves. The waste heat losses for the mission system are assumed to be constant, with 80% of the total load rejected to heat (20 % efficient). The energy storage system losses are assumed to be a constant 10 % rejection to waste heat for any energy used to charge or discharge the system. These constant percentages could be changed, or a load vs. loss profile could be inserted in their place. The calculation for waste heat loss is further defined in the equations below where $L_{gen}$ defines the lookup table for generator losses and $L_{prop}$ defines the lookup table for propulsion system losses.

$$H1_{load(\%)} = \frac{1}{C1} * (L_{gen}(G1_{Torque}) * G1_{kW} + L_{gen}(G2_{Torque}) * G2_{kW} + E_{kW} * 0.10 + L_{prop}(\frac{P1_{kW}}{P1_{kW-max}}) * P1_{kW} + M1_{kW} * 0.80) \quad (2.3)$$

$$H2_{load(\%)} = \frac{1}{C2} * (L_{gen}(G3_{Torque}) * G3_{kW} + L_{prop}(\frac{P2_{kW}}{P2_{kW-max}}) * P2_{kW} + M2_{kW} * 0.80) \tag{2.4}$$

The two equations shown above leverage constant terms $C1$ and $C2$ to scale the calculated waste losses. The constant term $C1$ and $C2$ represent the respective maximum system losses to convert the waste heat into a value between 0 to 100 representing the percentage of waste heat losses. A summary of the I/O signals for the control of waste heat is provided for heater 1 below in Table 2.7 and is identical for heater 2.

Table 2.7: Waste Heat System 1 Signals

| **Component** | **Signal** | **Units** |
|---|---|---|
| Heater VFD | Input Current | Amps RMS |
| Heater VFD | Enable | I/O |
| Heater VFD | Waste Heat Command | (%) of max |
| Heater VFD | Relay to SSB1 | I/O |

### 2.4.4 Summary

The cooling system provides a virtual link between the dynamic plant load and required waste heat dissipation, has the ability to inject common real world faults (clogs and leaks) as well as the functionality to impose limitations on other systems within the laboratory given as a result of overheating. These capabilities provide the ability to accurately represent common faults and failures in time for a shipboard cooling system and the subsequent effect on plant level functionality. A visual of the as built cooling system configuration is shown below in Figure 2.8

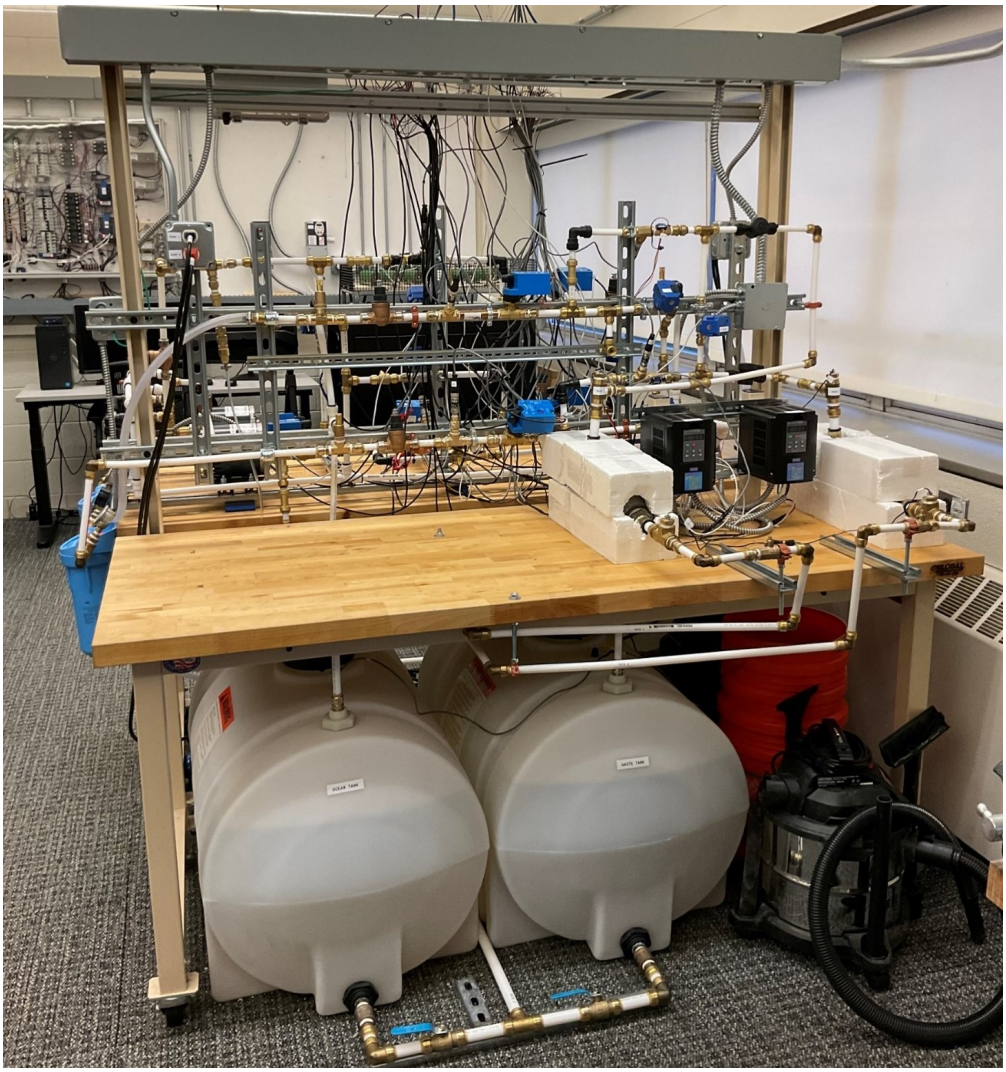

Figure 2.8: Cooling System - Visual

## 2.5 Fuel System

### 2.5.1 Introduction

The fuel system is interconnected through a virtual linkage to the available emulated diesel generator torque in real time, which provides the ability to limit available generator torque based on fuel system conditions. The fuel system consists of two parallel flow paths, each containing a low pressure supply system and a high pressure injection system. The fuel system simulates fuel flow using water as the fluid to represent fuel. The fuel system diagram is shown below in Figure 2.9.

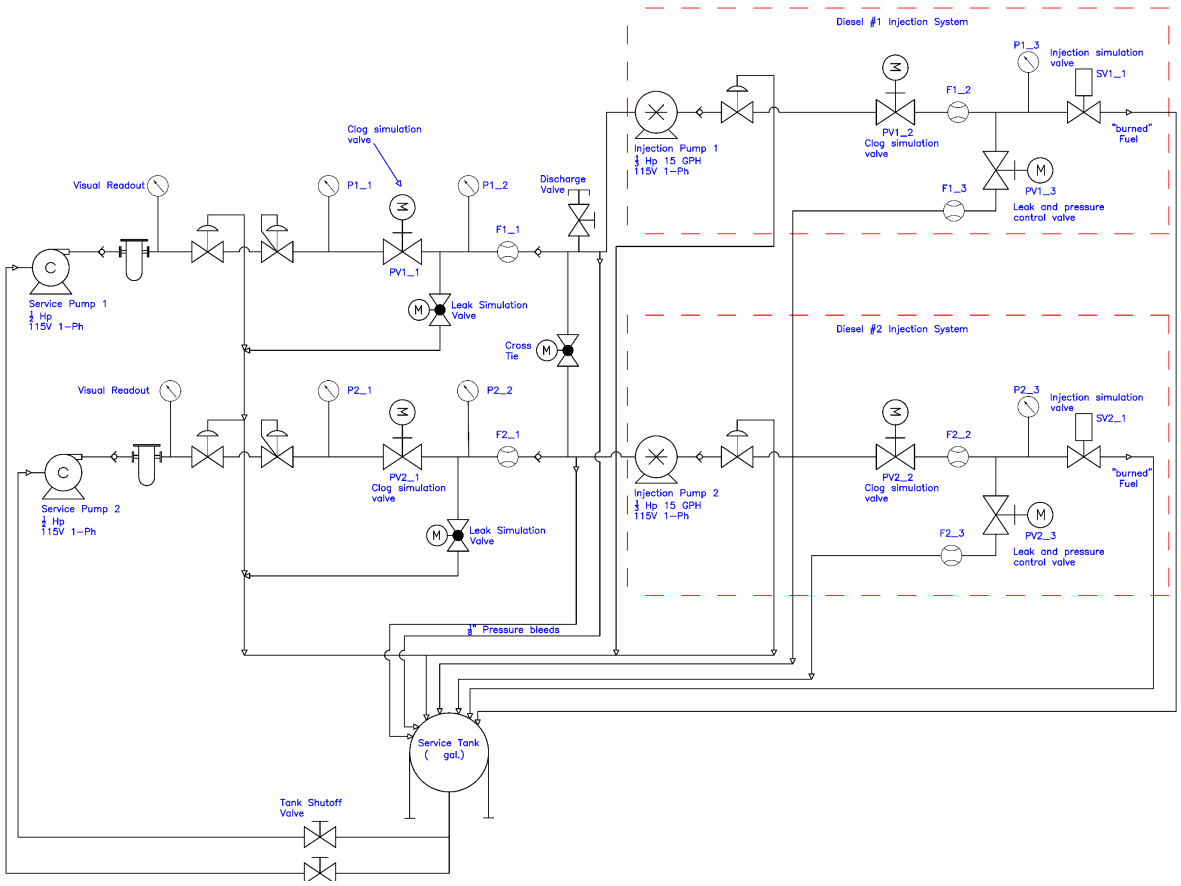


Figure 2.9: Fuel System - Diagram

The two flow paths are identical, each containing a low pressure system powered by a centrifugal pump that simulates the ship's fuel service system and a high pressure system driven by a positive displacement pump which simulates the on-engine portion of the fuel system. The fuel system circulates water through both parallel loops drawing and returning from a common 35 gallon tank. For work in this thesis the fuel system has been constructed and controlled to model diesel engine dynamics; however, the fuel system control can be modified to model various combustion engines or gas turbines. The signals for control and data acquisition on the two fuel systems are shown below in Table 2.8.

Table 2.8: Fuel System Signals and Controls

| Variable | Path | Parameter |
|---|---|---|
| P1-1 | LP1 | Pressure before clogs and leaks |
| P1-2 | LP2 | Pressure before clogs and leaks |
| P2-1 | LP2 | Pressure after clogs and leaks |
| P2-2 | LP2 | Pressure after clogs and leaks |
| P1-3 | HP1 | High pressure rail |
| P2-3 | HP2 | High pressure rail |
| PV1-1 | LP1 | Proportional valve for clog simulation |
| PV2-1 | LP2 | Proportional valve for clog simulation |
| PV1-2 | HP1 | Proportional valve for clog simulation |
| PV2-2 | HP2 | Proportional valve for clog simulation |
| PV1-3 | HP1 | Proportional valve for HP control and leak simulation |
| PV2-3 | HP2 | Proportional valve for HP control and leak simulation |
| L1 | 1 | Controllable ball valve for Leak simulation |
| L2 | 2 | Controllable ball valve for Leak simulation |
| SV1-1 | 1 | Fuel Injection solenoid valve |
| SV2-1 | 2 | Fuel Injection solenoid valve |
| CT1-1 | 1 | Current transducer on LP pump |
| CT2-1 | 2 | Current transducer on LP pump |
| CT1-2 | 1 | Current transducer on HP pump |
| CT2-2 | 2 | Current transducer on HP pump |

As shown above in Table 2.8, the fuel system and its' two parallel flow paths has rich group of input and output signals to enable virtual linkages between other plant systems and enable data acquisition for prognostic implementation. The injection of fuel system faults (leaks and clogs) and the fuel injection system is further defined in the following two sections followed by a summary of the fuel system capabilities.

### 2.5.2 Fault Injection

To inject common faults and failure onboard real world vessels a proportional valve and controllable ball valve were added to both low pressure flow paths within the fuel system. The ball valve provides the ability to inject binary leaks (leak or no leak). The leak size is set by a manual ball valve prior to the controllable valve. This set point is constant throughout all work in this thesis. The injection of leaks can be triggered through two main modes:

Manually through the user HMI or through a loaded spreadsheet at a given desired time during a simulation.

Four proportional valves are used to inject clogs into both low pressure flow paths and both high pressure rails. The proportional valves can be controlled as a linear function of cross sectional area from fully open to closed. The control to the valves can be sent in three modes: Manual mode set by the user through the HMI interface, a constant mode read from a pre-loaded spreadsheet, or in a dynamic mode with parameters set in a pre-loaded spreadsheet. The three modes enable the ability to run large simulation batches at a constant clog rate or a dynamically changing clog rate and also provides the ability for a user to simply set the clog through the user HMI.

The high pressure system leverage two additional proportional valves to provide a high pressure relief, allowing for control of rail pressure. The set point of these valves can be offset to inject a leak into the high pressure rail. Leaks into both high pressure rail systems can be injected in the three modes defined for the proportional clog valves.

### 2.5.3 Fuel Injection Control

The modeling and hardware integration for the fuel injection system was part of work funded in conjunction with this dissertation and is further described in [1]. This section provides a summary of the modeling and hardware integration for the fuel injection system leveraged throughout hardware simulation work as part of this PhD dissertation and is work lead by Almquist [1].

The circuit used to control the solenoid injection valve is provided an analog input from the embedded control system proportional to fuel injection percent as a function of wide open throttle (WOT). The circuit leveraged two semiconductors to create the pulse timing indicative of the notional diesel engine and buffer the necessary power to drive the solenoid at the computer amplitude in accordance to the real time power demand of the virtually linked diesel generator set. The control circuit schematic is shown in Figure 2.10

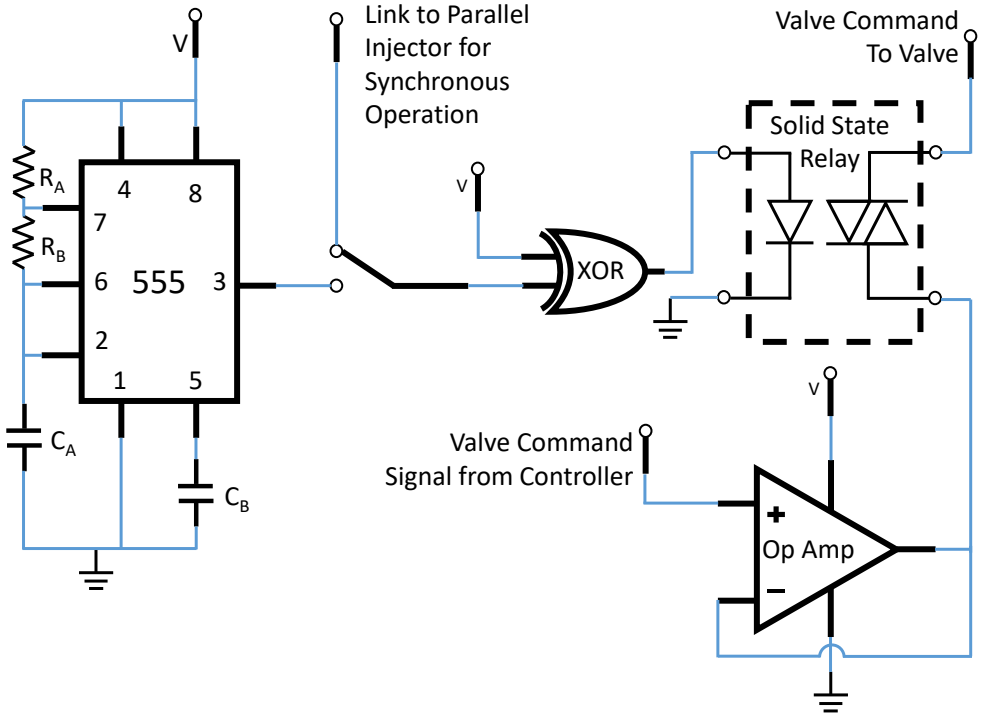


Figure 2.10: Fuel Injection Control Circuit [1]

The control system command from the main control system to the hardware circuit can be linked to any of the three emulated diesel generators within the laboratory. This linkage provides the throttle setting as a function of the real time load for the VFD driving the synchronous alternator. A summary of the injection control signals is provided below in Table 2.9.

Table 2.9: Injection Control Signals - LabVIEW to Embedded Hardware

| **Component** | **Signal** | **Units** |
|---|---|---|
| Injector 1 Control | Injection Command | V DC |
| Injector 1 | Injection Pulse | V DC |
| Injector 2 Control | Injection Command | V DC |
| Injector 2 Control | Injection Pulse | V DC |

In the event a fault is injected into the fuel system and rail pressure is degraded, the fuel system controller attempts to adjust the throttle setting to account for the resultant degradation in fuel injected. The adjustment of throttle position with respect to rail pressure and demanded fuel is shown below in Figure 2.11. This representation is provided for a rail

pressure of 145 PSI and below. The normal Operating rail pressure is set at 145 to 150 PSI.

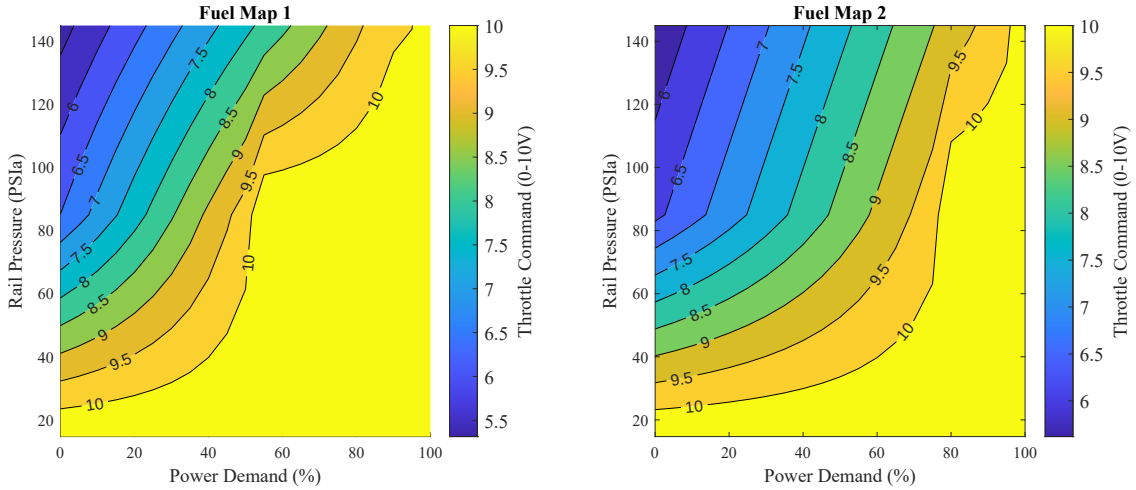


Figure 2.11: Fuel System - Injector Control Map Modified from [1]

The yellow section of Figure 2.11 represents saturation of the fuel injection command at (WOT) where demanded fuel is not achieved. The insufficient fuel flow through the emulated fuel injection system occurs where rail pressure is low due to a system fault (clog and leaks) and generator loading is high. To integrate response of a fuel system fault on the virtually linked generator, a torque limit is placed into the control loop for the emulated diesel generator set. The torque limit is set as a function of rail pressure to limit available toque to the synchronous alternator based on the fuel system dynamics. This virtual cross linkage provides the ability to inject real world faults and failures for the fuel system and model the subsequent generator set and plant level response.

### 2.5.4 Summary

The fuel system provides two virtual links between the emulated diesel generators to simulate the fuel flow and injection dynamics for a notional diesel engine and the subsequent generator response. The fuel fuel dynamics are controlled by the real time loading of the emulated generator based on the torque demanded by the linked synchronous alternator. The fuel system injection flow is observed as a function of rail pressure and through a second virtual linkage, a torque limit is placed on the generator when the error in fuel injection (error = actual - demanded flow) is negative. This virtual linkage provides the ability to inject real world faults and failures for the fuel system and model the subsequent plant level response. A visual of the as built fuel system configuration is shown below in Figure 2.12.

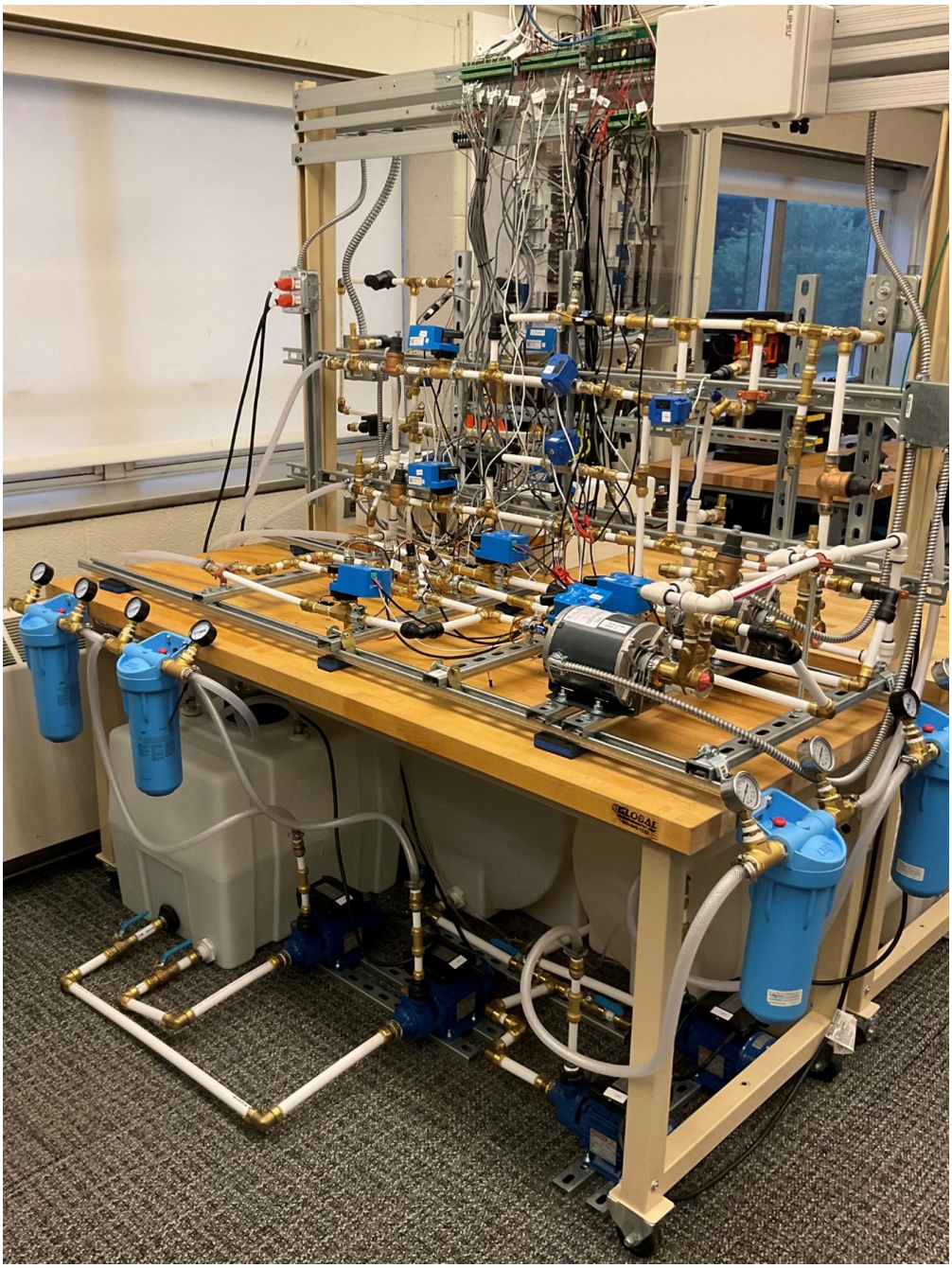

Figure 2.12: Fuel System - Visual

## 2.6 Propulsion

The machinery plant has two main propulsion systems, propulsion system 1 and 2, attached to MSB1 and MSB2 respectively. The the two propulsion systems consist of a variable frequency drive which powers a three phase induction motor that is used to drive a separately

excited wound field DC machine acting as a generator. The VFDs and induction machine are representative of a notional all electric ship propulsion system. The wound field DC machine is used to produce a load on the induction machine representative of a notional cubic speed to power load profile. To create the desired load profile, the DC machine armature is connected to a constant resistor load and the field is externally excited by a controllable DC power supply programmed as a function of speed. The electrical one line diagram for this configuration is shown below in Figure 2.13.

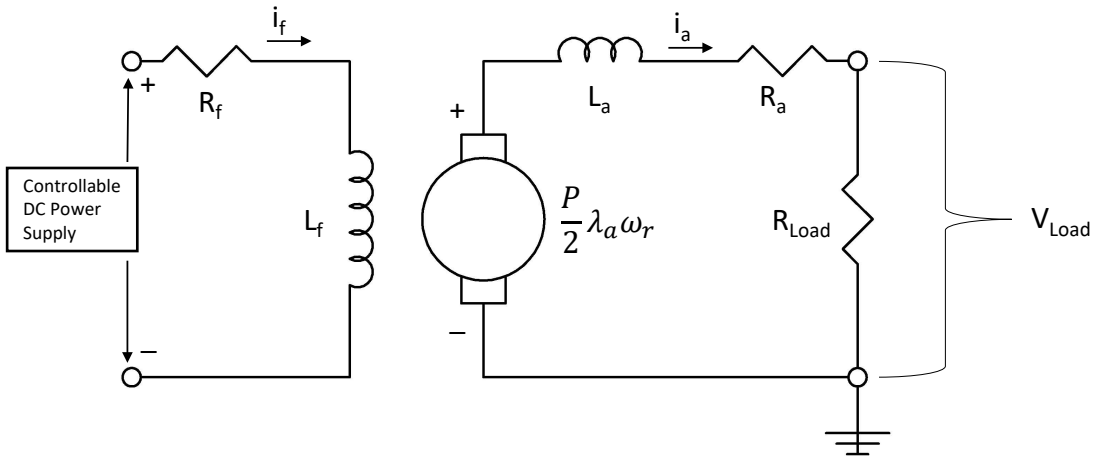


Figure 2.13: Propulsion DC Load Machine - Wiring Diagram

The field winding with resistance ($R_f$) and inductance ($I_f$) are externally excited by the controllable DC power supply. The DC power supply receives an analog input from the embedded control system, in real time as a function of commanded propulsion speed. The armature with internal resistance ($R_a$) and inductance ($L_a$) are connected to a resistive load bank ($R_{Load}$) that has a fixed resistance. Given the configuration hardware system and the desired cubic speed to power load profile a control equation was derived.

The control equation was derived assuming steady state conditions and linear DC machine losses without the presence of excitation field losses, given the external field power supply was powered by the building. Using these assumptions, the following equations were leveraged to produce a cubic power load profile across the resistance heater with respect to propulsion shaft rotational rate.

$$P_{load} = \frac{{V_a}^2}{R} \tag{2.5}$$

Given the desire for $P_{load}$ to increase as a cubic function of speed, the output voltage, $V_a$ must increase linearly with respect to shaft speed. The output voltage can be as shown in

Equation 2.6.

$$V_a = R_a I_a + \frac{N_p}{2} M_{af} I_f \omega_r \tag{2.6}$$

Where $V_a$ is a function of machine constants, (number of poles $N_p$ and field inductance $M_{af}$), and current through the excitation field $I_f$. The field current can be controlled through variation of the input field voltage as shown below.

$$I_f = \frac{V_f}{R_f} \tag{2.7}$$

Therefore the load power becomes:

$$P_{load} = \frac{(R_a I_a + \frac{N_p}{2} M_{af} \frac{V_f}{R_f} \omega_r)^2}{R_{Load}} \tag{2.8}$$

By dropping constant terms and considering the armature losses to be negligible as compared to the load, the power by the dc machine reduces to a function of field voltage, $V_f$, and shaft rotational frequency, $\omega_r$, as shown below.

$$P_{load} = C_1 V_f^2 \omega_r^2 \tag{2.9}$$

By exciting $V_f$ as function of the square root of $\omega_r$ a cubic speed to power curve is achieved. Using this relationship, the numerical constant corresponding with voltage can be determined using experimental testing and known parameters provided in Tables 2.10 below.

Table 2.10: DC Machine Specifications

| **Parameter** | **Value** | **Unit** |
|---|---|---|
| Poles | 2 | - |
| Field Voltage | 100 | VDC |
| Armature Voltage | 180 | VDC |
| Armature Current | 14.7 | ADC |
| Rotational Rate | 1750 | RPM |

Provided it is desired to produce the maximum load toque at the maximum rotational rate of 60Hz for the machine, the DC machine operates in an under load capacity at all loading points below maximum speed. Given the desired quadratic loading structure the field excitation limit was experimentally determined by operating the DC machine at 60Hz and increasing the field voltage until a capacity constraint was met, defined in Table 2.10.

The limitation for the DC machine was maximum current output, which was achieved at an excitation of 90 VDC. Given this limitation the finalized control equation was formed.

$$V_{Command} = 9 * \frac{\sqrt{\omega_r}}{\sqrt{\omega_{r-max}}} \tag{2.10}$$

The control command shown above in equation 2.10 is a function of commanded propulsion speed $\omega_r$, maximum speed $\omega_{r-max}$ and accounts for the necessary scaling for the analog control signal of 0-10 Vdc to DC power supply output of 0-100v DC.

Leveraging the electrical configuration shown in Figure 2.13 and control Equation 2.10 the systems produce the desired quadratic loading profile shown visually below in Figure 2.14.

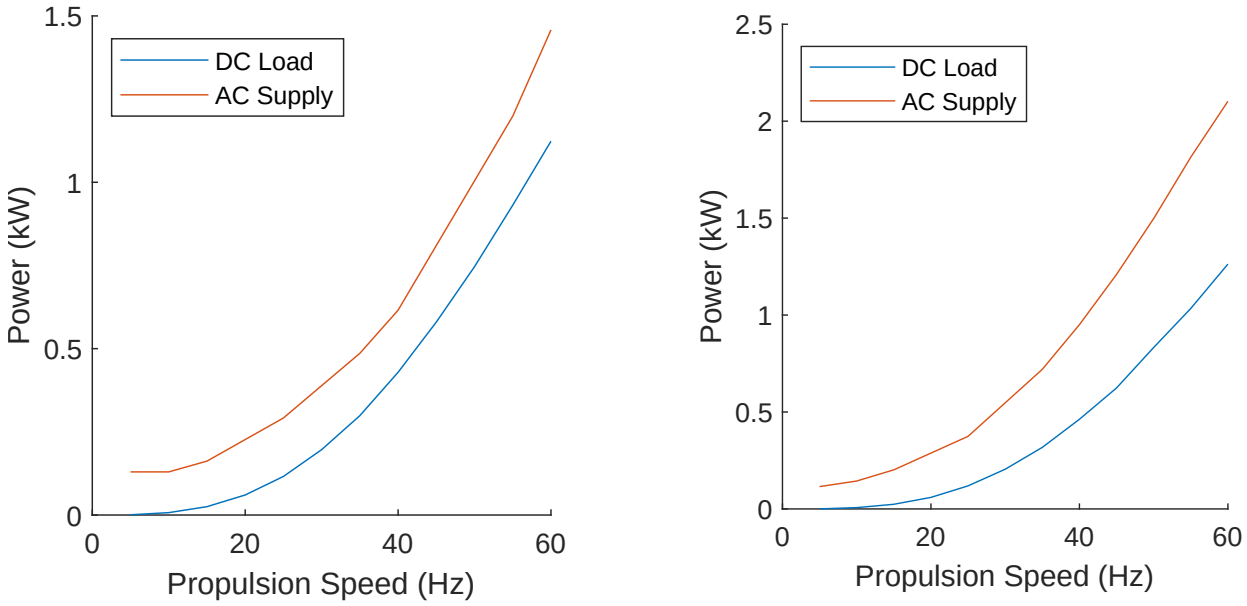


(a) System 1

(b) System 2

Figure 2.14: Propulsion Speed to Power

As shown above in Figure 2.14, The demanded load from the propulsion system is insignificant from 0-30Hz, from 30Hz to a full speed ahead of 60Hz, the system load increases by a magnitude of 6. The two subplots within Figure 2.14 represent the individual propulsion systems 1 and 2 and their respective speed to power curves. Propulsion system 1 has a more efficient variable frequency drive as compared to propulsion system 2. The variation in variable frequency drives is represented by the larger AC power draw for propulsion system 2 shown in Figure 2.14b as compared to the AC input power draw of propulsion system 1 shown in Figure 2.14a. The remainder of the system (3 phase induction motor, DC field

would machine, excitation system, and resistive load banks) are identical for both system 1 and system 2. The identical loads between the two systems is illustrated through the near identical DC load curves for systems 1 and 2 shown in Figure 2.14.

A summary of the signals for propulsion system 1 is provided below in Table 2.11.

Table 2.11: Propulsion System 1 Signals

| **Component** | **Signal** | **Units** |
|---|---|---|
| VFD | Phase A - Current | A RMS |
| VFD | Speed Command | Hz |
| VFD | Relay | I/o |
| VFD | Enable forward | I/o |
| VFD | Enable rev | I/o |
| DC Machine | Load Current | A DC |
| DC Machine | Load Voltage | V DC |
| Field Power Supply | Relay | I/o |
| Field Power Supply | Voltage Command | V DC |

The signals for propulsion system 1 shown above in Table 2.11 are identical for propulsion system 2. A visual of the as built propulsion systems are shown below in Figure 2.15.

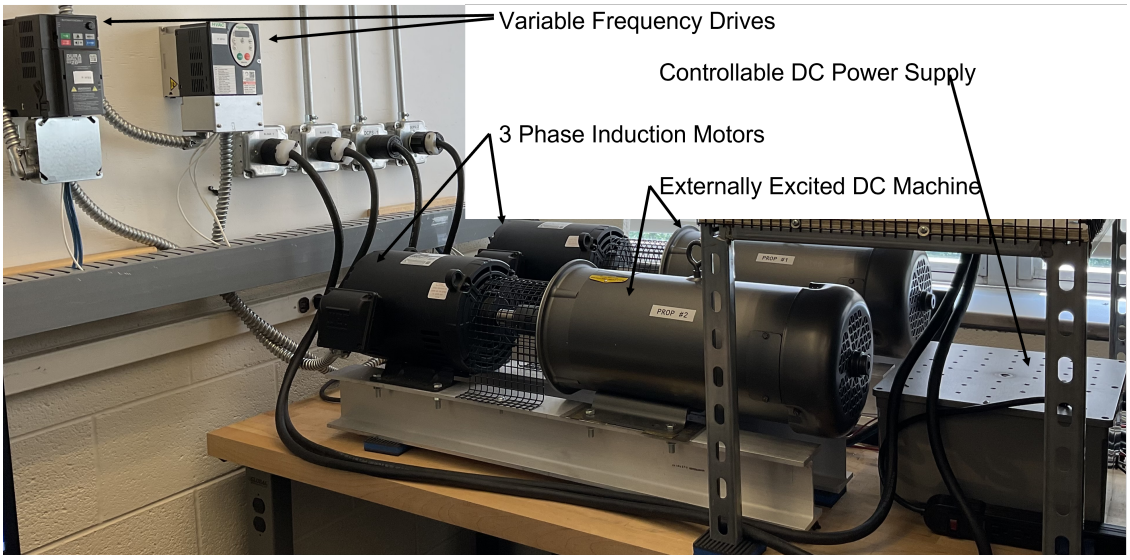


Figure 2.15: Propulsion Systems - as Built

Propulsion systems 1 and 2 provide the ability to place loads representative of real world all electric propulsion systems on the laboratory scale main switchboards and place corre-

sponding waste heat losses into the cooling system through a virtual linkage discussed in Section 2.4.

## 2.7 Mission System

The mission system consists of controllable three phase rectifiers (DC power supplies) and controllable DC resistive load banks (load banks). The DC power supplies are controlled as a function of maximum output voltage and maximum output current through the embedded control system. The DC load banks can be programmed in two modes. Mode 1 provides the ability to trigger pre-configured load profiles. Mode 2 provides the ability to commanded any desire load in amps DC within the limitations of the load bank capacities. The machinery plant contains two mission systems with capacities defined in Table 2.12.

Table 2.12: Mission System Specifications

| System | Parameter | Value | Unit |
|---|---|---|---|
| 1 and 2 | Power supply max output voltage | 100 | VDC |
| 1 and 2 | Power supply max current output | 50 | ADC |
| 1 | Load bank power | 2.6 | Kw |
| 2 | Load bank power | 5.2 | Kw |
| **1** | **System max load** | **2.6** | **Kw** |
| **2** | **System max load** | **5.0** | **Kw** |

Mission system 1 has a maximum of 2.6 kW, limited by the programmable DC load bank and mission system 2 has a maximum DC power dissipation of 5.0 kW limited by the DC power supply. A list of the signals for mission system 1 is provided below in Table 2.13.

Table 2.13: Mission System 1 - Signals

| Component | Signal | Units |
|---|---|---|
| DC Power Supply | Voltage setpoint | A DC |
| DC Power Supply | Current Limit | A DC |
| DC Load | Program Trigger | I/O |
| DC Load | Current Command | A DC |

The signals listed above in Table 2.13 for mission system 1 are repeated and identical for mission system 2.

Leveraging the mission system an example of a step load and pulse load with the subsequent generator dynamic response is show below in Figure 2.16 and Figure 2.17 respectively.

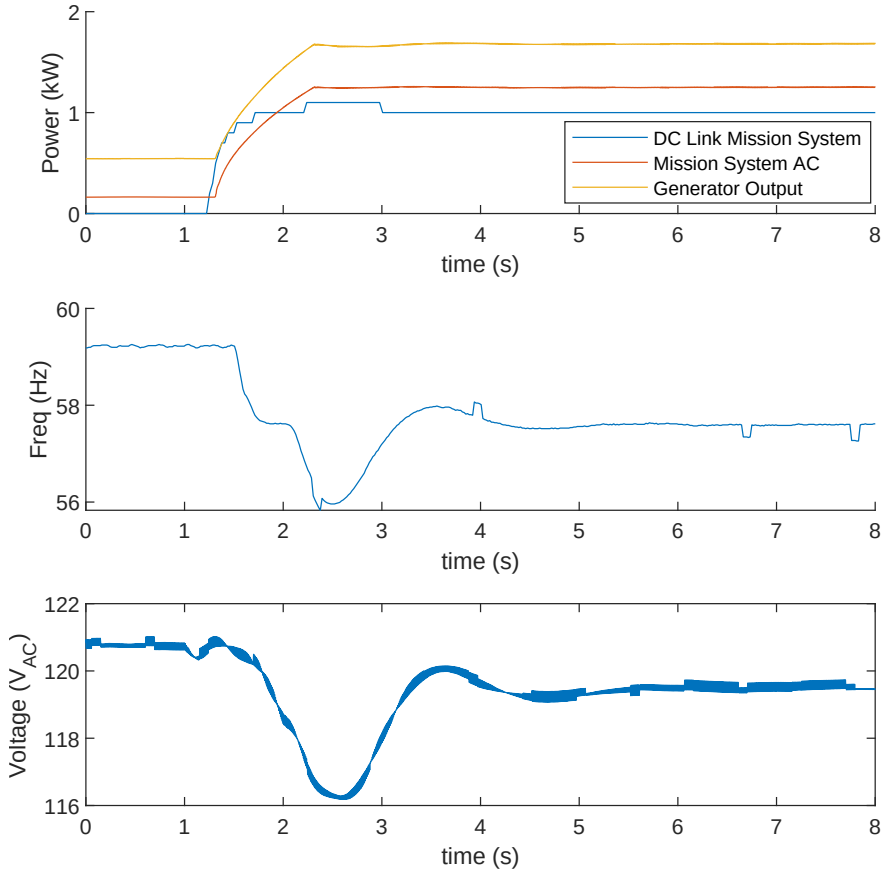


Figure 2.16: Example Mission Profiles and Generator Response - Step Load

As shown above in Figure 2.16, a commanded step from 0 to 1 kW DC to the mission system produced a slightly rounded square pulse drawn by the DC load bank (shown in blue). The DC power supply draw a lags the response of the DC load and has a rounded step increase from 0 to 1.15 kW as shown in red. The delay is a result of buffering from the internal DC power supply capacity and the difference in total load from 1 to 1.15 kW is a result of the internal losses for the mission system DC power supply. Shown in yellow depicts the total change in load on the generator supplying the load bank. The transient response in generator frequency and voltage is representative of the dynamics seen onboard real world vessels [35].

Similar to the output shown above in Figure 2.16, the response of the generator as a result of a pulse load is shown below in Figure 2.17 for a commanded pulse of 1 second on, one second off at 0.5 kW.

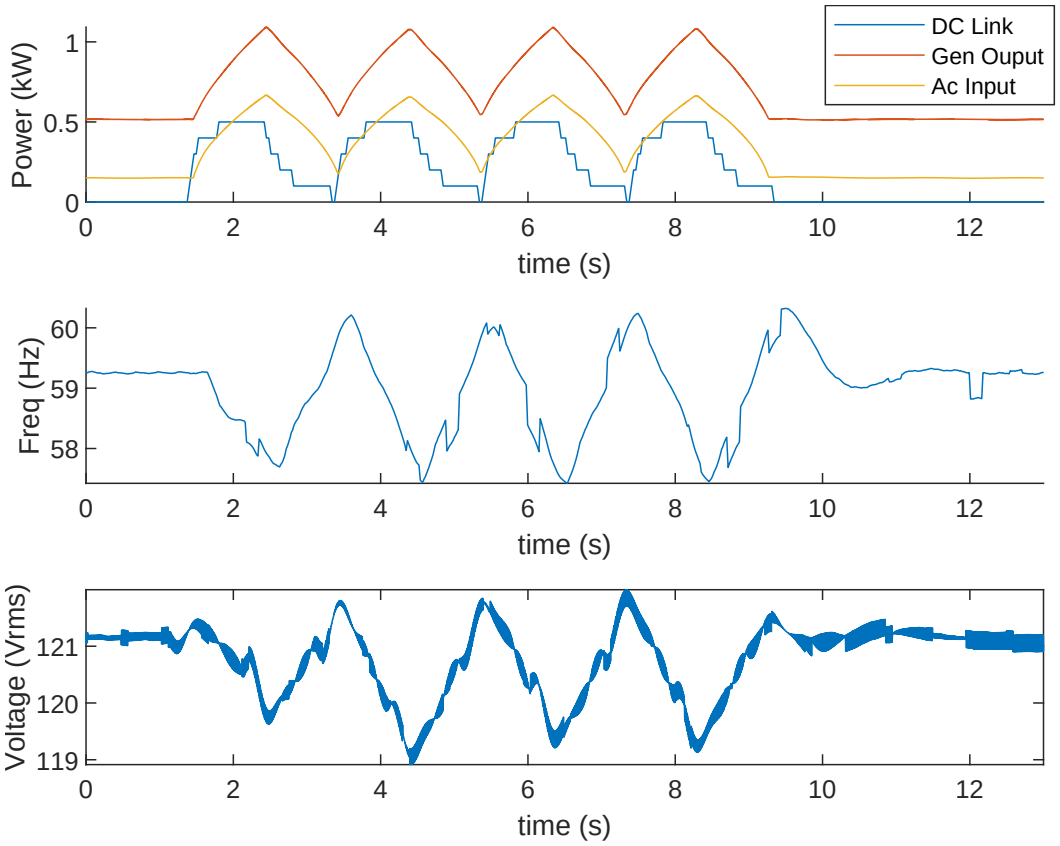


Figure 2.17: Example Mission Profiles and Generator Response - Pulse Load

As shown above in Figure 2.17, the first subplot of the figure depicts the jagged square shape of the power drawn by the DC load bank (shown in blue) followed by the response in power draw for the AC to DC power supply (in yellow) and generator output power (shown in red). Similar to the step load a rounded pulse in power is observed on the AC bus due to the internal buffering of the AC to DC power supply. The transient response for generator frequency and voltage are shown in the subsequent two subplots.

The integration of two sets of programmable load banks and AC to DC power supplies, configured to represent two shipboard mission systems, connected to both MSB1 and MSB2 allows for emulation of a wide variety of dynamic loads. The mission systems can emulate real world loads such as Electromagnetic Railguns, Electromagnetic Aircraft Launching System and Laser Weapon Systems. The ability to place any desired dynamic electrical load onboard both switchboards provides a large breath of hardware simulation capabilities.

Mission systems 1 and 2 provide the ability to place loads representative of real world all electric propulsion systems on the laboratory scale main switchboards and place corresponding waste heat losses into the cooling system through a virtual linkage discussed in Section 2.4.

## 2.8 NI Control and Data Acquisition System

### 2.8.1 Overview

The Multiphysics laboratory ship machinery plant leverages a National Instruments (NI) based control system for plant control and data acquisition coupled with a host PC for supervisory control inputs. An example page from the Host PC control system is shown below in Figure 2.18.

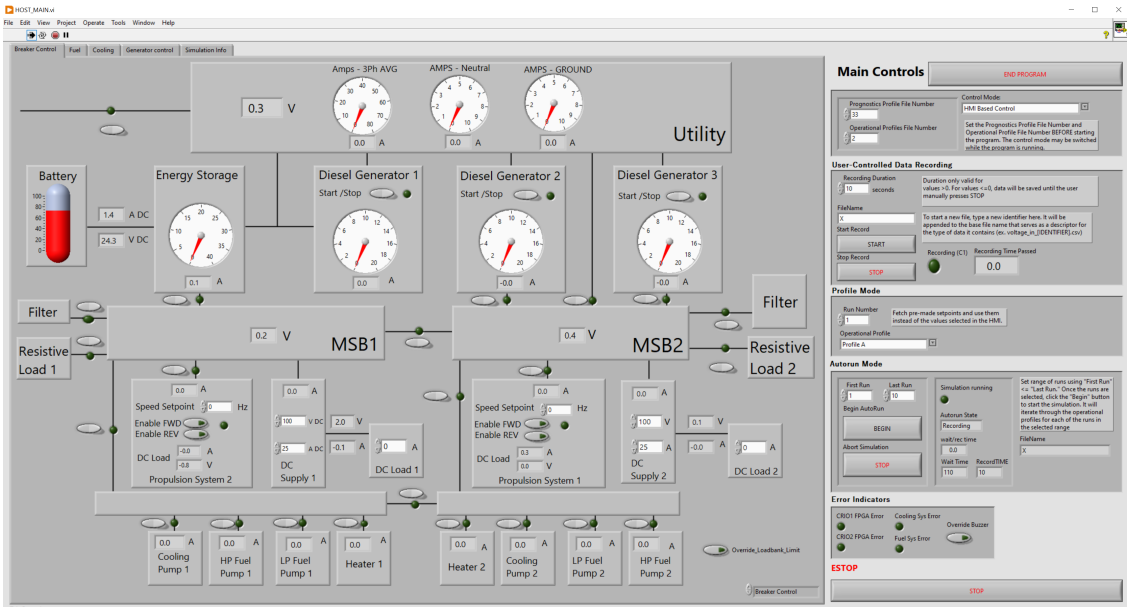


Figure 2.18: Control System - Host PC Interface

The integrated Hardware and software for control and data acquisition are further described in the subsequent three subsections. The first subsection defines the integrated NI hardware, followed by a discussion of the software control. The third and final subsection provides a summary of the embedded control system.

### 2.8.2 Integrated NI Hardware

The NI system consists of two CompactRIO's controllers, (cRIO-9045) with the following specifications: 1.30 GHz Dual-Core CPU, 2 GB DRAM , 4 GB Storage, Kintex-7 70T FPGA, and a 8-Slot chassis. Each of the 8 slots on both CompactRIOs are populated with I/O modules specified below in Table 2.14.

Table 2.14: CompactRIO Control Modules

| CRIO | Module Slot | Module | Module Type | I/o Channels | Sample Rate |
|---|---|---|---|---|---|
| 1 | 1 | 9208 | mA input | 16 | 500 S/s |
| 1 | 2 | 9208 | mA input | 16 | 500 S/s |
| 1 | 3 | 9208 | mA input | 16 | 500 S/s |
| 1 | 4 | 9264 | Voltage output | 16 | 25 Ks/s/ch |
| 1 | 5 | 9205 | Voltage input | 32 | 250 kS/s |
| 1 | 6 | 9485 | Relay | 8 | - |
| 1 | 7 | 9485 | Relay | 8 | - |
| 1 | 8 | 9485 | Relay | 8 | - |
| 2 | 1 | 9220 | Voltage Input | 16 | 100 kS/s/ch |
| 2 | 2 | 9264 | Voltage output | 16 | 25 Ks/s/ch |
| 2 | 3 | 9208 | mA input | 16 | 500 S/s |
| 2 | 4 | 9215 | Voltage input | 4 | 100 kS/s/ch |
| 2 | 5 | 9485 | Relay | 8 | - |
| 2 | 6 | 9215 | Voltage input | 4 | 100 kS/s/ch |
| 2 | 7 | 9485 | Relay | 8 | - |
| 2 | 8 | 9264 | Voltage output | 16 | 25 Ks/s/ch |

The integrated modules, listed in Table 2.14 are leveraged for control and data acquisition. All I/O signals across each chassis are recorded, when triggered, at sample rates defined in Table 2.15 below.

Table 2.15: CompactRIO Sample Rates

| CRIO | Module Type | Sample Rate | Units |
|---|---|---|---|
| 1 | Voltage input | 2500 | Hz |
| 1 | mA input | 30 | Hz |
| 2 | Voltage input | 2000 | Hz |
| 2 | mA input | 30 | Hz |

The two compactRIOS communicate to a host PC over a local Ethernet link. A visually summary of the physical hardware within the control system is show below in Figure 2.19.

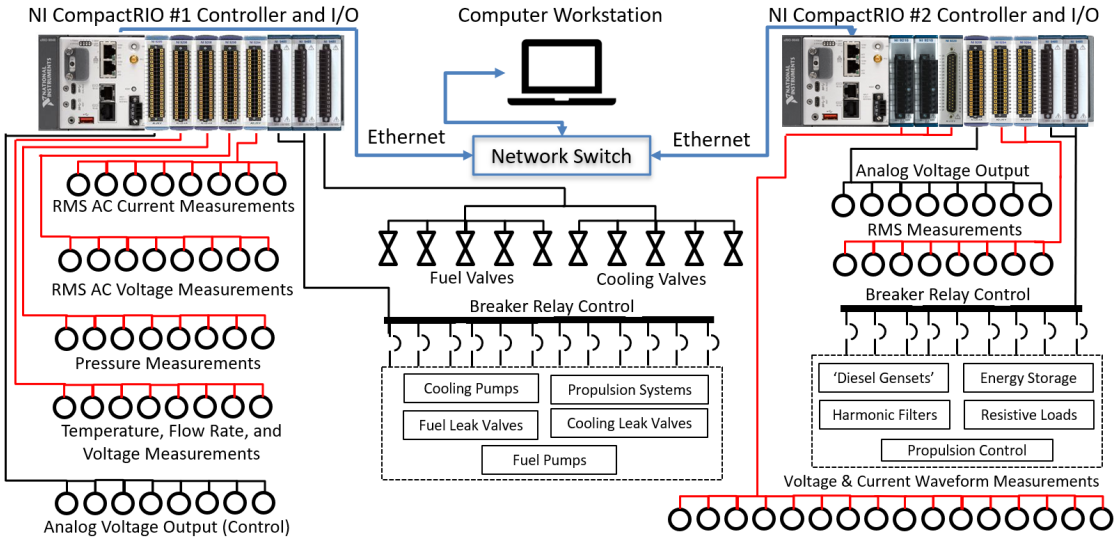


Figure 2.19: Control System - Diagram

The coupled integration of the control and data acquisition within one hardware system enables a large bandwidth of signals that can be acquired, continuously at high sample rates. This novel ability to save all laboratory signals provide an significant advantage for machine learning and AI integration when compared to the limitations of traditional systems containing a separate data acquisition device system and control system.

### 2.8.3 LabVIEW

### 2.8.4 Introduction

A LabVIEW software based control architecture was constructed using the two controllers and total of 208 I/O signals ports to provide the necessary machinery plant controls and virtual links between machinery plant systems.

### 2.8.5 Control Architecture

The embedded LabVIEW control software system optimizes CPU bandwidth and memory across both CRIOS and the host PC to enable real time control and data acquisition of the hardware machinery plant. The allocation of embedded resources is shown visually below in Figure 2.20.

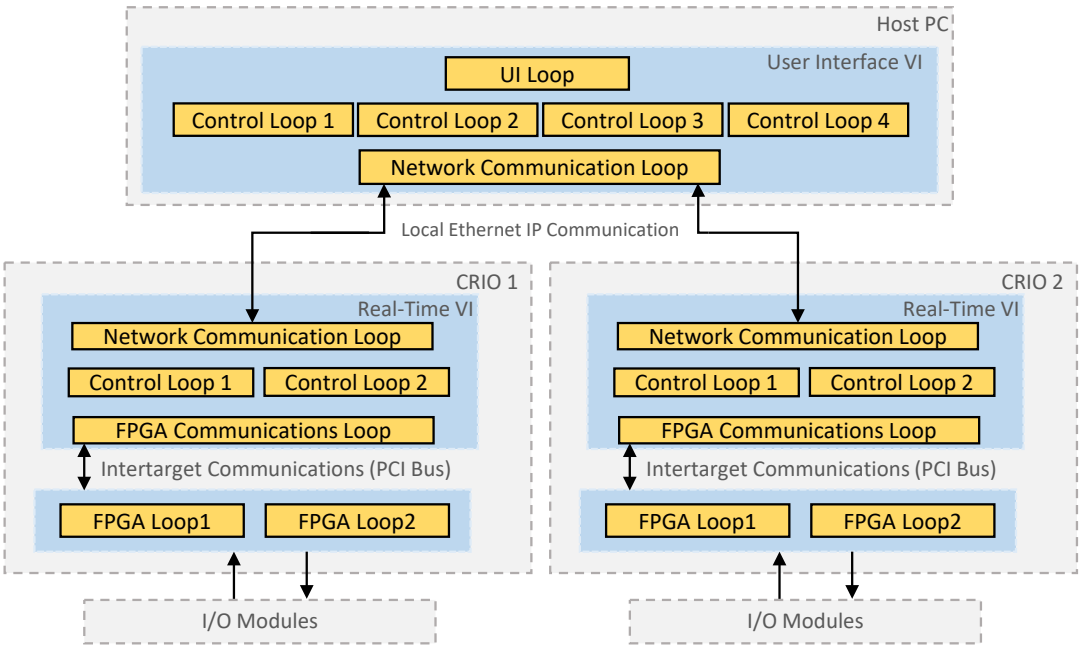


Figure 2.20: LabVIEW Software Control Process

As shown above in Figure 2.20, the software control structure consists of five core LabVIEW Virtual Instruments or VIs across the three devices. The processes executed within each VI are defined in the following three paragraphs grouped by device (Host PC, CRIO1 and CRIO2).

Host PC: The host PC contains a single VI containing six core process loops. A user interface or UI Loop is used to receive high level commands from a human user through the HMI interface and update high level plant values for the HMI display. The UI loop enables efficient buffering between the human user and other core processes within the host PC VI. A network communication loop is used to efficiently buffer values between the host PC and two CRIOS for real time communication over a local Ethernet TCP/IP connection. The four control loops contain various control functions for hardware system to system virtual connections that can afford the latency in control loop interaction to analog signal updates caused by the Ethernet communication time and CRIO real time to FPGA latency. Examples of these processes include: control mode selection and generator torque limits.

CRIO1: The embedded controller contains a real time VI and a FPGA VI. The real time VI is leveraged for communication with the host PC, communication with the FPGA VI and control loops 1 and 2. The Network communication loop follows the same process defined for the host PC. The FPGA communication loop buffers data from the FPGA loop for data acquisition, which is written to the local hard drive, and all control and HMI signals. This

buffer between the FPGA PCI bus and real time loop is necessary due to the variation in FPGA loop timing and the real time VI loop timing. The two control loops within CRIO1 contain various real time control processes such as: waste heat dynamics and fuel system dynamics. The FPGA VI contains two loops for data acquisition and control. The FPGA loops operate at varied sample rates defined in Table 2.15, where loop 1 contains the high sample rate signals and loop two contains the low sample rate signals. Both FPGA loops use a FIFO to stream data for acquisition to the real time VI. The FPGA loops contain additional controls that are best suited for FPGA logic. Examples of integrated FPGA logic include: breaker restrictions to avoid connection of unparalleled busses, pulse conversion to flow rate, propulsion system ramp rates and field control, and additional safety controls.

CRIO2: Follows the same architecture as CRIO1, with varied control processes within the real time and FPGA control loops. Examples of control processes within the real time loop on CRIO2 include: Generator frequency response dynamics, generator toque limits, generator voltage control and mission system control. Examples of control processes within the FPGA loop on CRIO2 include: Mission system rate limits, generator paralleling logic and control and additional safety controls.

### 2.8.6 Interface Control Modes

The HMI interface allows the user to select six different control modes for modification of high level plant controls in time. These modes are defined below:

1. HMI Based Control: This is the default control mode for the laboratory system. The user is able to manual adjust all desired high level plant controls through the Human Machinery Interface. In this mode, data is not recorded by default, however the user can record data using the HMI interface.

2. Mission Profile Control: This mode enables propulsion and mission system set points to be controlled by a modifiable CSV file located on the host PC, instead of through the HMI interface. In this mode, data is not recorded by default, however the user can record data using the HMI interface.

3. Mission Profile Group Control: This mode uses a modifiable CSV file located on the host PC to control the mission and propulsion system for a group of operational set points, each for a period of time seconds within the CSV file. In this mode, data is not recorded by default, however the user can record data using the HMI interface.

4. Mission Profile Group and Fault Injection: This mode allows fuel and cooling system faults to be injected at preset simulation times through an a CSV file located on the

host PC. In this mode operational parameters are also read in the same manner as mode 3. In this mode a simulation length and a full simulation length is defined and data is recorded for the length of the simulation.

5. TCP IP Control: Using this mode HMI control and indicators can be selected for control and observation from a remote device through a local Ethernet connection to an external device. The mode uses a group of registers with preset values that can be update over a TCP IP link to the local Ethernet network. This mode provides the ability for external devices to both read real time system parameters and control desired system set points. In this mode, data is not recorded by default, however the user can record data using the HMI interface.

6. Run to failure Control: This control mode provides the ability to inject and increase fault severity slowly until system failure occurs. A CSV file that contains all possible fault controls must be pre populated with the desired number of runs. Each run is a discrete set point for all fault triggers. For each run, the controller iterates across all operational points in the same manner mode 3 and records steady state data at each operational set point across every N number of runs.

The selection of the six control mode options is made on the side, permanent panel of the host HMI through a drop down menu. The selection of the available control modes is shown visually below in Figure 2.21.

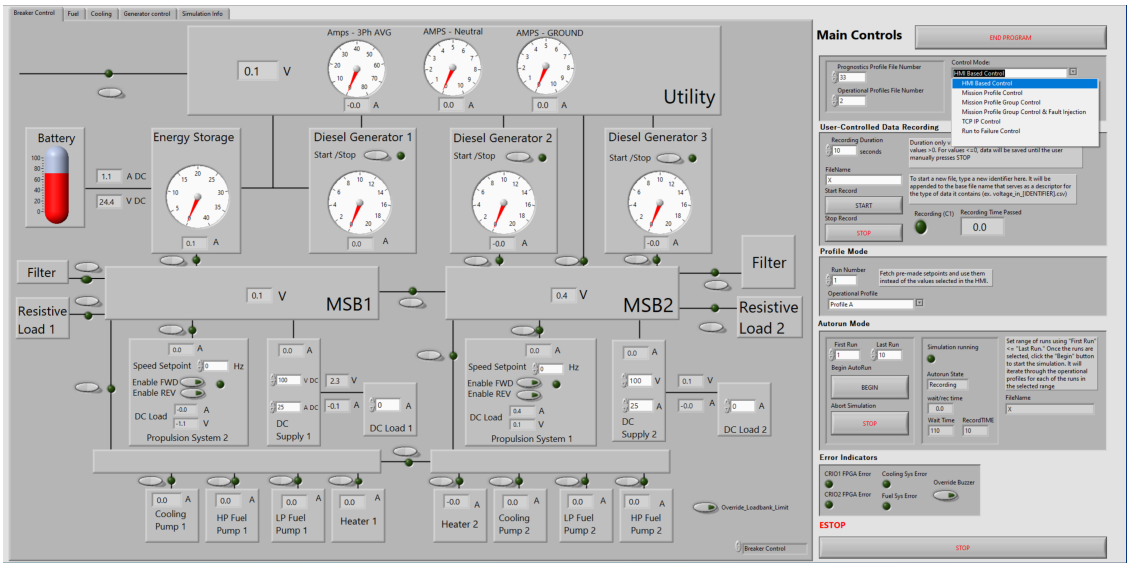


Figure 2.21: HMI Control Modes

Through the integration of preset control modes users can efficiently operate the laboratory ship machinery plant for a wide breadth of experimental simulations and data acquisition.

### 2.8.7 Summary

The embedded control system provides a singular system for data acquisition and control of systems and their interdependencies within the MLSMP. The system allows users to leverage programmed control modes to modify high level system controls through an HMI. The system leverages two real time controllers, a host PC and over 200 analog channels for control and data acquisition. The control architecture effectively leverages resources at the FPGA, real time and host PC levels to efficiently complete the necessary control and data acquisition tasks in real time.

## 2.9 Post Processing of Acquired Data

The LabVIEW control and data acquisition system defined in Section 2.8.4 enables data acquisition for a single user initiated record instance and for the acquisition of data from an automated LabVIEW control process which records several instances over a desired simulation. The automated LabVIEW control process is defined in detail in Chapter 4. In both acquisition processes, raw data from CRIO 1, CRIO 2, and the Host PC is written to CSV files, which requires a post processing code to scale the raw data into usable engineering units. To do so, two post processing codes are constructed and leveraged throughout work in this dissertation. The final version of the processing code was made by Manohar under work completed in PhD dissertation [36] and publication [37].

The processing codes performed three core functions and were identical for both versions. The processing codes scaled the raw output signals to place signals in engineering units (flow, pressure, etc.) for each signal acquired. The processing codes scaled the signal time vector to have simulation start time of 0 seconds, instead of the current clock time of the FPGA acquisition device. Finally the codes provided the average value of each signal for the given simulation run. The two versions differed in the type of hardware simulation conducted.

Processing code A was formed to process a single simulation record instance. Version B was designed to process Failure Profiles (s), define in detail in Chapter 4, where a failure profile consisted of up to 10 runs and each run contained three record instances. Each record instance corresponded to an operational profile, also defined in Chapter 4. The file structure, and user commands are defined as in the following two subsections.

### 2.9.1 User Interaction

The user commands to use the two versions of code are as follows:

Version A: The user will call the python script `PostProcess_SingleSimulation_V1.py` using the command window with the following input string. [`PostProcess_SingleSimulation_V1.py` FilePath datasetNum]. The file path will lead to the location of the desired folder to process. The required contents of the folder are defined in a following section.

Version B: The user will call the python script `PostProcess_FailureProfile_V1.py` using the command window with the following input string, [ `PostProcess_FailureProfile_V1.py` FailureProfileStart FailureProfileEnd Dataset_X], where FailureProfileStart is the first failure profile to process and FailureProfileEnd is the last failure profile to process. Dataset_X is the dataset the failure profiles are located within. The path for this version will be preset within the code itself for ease of use on the local lab computer.

### 2.9.2 File Structure

Both instances of the python code are located on top level of the file structure on the host PC. The location the top level of this path is used in when using version A and written into the code itself when using version B. Both versions of the code use the same top-level folder, as shown below.

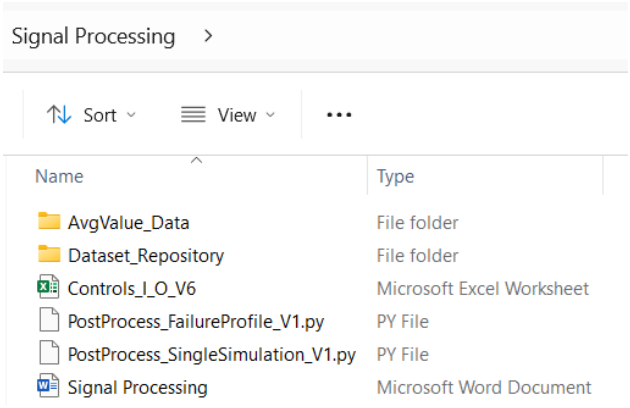


Figure 2.22: Base Folder for Data Processing

The main folder contains the files shown above with a single sub-folder. The sub-folder contains both datasets, as shown below.

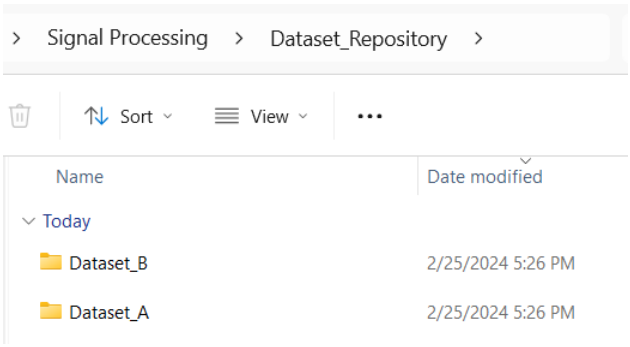


Figure 2.23: Datasets A and B for Data Processing

The sub-folder shown above contains two Datasets, `Dataset_A` provides an example of the substructure for processing code Version A and `Dataset_B` provides an example of the substructure for processing code version B.

The file structure for using version A of the code is shown below in Figure 2.24.

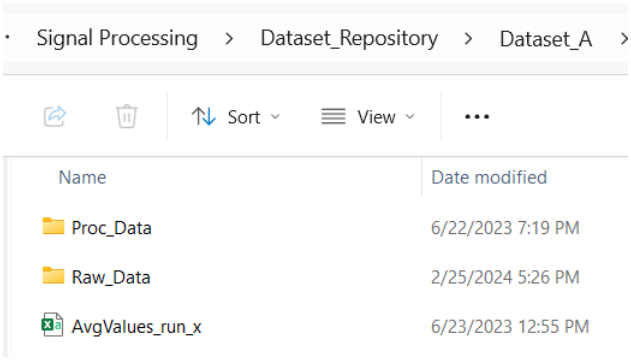


Figure 2.24: Version A Base File Structure

An example of the raw files is provided below in Figure 2.25.

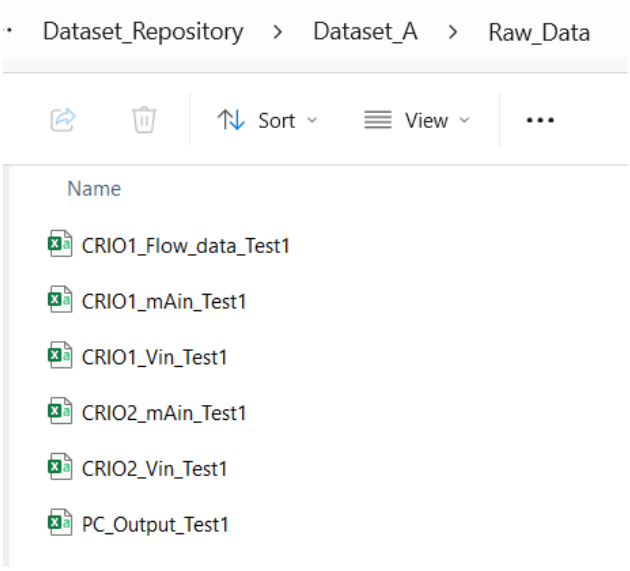


Figure 2.25: Version A Required Files

Using version the `Raw_Data` folder would exist with the files shown above and the `Proc_Data` folder would be generated along with the `AvgValues_run_x.csv` file.

Using version B of the post processing code, the following folder structure shown in Figure 2.26 is required prior to calling the function in python.

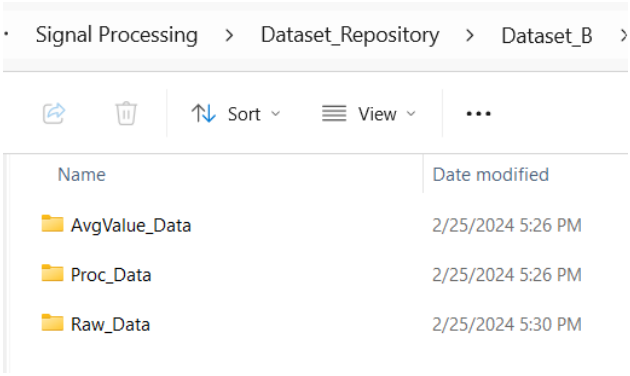


Figure 2.26: Dataset B Base Folder

The `Raw_Data` folder requires populated Failure Profiles as shown below in Figure 2.27.

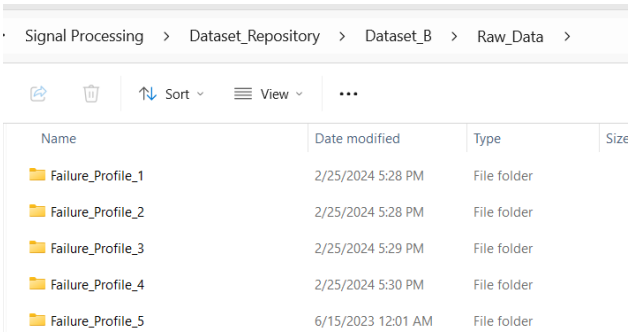


Figure 2.27: Dataset B - Input Data Folders

Where each file folder contains all recorded files for a given profile. After calling the processing code, processed time series data is generated and archived alongside average value data for each record instance. An overview of the average value data is provided followed by an overview of the time series data.

For each failure profile, as shown below in Figure 2.28, average value data is provided for each of the three operational profiles (record instances) as shown in Figure 2.29.

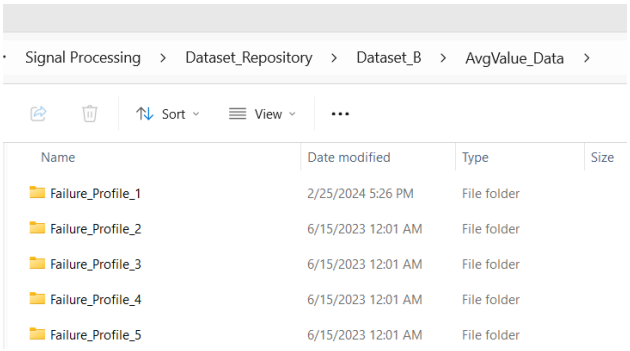


Figure 2.28: Dataset B - Output Average Value Data Folders

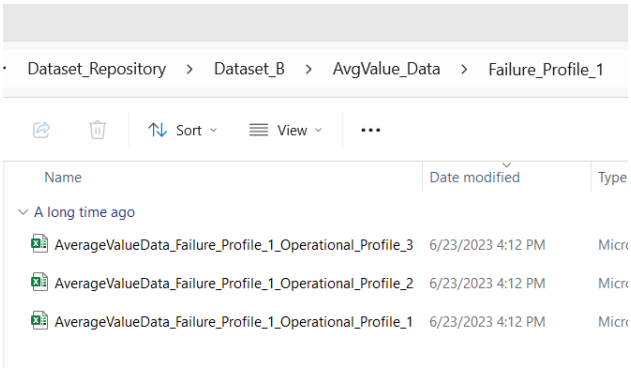


Figure 2.29: Dataset B - Output Average Value Data Files

In a similar process for each Failure profile, process data is stored by Failure profile, then sequence point, then operational profile. The failure profiles are shown below in Figure 2.30.

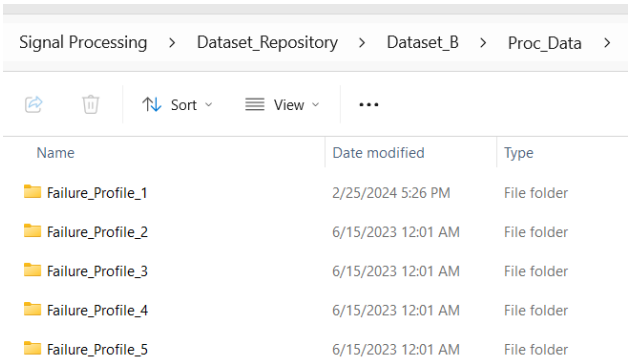


Figure 2.30: Dataset B - Output Time Series Data Failure Profiles

Each Failure profile contains the subsequent sequence points as shown below in Figure 2.31.

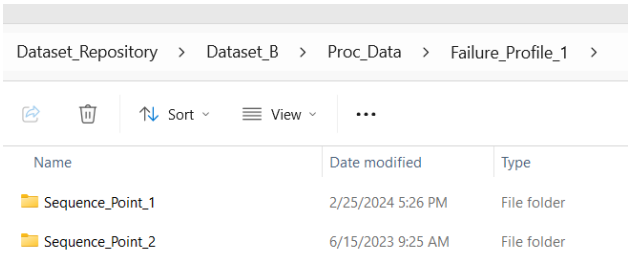


Figure 2.31: Dataset B - Output Time Series Data Failure Profile Folders

Each sequence point contains the subsequent operational profiles as shown below in Figure 2.31.

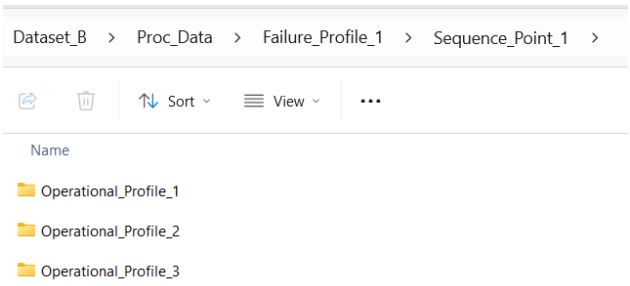


Figure 2.32: Dataset B - Output Time Series Data Operational Profile Folders

Each operational profile contains the subsequent operational profiles as shown below in Figure 2.31.

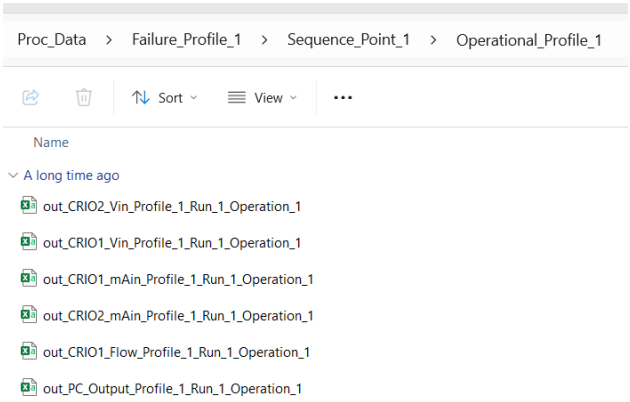


Figure 2.33: Dataset B - Output Time Series Files

### 2.9.3 Summary

The processing code with versions A and B enables the efficient and uniform post processing and achieving of hardware simulation data for work throughout this dissertation and future laboratory use.

## 2.10 Exemplary Multi-Physics Simulations

To showcase the capabilities of the novel multi-physics physical hardware plant and illustrate potential fault mitigation techniques, three example hardware simulations are conducted. The three simulations adopt and apply common fault mitigation techniques in an unconventional manner. The three common techniques are inspired by the following adoptions in other domains and are as follows:

- Load shedding: A well established mitigation technique for overloading of systems and optimization of load shedding for ship applications is prevalent in current research [38–41].
- Droop control: Traditionally used to balance power output in parallel generator applications. This well established principle has been implemented for renewable inverter applications to improve active power sharing in paralleled two-stage PV inverter systems improving overall system resilience [42].
- Energy storage: Has been well studied in current research for topics including mitigation of overloading at peak load, improvement of fuel economy and system fault mitigation [43, 44].

The first simulation showcases the injection of a cooling system leak and the subsequent plant response. Using a load shedding technique, the control system reduces the plant load to mitigate an overheating fault in the cooling system. The second simulation showcases injection of a fuel system fault and the subsequent multi-system response with the use of a sole generator and energy storage. The third simulation leverages a parallel generator configuration with the injection of a cooling system fault. A load sharing technique is implored to mitigate an overheating fault.

### 2.10.1 Fault Injection - Load Shedding

This simulation was presented at [2] and is provided in this subsection to form a complete document of work completed in fulfillment of this PhD.

This simulation uses the notional mission scenario with time variant propulsion and mission loads, depicted in Figure 2.34.

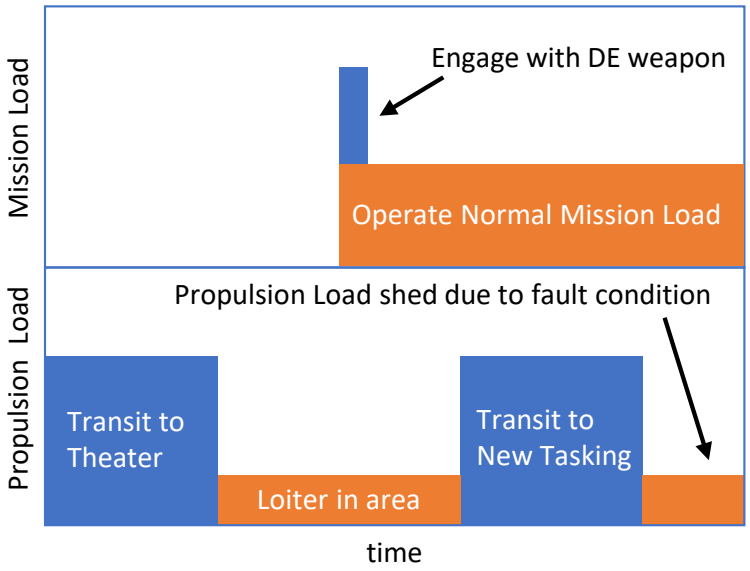


Figure 2.34: Mission Scenario from [2]

Using the mission scenario depicted in Figure 2.34. The cooling system began in a full health condition at the start of the simulation. Shortly after the simulation started, a leak was injected into the cooling system. The injected leak is shown in Figure 2.35, where a sharp drop in system flow rate is observed. A rise in temperature is also observed across the cooling system flow path, however the nominal change in heat rise does not exceed the system limit. A small change in pump current is also experience at the injection of a cooling system leak as shown in Figure 2.35, this response indicates potential for leak detection using pump current as a input signal.

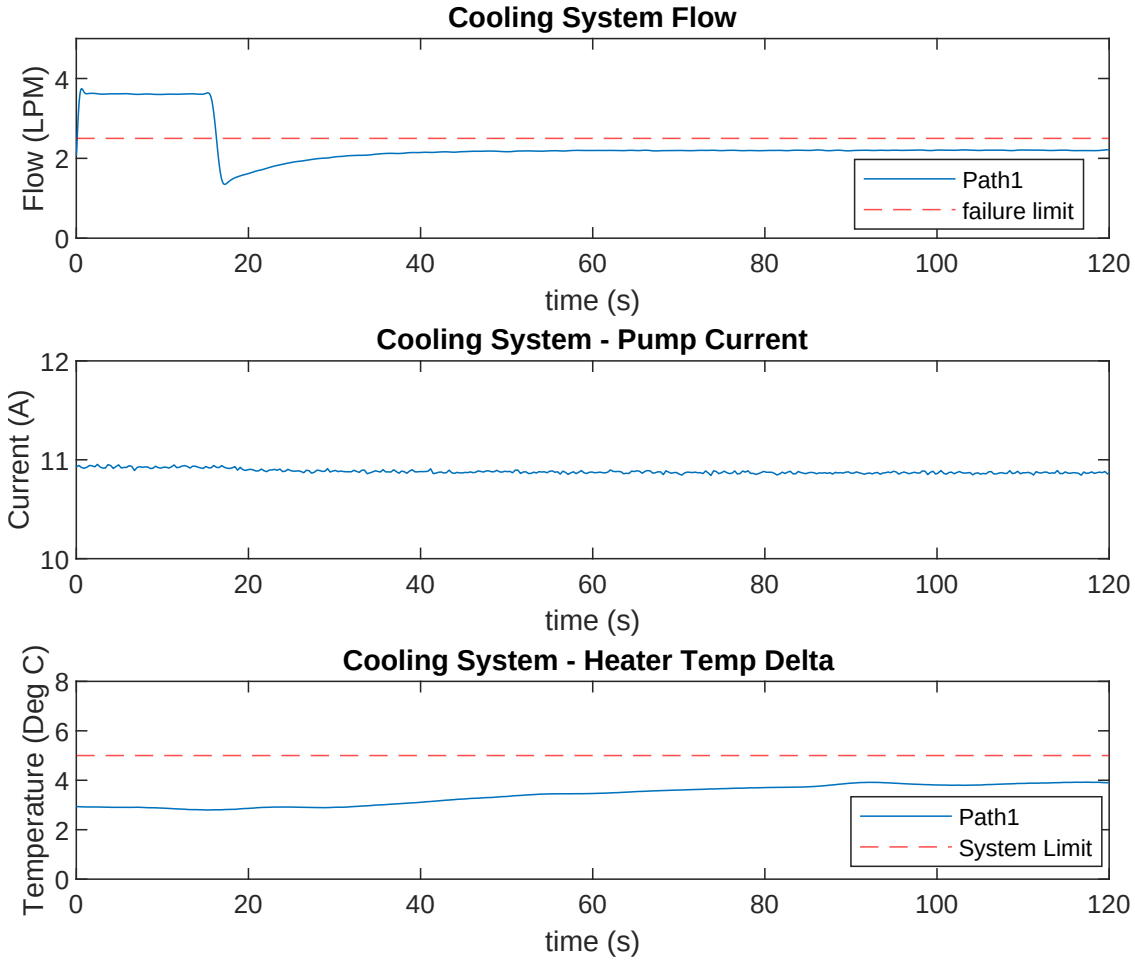


Figure 2.35: Cooling System Fault Injection with Load Shedding from [2]

As the mission scenario continues the high propulsion load in conjunction with the high mission system load causes an increase in thermal rise across the cooling system which exceeds the thermal limit of the cooling system as shown in Figure 2.36.

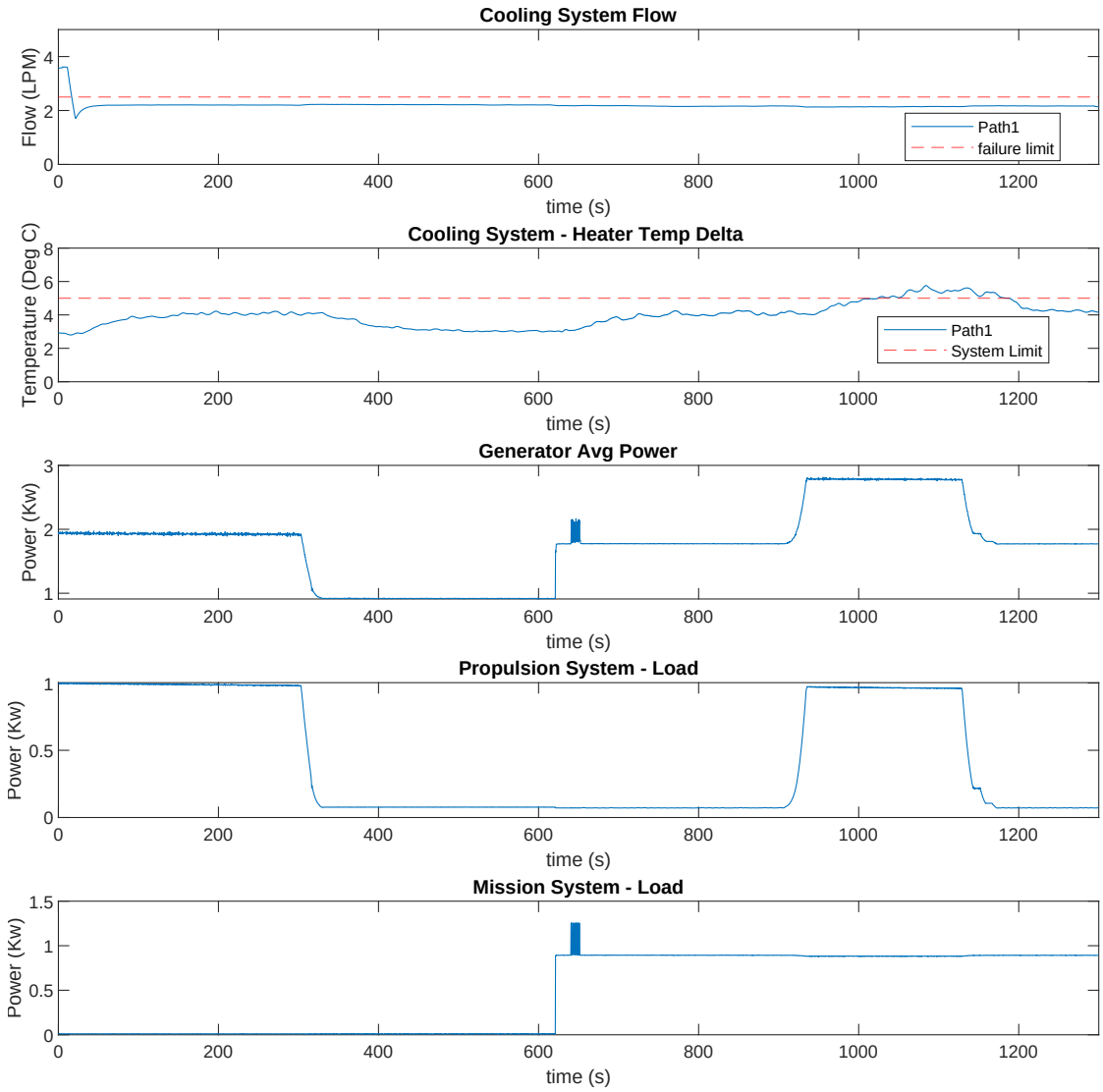


Figure 2.36: Cooling System Fault Mitigation with Load Shedding from [2]

To mitigate this fault the propulsion load is reduced allowing the mission system to continue at its desired load and reducing the thermal rise across the cooling system within the system limits as shown in Figure 2.36 above.

### 2.10.2 Fault Injection with Energy Storage

A high pressure fuel system leak is injected at the start of this simulation. The fuel leak cause an insufficient amount of flow through the injector. The error in fuel flow (demanded fuel vs. actual) placed a virtual limit on the generator output torque. The limit imposed on the emulated generator set results in a drop in generator frequency resulting in the generator tripping offline. As the generator began to lose stability the energy storage system

supplemented the energy demanded by the loads. When the generator was unable to produce sufficient capacity to remain online and tripped, the energy storage system became the sole source. This dynamic response is shown visually below in Figure 2.37.

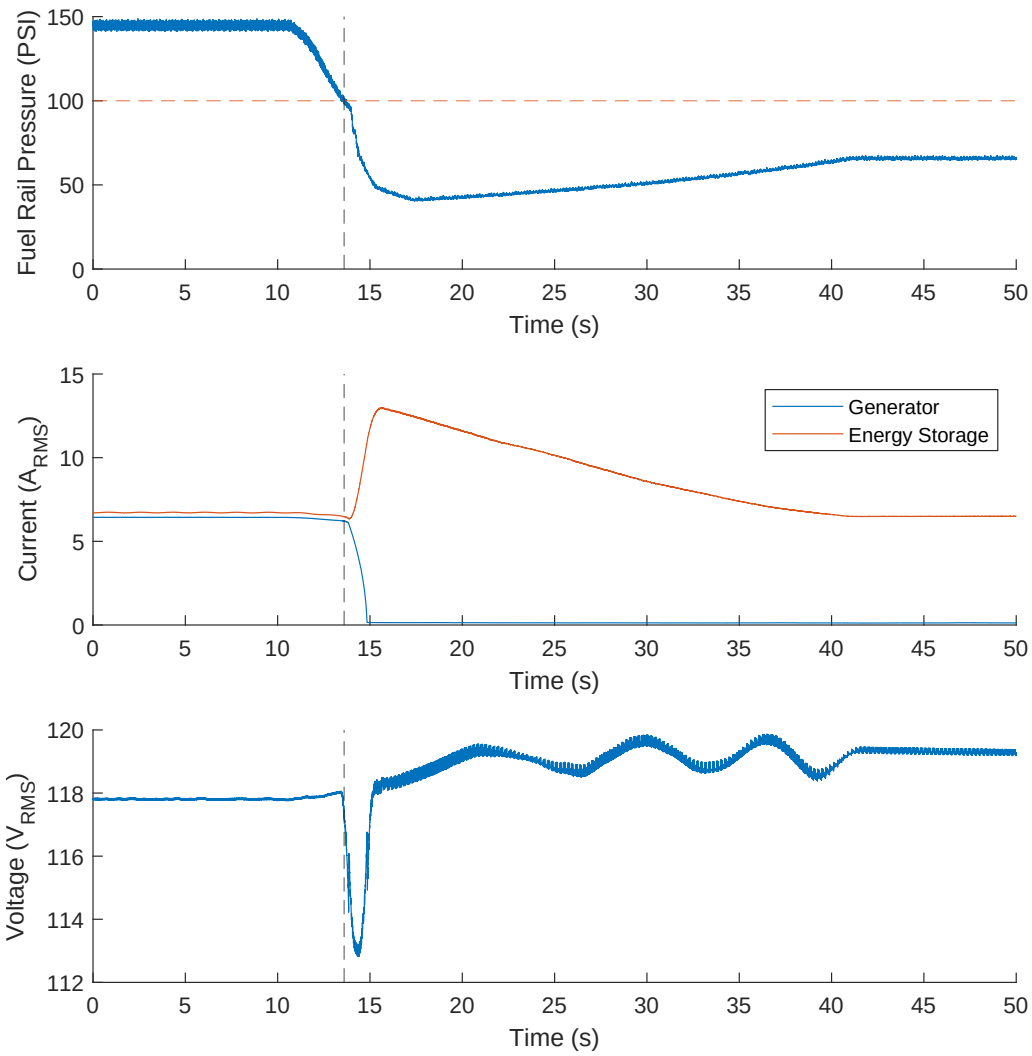


Figure 2.37: Plant Response - Generator Fuel System Failure with Energy Storage Backup

### 2.10.3 Fault Injection with Paralleled Generators

This simulation was conducted to predict the laboratory plant machinery systems ability to operate in parallel and simulate, in hardware the effect and recovery of a fault in one of the two supporting cooling systems. The hardware simulation began with generators 2 and 3 online, both providing 50% of the total plant load. The ship machinery plant had both propulsion units online at a rate of 30Hz and the mission system with a load of 1 kW each

for the duration of the simulation. Resistive loads 1 and 2 were also online as well as both fuel and cooling systems. Fuel system 1 supported generator 2 and fuel system 2 supported generator 3. Cooling system 1 supported losses from propulsion and mission system 1 as well as generator 2. Similarly, Cooling system 2 supported losses from propulsion and mission system 2 as well as generator 3.

At the start of the simulation all systems were in full health with no faults or failures injected. Once the simulation started, a clog was injected into the cooling system 1. The clog reduced flow across waste heater 1, which subsequently caused the temperature to rise over the overheating threshold. To combat the system overheating, a load with high losses (mission system) or the generator output would have to be reduced. Given the ability to load share the generator load from generator set 2 was reduced by 40 %, causing generator 3 load to increase by 40 %. The shift of power output between generator 2 and 3, reduced the required waste heat dissipation for the faulted cooling system, causing the temperature across the heater to reduce back within safe operating levels. This is shown visually in Figure 2.38 below.

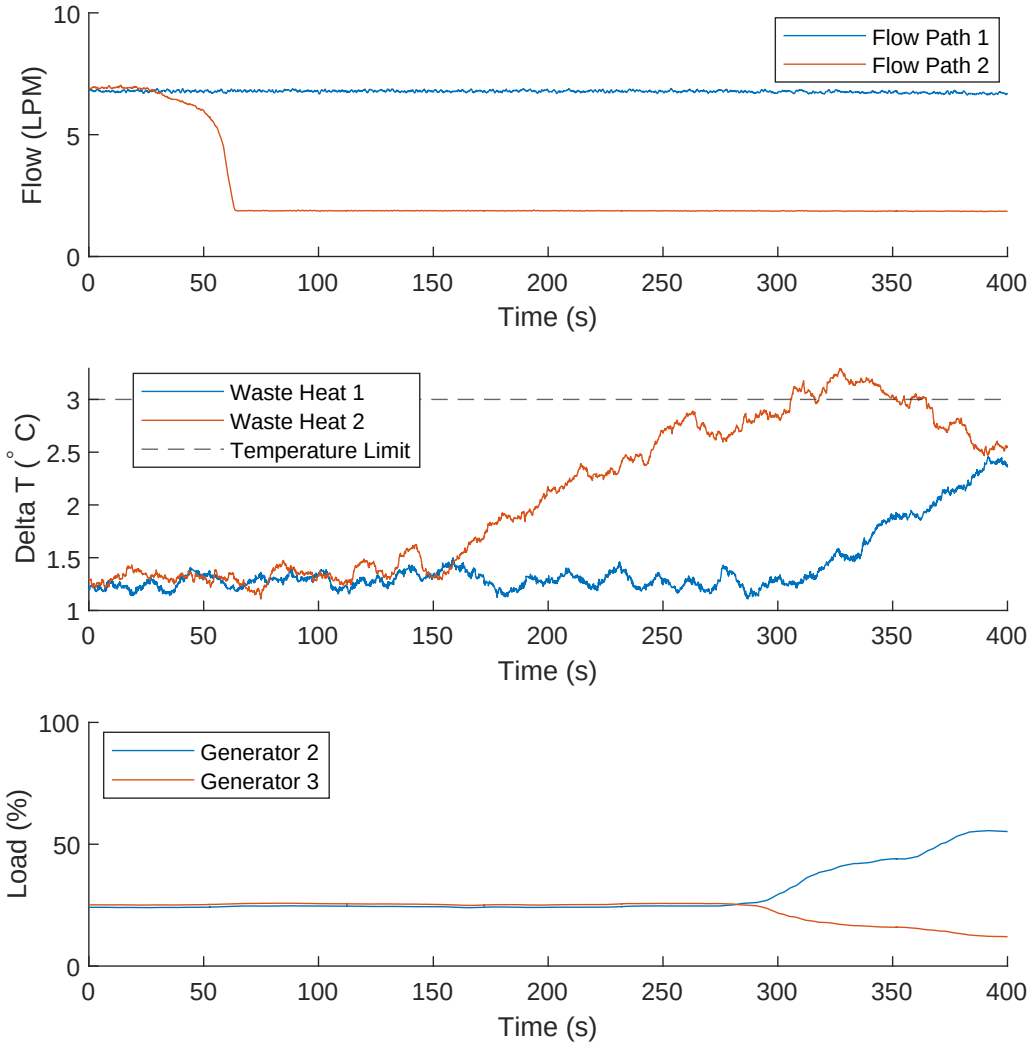


Figure 2.38: Plant Response - Cooling System Fault with Parallel Generators

As shown above in Figure 2.38, by shifting 40 % of the load from generator 2 to generator 3 all system loads were able to remain online and system overheating was effectively mitigated. It is also noted that heater 2 showed an increase in temperature across the heater due to the increase load on generator 3 and subsequent system losses.

As shown through this exemplary simulation, the laboratory scale ship machinery plant has the ability operate with generators in parallel, shift load sharing and emulate effects of support system faults such as clogging and their effect on the overall machinery plant.

### 2.10.4 Summary

This section showcased the capabilities of the novel multi-physics physical hardware plant and illustrate potential fault mitigation techniques through three exemplary simulations.

The three simulations adopted common control strategies inspired from literature to improve operational resilience in the presence of a system fault. This section provides insight into the potential to mitigate faults and maintain operational availability using real time control. Plant health, both its current state and predicted future state are essential inputs to build future control based, fault mitigation techniques. These example simulations provide motivation for to explore plant level prognostics and diagnostics.

## 2.11 Summary Laboratory Ship Machinery Plant

This chapter provided a detailed overview of the laboratory scale ship machinery plant (MLSMP) that was designed, constructed and validated with the necessary physical and virtual system interconnections to accurately represent plant dynamics and common faults of machinery plants found on vessels in the real world. The MLSMP leverages physical and control based system to system linkages to enable the injection of common faults and operation of the MLSMP to failure without damaging the physical hardware within the laboratory. The MLSMP provides the capability to simulate in hardware run to failure profiles for common faults and failures of machinery plants and explore potential to improve operational resilience in an unmanned ship machinery environment environment through unconventional control mitigation techniques. A Visual overview of the laboratory scale machinery plant is shown below in Figure 2.39.

Figure 2.39: Visual Overview of the Novel Laboratory Scale Ship Machinery Plant

# CHAPTER 3

# Initial Application of Artificial Intelligence for Cooling System Health Prediction

This chapter is provided largely as a direct quotation from work presented at the Intelligent Ships Symposium in May of 2023 [45] (denoted by material indented in this chapter). The inclusion of content as a block quote provides a singular document of work completed as part of this PhD. A brief overview of this work and its relevance in this dissertation is first provided prior to the direct quotation of four sections, Sections 3.1- 3.3. A summary is provided following the direct quotation of work from [45]. Small modifications to the original content have been made to avoid duplication of the already defined in Chapter 2 relating to the University of Michigan laboratory-scale ship machinery plant or MLSMP.

As a first step in the application of Artificial Intelligence (AI) to the MLSMP, temperature and current data from the laboratory cooling system (defined in Chapter 2 ) were selected as inputs to AI driven algorithms for fault detection and the prediction of current system capability, given a randomized and degraded state of health. The cooling system was selected due to the common system faults of clogs and leaks. Both types of faults, clogs and leaks, were injected in the cooling system to produce varying states of system health and result in a reduction of cooling capability. The presence of a leak in a flow path on its own can be easily detected through various sensor readings; indicated by a drop in pressure on the outlet of the system pump, an increase in overall flow out of the system pump, and a change in pump electrical draw. However, in conjunction with an unknown state of flow path clogging in time leaks become difficult to detect as both faults (clogs and leaks) affect system dynamics and are interdependent to each other [46]. As a result, the cooling system leveraged for this paper provides a complex system with interdependent faults that cause degradation in system capability. To address the detection of a fault (i.e, a leak) and predict the current cooling system capacity given an unknown and degraded state, two applications of AI are used. The first application uses pump current as input data to explore a k-nearest neighbors (KNN) algorithm to detect a cooling system leak in the presence of an unknown state of

system clogging. The second application of AI explores the use of a long short-term memory (LSTM) recurrent neural network (RNNs) to project temperature rise within the cooling system for a step increase in loading from 20 % to 100 % thermal load.

## 3.1 Input Data Collection

To obtain datasets for the two AI applications of prognostics in this paper the cooling system waste heat control was preprogrammed for two unique waste heat profiles as a percentage of max emulated waste heat. Profile A simulated and injected a step-in waste heat loading from 10 % to 20 %, simulating a small step increase in plant loading, for example turning on a mission radar system. Profile B simulated and injected the full amount of waste heat (100 %), simulating the machinery plant at 100 % load, which relates to the generators at max output caused by high mission system loading and propulsion system loading. The two waste heat profiles and the respective system loading are shown in Figure 3.1

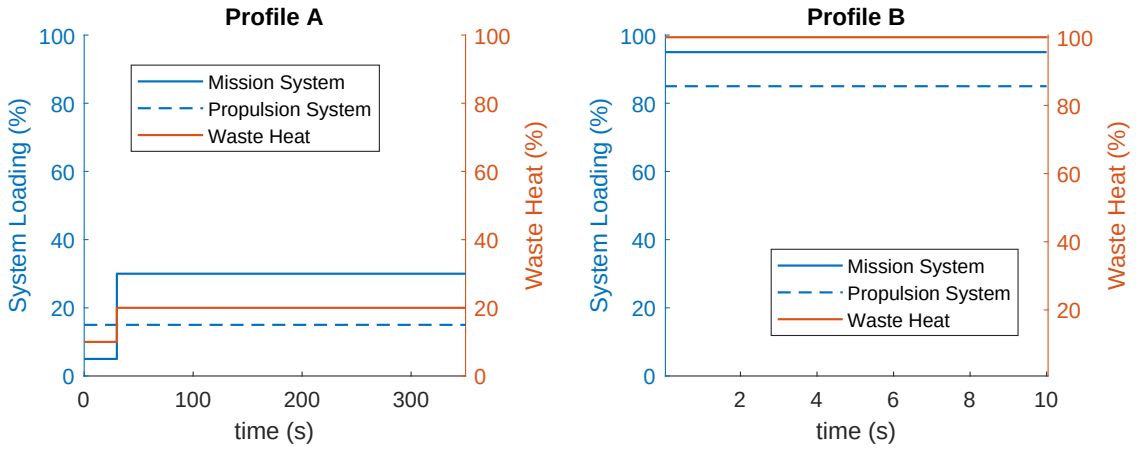


Figure 3.1: Mission Profiles

The two waste heat profiles A and B were injected into the cooling system through the use of heater 1, as defined in Chapter 2.

Service pump 1, illustrated in Figure 2.7, was placed online to provide flow through heater 1, dissipating the injected heat from profile A and B. To produce a rich dataset, containing random states of system health, with a varied and degraded ability to remove waste heat, a set of 100 randomized fault conditions were constructed, defined as runs. For each simulation run the state of health is degraded through the injection of

a randomized combination of leaks and clogs. For leaks a binary position of Leak/No leak was generated. For clogs a randomized value 0-80 % is generated in discrete integer values i.e. (0 %, 1 %, 2 %), these values correspond to a proportional globe valve position. For each run, two cases are recorded, using waste heat profile A and B. Case A, uses profile A and places the heater at steady state with 10 % loading and records a step response to 20 % loading. Case B places the heater at 100 % loading and records the steady state behavior. For all 100 unique states of health and each of the two loading cases the temperature across the heater ($T1_2 - T1_1$) and AC RMS line current to pump 1 was recorded. The data was then processed to produce input data for the two prognostics AI applications. The temperature delta across the heater for both cases A & B were combined by concatenating temperature data from case B onto the end of case A. These two cases were combined to leverage a times series prediction network, attempting to predict case B given case A (i.e., predict the temperature rise at max load given a small step change in loading caused by the mission radar system being placed online). Additionally, for each run the dynamics of the fluid flow and load on the pump were considered constant, so an average value of pump current was obtained for each of the 100 runs. Figure 3.2 provides 4 (of 100) temperature responses for case A and case B and Table 3.1 provides the average pump current draw for these 4 runs.

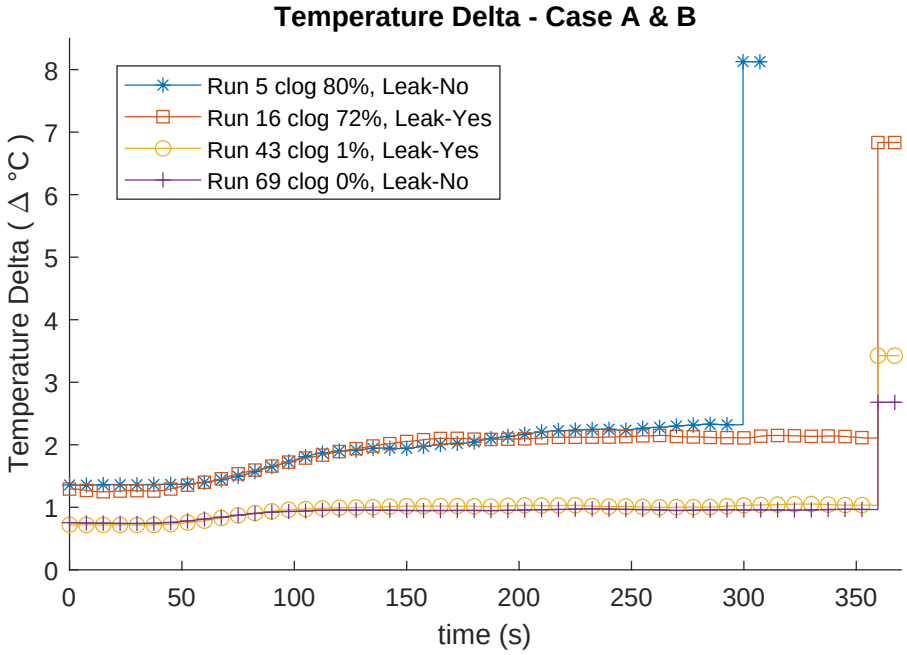


Figure 3.2: Example Runs (Case A and B)

The four exemplary outputs depict responses near the four unique boundary cases, where the state of health is: near the max boundary of clogging without a leak (Run 5), near the max boundary of clogging with a leak (Run 16), near the min boundary of clogging with a leak (Run 43), and near the min boundary of clogging without a leak (69). The corresponding average pump current draw across case A and case B is provided below in Table 3.1.

Table 3.1: Example Runs - Average Current

| **Run Number** | **Clog (%)** | **Leak Status** | **Current (Amps)** |
|---|---|---|---|
| 5 | 80 | No Leak | 10.91 |
| 16 | 72 | Leak | 10.53 |
| 43 | 1 | Leak | 9.55 |
| 69 | 0 | No Leak | 10.23 |

The 100 unique current values in amps correlating to each of the 100 randomized states of health will be used as the first set of input data for the application of leak detection in the subsequent section.

A histogram of the temperature rise for profile A and B is provided below in Figure 3.3.

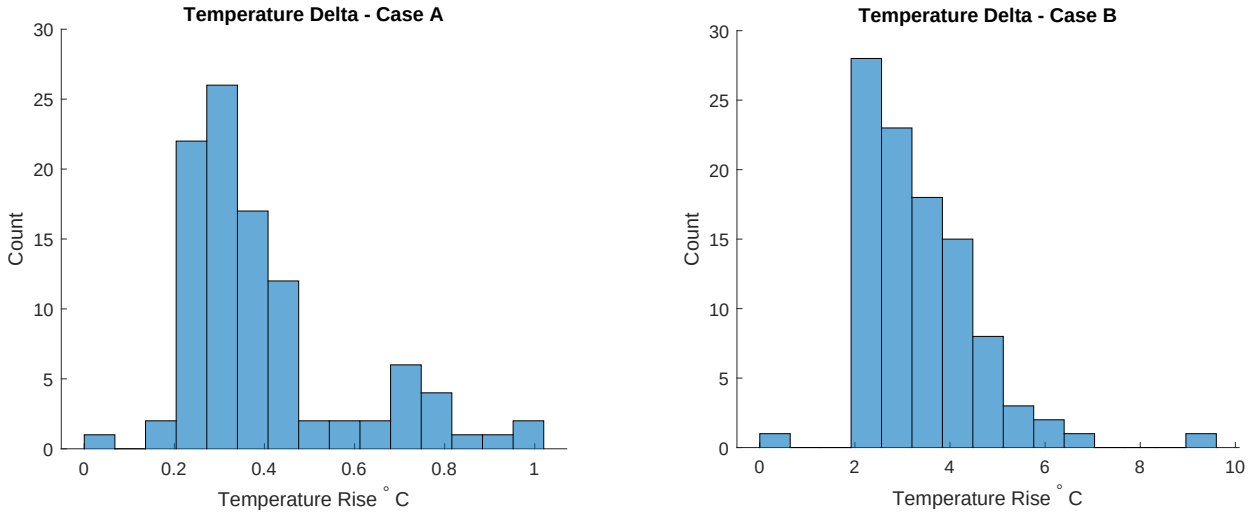


(a) Temperature Distribution Profile A

(b) Temperature Distribution Profile B

Figure 3.3: Distribution of Temperature Rise for Profile A and Profile B

As shown in Figure 3.3a a notional rise in temperature is experienced across all data points in the lightly loaded condition. A similar distribution is provided in Figure 3.3b for

the temperature rise in profile B. Figure 3.3 illustrates the correlated distribution between the rise in temperature for different profiles under the same condition of system health.

The 100 run profiles of combined temperature data for case A and case B will serve as the second set of input data for the prediction of temperature rise in the subsequent Section 3.2.2

## 3.2 Application of Machine Learning

Utilizing the two input datasets defined in the previous section, a set of KNN classifiers were applied to predict leak status and utilizing temperature data as an input into a LSTM model, the temperature delta at max loading was predicted from the step temperature data.

### 3.2.1 KNN classifier for Leak Detection

To detect a system, a cubic and cosine KNN classifier were selected for evaluation. These classifiers were selected due to the unknown, complex, and interdependent relationship between pump current and leak status in the presence of clogging. For classifiers the 100 instances were broken down into two sets, a test dataset, and a train dataset. The training dataset consisted of 80 randomly selected runs from the set of 100 and the remaining 20 were held back for a testing dataset. The training parameters selected are listed below in the following Table 3.2.

Table 3.2: KNN Classifier - Training Parameters

| **Parameter** | **KNN Cubic** | **KNN - Cosine** |
|---|---|---|
| Distance Metric | Minkowski (Cubic) | Cosine |
| Distance Weight | Equal | Equal |
| Number of Neighbors | 10 | 10 |
| Standardize data | True | True |

### 3.2.2 LSTM RNN for Temperature Prediction

To predict the maximum temperature rise given the response to a step in known loading from 10 % to 20 % an LSTM was applied. The LSTM model utilized the 100 temperature profiles as inputs, shown in Figure 3.4, where 10 of the cases were

randomly selected and reserved for a testing dataset and the remaining 90 profiles were utilized as the training dataset.

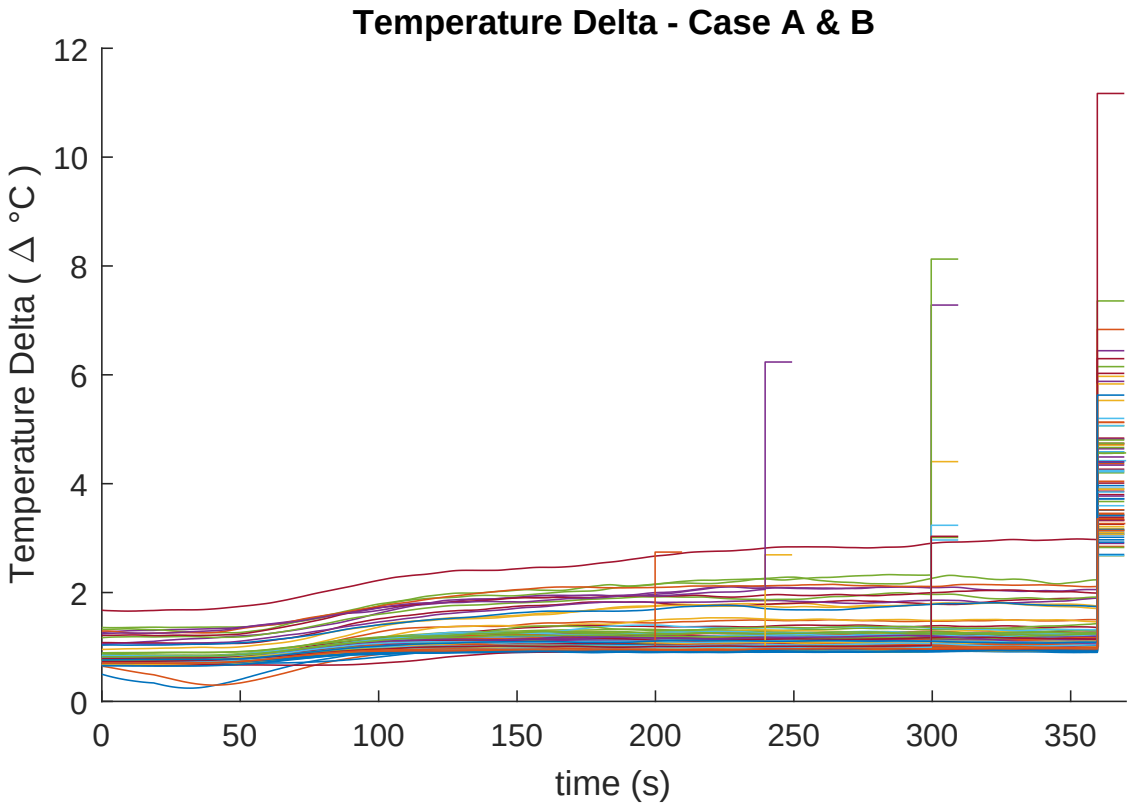


Figure 3.4: Training and Testing Dataset - LSTM

As illustrated in Figure 3.4, left sequence padding was applied to the dataset prior to training and testing. Left padding was selected to place a higher prediction weight on the final output value, as we are only interested in the final temperature achieved and not the ability to model the details of the step in temperature. The Adam optimizer was selected for training the LSTM due to its' favorable ability to handle nonstationary objects with noisy and sparse gradient spaces [47]. Commonly, input data is normalized to avoid gradient clipping, leading to the LSTM prediction value jumping to the highest or end value, however in this application this behavior is favorable as we are only interested in the final temperature value prediction, so the data was not normalized. To train the network the full input profile was used for the 80 cases. Once trained, the model was evaluated on the test data. To test the model, only the first 175 seconds of data was fed as the input and the next single timestep value was predicted. Since the model parameters were tuned to place prediction weight on the final steady state

temperature the predicted value was expected to be near the actual final temperature. To evaluate accuracy the predicted value was compared to the average steady state temperature for the 100 percent loading case. The parameters used are summarized in Table 3.3 and MATLAB was leveraged to implement the testing and training process [48].

Table 3.3: LSTM Parameters

| **Parameter** | **Value** |
|---|---|
| Max Epochs | 200 |
| Shuffle Data | Every Epoch |
| Training option | Adam |
| Sequence Padding | Left |
| LSTM layers | 128 |
| Prediction input data | 500 steps or t = 175 (S) |
| Prediction length | 1 step |

## 3.3 Results and Discussion

For the detection of system leaks given an unknown state of system health, caused by clogging and leaking, a Cosine and Cubic KNN classifiers were leveraged, and their accuracy was compared. The Cubic KNN classifier has an overall test prediction accuracy of 90 %. The Cosine KNN classifier had an overall accuracy of 95 %, proving to be 5 % more accurate than the Cubic KNN classifier. The confusion matrix for the Cosine KNN classifier is shown in Figure 3.5.

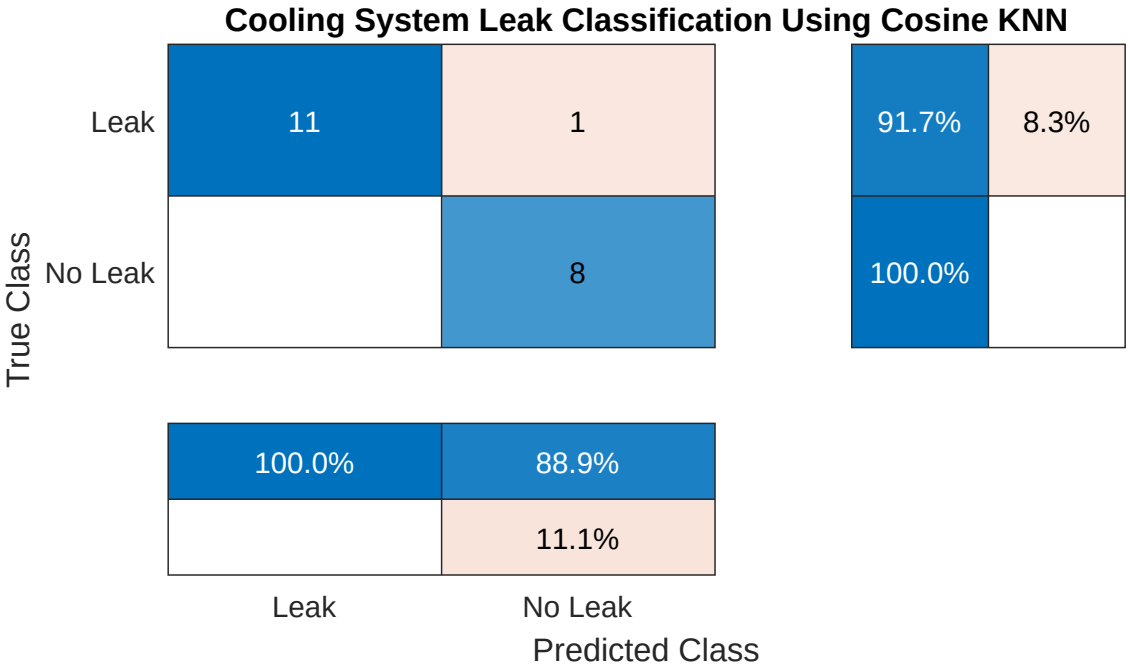


Figure 3.5: Cosine KNN - Confusion Matrix

As depicted in Figure 3.5, given the cases when a leak was present the classifier missed 1 true instance resulting in an 8.3 % error. In the cases where a leak was not present for the true class, the classifier predicted no leak 100 % of the time. Across the training data, the cosine KNN classifier predicted the true system state 95 % of the time, given only pump current as an input to the model. This high prediction accuracy using a simple Cosine KNN model provides promise for the flexibility, ease of implementation and high accuracy of fault detection for machinery systems using AI driven prognostics.

The LTSM model predicted the final temperature rise with an overall error of only 0.8729 % given the dynamic change in load from a heater loading of 10 % to 20 % when tested on the test data. The input LSTM data (Input), actual profile data (Response), LSTM prediction (predicted value), and the average true value used for comparison (Actual Value) for each of the 10 test cases are shown in Figure 3.6.

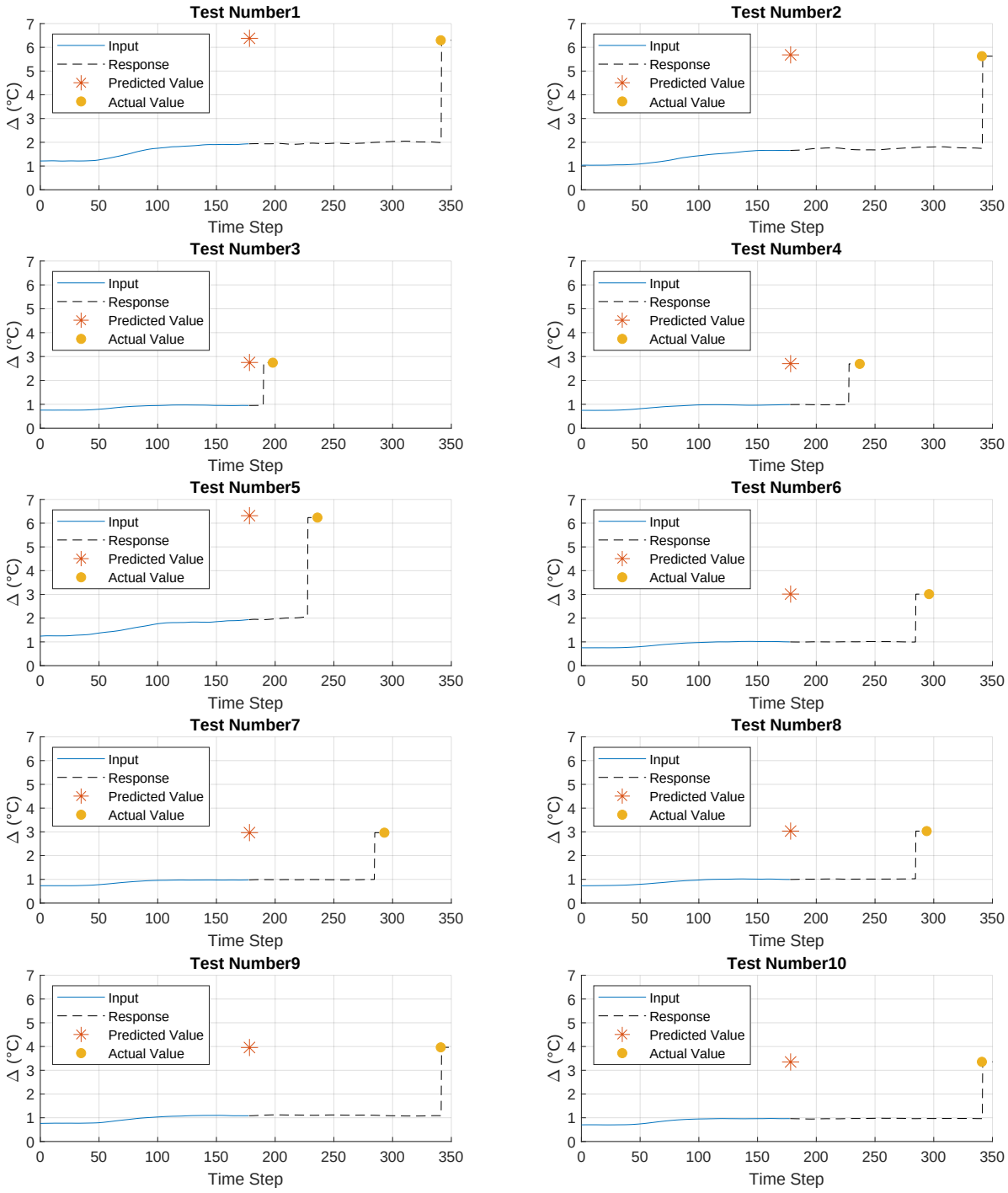


Figure 3.6: LSTM Test Predictions

The model was effective in the prediction of final temperature, however the model was unable to provide an accurate time for the final temperature. The first prediction value for the model provided the final temperature value. The model output was truncated after the first predicted value as shown as a singular point (predicted value) in red in Figure 3.6. The

final value used as the true point of comparison is illustrated in yellow. The yellow point is compared against the predicted point to quantify the model error. The numerical values for the prediction results shown visually in Figure 3.6 are provided below in Table 3.4.

Table 3.4: LSTM Prediction Test Results

| **Test Case** | **Predicted Value** | **True Value** | **Error(%)** |
|---|---|---|---|
| 1 | 6.30 | 6.45 | 2.51 |
| 2 | 5.63 | 5.73 | 1.91 |
| 3 | 2.74 | 2.76 | 0.61 |
| 4 | 2.69 | 2.71 | 0.74 |
| 5 | 6.24 | 6.39 | 2.48 |
| 6 | 3.01 | 3.01 | 0.04 |
| 7 | 2.97 | 2.97 | 0.09 |
| 8 | 3.03 | 3.03 | 0.02 |
| 9 | 3.96 | 3.96 | 0.17 |
| 10 | 3.36 | 3.35 | 0.16 |

As illustrated in Table 3.4 and Figure 3.6 for the 10 test cases the final temperature rise was predicted with an overall error of only 0.8729 %.

## 3.4 Summary

Work from [45] demonstrated the ability to detect a common cooling system fault (i.e., a leak) in the presence of an unknown system state of health caused by clogging. In addition this work demonstrated the ability to leverage the response of the cooling system to a known change in loading, to predict the temperature rise at full load, providing knowledge of the systems capacity given a degraded state of system health. The ability to both detect faults and predict the current system capacity using simple AI driven algorithms provides insight into the potential ability of AI driven algorithms to provide better prognostic system health predictions at the plant level. Work in Chapters 4-5 expands off this work by applying AI driven algorithms across the plant machinery systems to predict overall mission capabilities in time given the degrading state of health of the plant.

# CHAPTER 4

# Acquisition of Laboratory Ship Machinery Plant Run to Failure Data

## 4.1 Introduction and Overview of Experiments

The MLSMP, defined in Chapter 2, was leveraged to create 100 run to failure (RTF) profiles that modeled a notional ship machinery plant. The failure profiles injected common faults into the cooling and fuel systems, which caused a degradation in system performance until both the cooling and fuel system failed. Data was collected over a period of 10 sequence-points or until both the fuel and cooling systems had failed. Each sequence-point represented a discrete state of health for the plant machinery systems. On each sequence-point, steady state data was recorded for three different operational profiles. The 100 failure profiles were configured using a constructed software model of the fuel and cooling system in conjunction with a clog model from literature [3]. The model and resultant control outputs is discussed in the following section, section 4.2. The three operating profiles for each discrete sequence-point are defined in section 4.3. Using the configured failure profiles and operational profiles a test procedure was built to record the 100 run to failure profiles, which is defined in Section 4.4. Section 4.5, defined the acquired data, and pre-processing conducted to remove sensor signal noise, errors in hardware system data acquisition, and data trimming to fit the required run to failure format for AI implementation. The final section, Section 4.6, provides a summary and key takeaways for the acquisition of laboratory ship machinery plant run to failure profiles. A summary of terms is provided below in Table 4.1.

Table 4.1: Key Terms

| |
|---|
| **Operational Profile:** A set of operational loads that represents a steady load on the plant (i.e mission load, propulsion load, etc.). This work leverages three operational profiles (a-c) defined in detail in Section 4.3 |
| **Mission scenario:** A sequence of the three operational profiles that that represent a notional ship mission. |
| **Sequence-Point:** A discrete state of health for the machinery plant with support systems having a discrete level of clog restriction and a state of leak or no leak. For each point the mission scenario is conducted. Three 10 second steady state windows of data is recorded for each point. One of the three windows is within each of the three operational profiles (a-c). |
| **Run to failure (RTF) profile:** A sequence of up to 10 points where each successive point contains a further degraded in state of plant health while one or more operational profile can be achieved. |
| **Failure:** The instance where any support system can no longer provide sufficient functionality to achieve a given operational profile. |
| **Mission Profile:** The mission profile is completed for each discrete point of health within the sequence. |

## 4.2 Software Modeling

### 4.2.1 Overview

To accurately simulate in hardware the dynamics of clogs and leaks onboard ocean going vessels, software models of the hardware fuel and cooling systems within the MLSMP were developed in MatLAB Simulink. The software models integrated an adopted clog model developed by [3] into the constructed cooling and fuel system models. The functional diagram for each of the base configurations leveraged in the cooling and fuel system models is shown below in Figure 4.1.

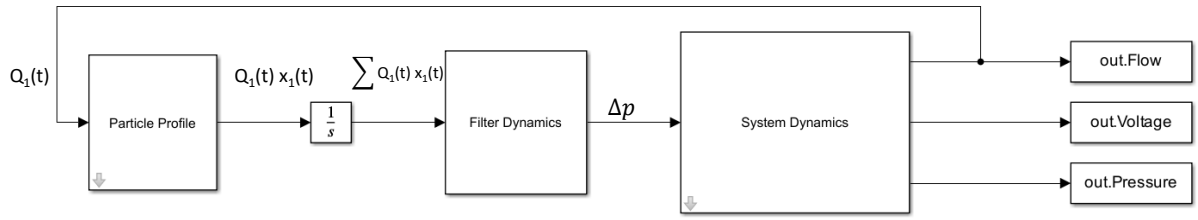


Figure 4.1: Software Model Overview

The functional diagram shown above in Figure 4.1 was leveraged as a single instance for the cooling system, given the singular and identical flow paths for systems 1 and 2. The fuel system contains two flow paths; a low pressure and high pressure flow path requiring two individual instances of the base model to represent the high pressure and low pressure fuel systems, respectively.

The variable $Q_1$ represents flow as a function of hardware system model dynamics and filter clogging dynamics. The variable $x_1$ represents the particle content which varies with respect to time. The particle buildup is a summation of flow rate times the particle content or $\sum Q_1 x_1$. The drop in pressure due to filter dynamics is represented by $\Delta p$. The base configuration shown in Figure 4.1 for the three variant models leverage identical governing equations for each of the three models. Parameters within the model vary with respect to each of the three flow paths. A detailed discussion of the clog model is provided in the following subsection. Leveraging the clog model, the constructed Simulink models for the fuel and cooling systems are defined in Subsection 4.2.3.

### 4.2.2 Clog Model

To accurately model filter clogging for the cooling and fuel system a filter clog model developed by [3] was leveraged. The clog model and adaptations made for use in this thesis is defined in this subsection. The original model provides the drop in pressure across a filter based on constant flow, a fixed particle size distribution, and a fixed percent of particles suspended in flow. The representative filter and cake buildup for the model is shown below in Figure 4.2.

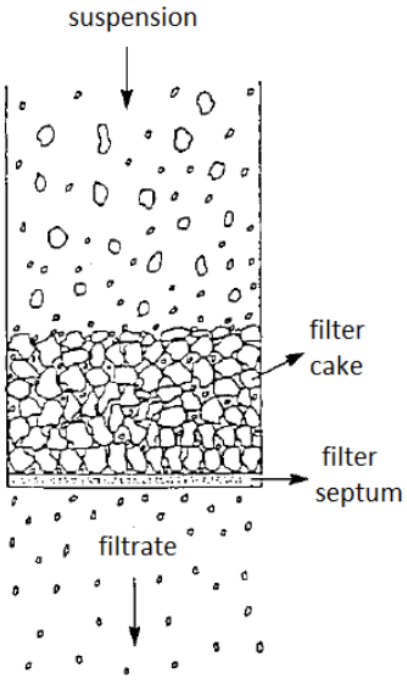


Figure 4.2: Schematic representing cake build up on a filter medium from [3].

As shown above in Figure 4.2, the particles suspended in flow build up as filter cake and compact against the filter septum. The buildup of filter cake as a result of the particles in suspension produces a drop in pressure across the filter. The model from literature solves for pressure drop across the filter using Equation 4.1 with parameters defined in Table 4.2.

$$\Delta P = \frac{150 V_s \mu (1-e)^2 L}{{D_p}^2 \epsilon^3} + \frac{1.75(1-\epsilon)\rho {V_s}^2 L}{\epsilon^3 D_p} \tag{4.1}$$

Table 4.2: Clog Simulation Variables

| **Variable** | **Parameter** |
|---|---|
| $\Delta P$ | Pressure drop |
| $L$ | Total height of the bed (or cake) |
| $V_s$ | Superficial (empty-tower) velocity |
| $\mu$ | Viscosity of the fluid |
| $\epsilon$ | Porosity of the bed (or cake) |
| $D_p$ | Diameter of the spherical particle |
| $\rho$ | Density of liquid |

To solve for the total height of the bed $L$ the following equation is used.

$$L = \frac{\ln\left(l_1 \frac{\sum Q_x}{A_f}\right)}{l_2} \tag{4.2}$$

Where $\sum Q_x$ represents the cumulative particle volume retained on the filter with $Q_x$ representing a constant produce of flow rate and particles in suspension. The variable $A_f$ represents the filtration area. Parameters $l_1$ and $l_2$ are optimized through experimental fitting conduced in literature [3]. To solve for the $\epsilon$, the following equation is used.

$$\epsilon = 1 - \frac{e^{p_1 \frac{\sum Q_x}{V_f}}}{p_2} \tag{4.3}$$

The optimized parameter values for Equations 4.2 and 4.3 are defined below in Table 4.3.

Table 4.3: Optimized Parameters From Literature

| **Parameter** | **Value** |
|---|---|
| $l_1$ | 4e+7 |
| $l_2$ | 899 |
| $p_1$ | 1.2346 |
| $p_2$ | 9.1464 |

This base model provided by [3] in equations 4.1 - 4.3, was modified to incorporate a variable input of flow rate and particle density in time to align with the dynamics of the physical hardware systems and particle distributions in fuel and cooling fluids onboard ships. To do so $\sum Q_x$ was replaced with a time variant variables $Q_1(t)$ and $x_1(t)$ to produce $\sum Q_1(t) * x_1(t)$ where, $Q_1(t)$ the time variant value for flow across the filter given the hardware system model dynamics. $x_1(t)$ represents the time variant profile for particle density representative of fuel and cooling system particle profiles, defined further in the following subsection.

### 4.2.3 Software Simulation Models

The adopted clog model defined in the previous subsection, was integrated with software models of the hardware fuel and cooling systems within the MLSMP. For both the fuel and cooling hardware systems, experimental testing was conducted to map flow and pressure as a function of leak status (leak and no leak conditions) and proportional valve percent restriction. This calibration data was acquired by operating each system at steady state for

each discrete position of the proportional valve, commanded in volts DC, with and without a system leak. Using the hardware data, functions were created for each flow path to calculate flow and proportional valve set point ($V_{DC}$) as a function of $\Delta p$ across the emulated filter (proportional valve) as defined in Chapter 2. The constructed software models for each flow path was integrated with the adopted clog model which produced three variants of the base model shown visually in Figure 4.1. The three models were configured into two Simulink files for run time simulations. The two files represent each fluid system, cooling and fuel. The cooling file is used for cooling system 1 and 2. Experimental data for cooling systems 1 and 2 produced near identical flow to pressure curves, with a varied commanded voltage to pressure curve between systems 1 and 2. Given the software simulations are only dependent on flow and pressure, and the output of command voltage is provided for future hardware system control, a single Simulink simulation file was sufficient to model both flow paths for the cooling system and incorporate two output command voltage signals for each of the two cooling systems. All hardware system dynamics for the fuel systems 1 and 2 with respect to varied proportional valve restriction and leaks were identical. As a result fuel system 1 and 2 (combines the LP and HP models) are contained in a singular Simulink simulation file. A visual of the fuel and cooling system files are shown below in Figure 4.4 and Figure 4.3.

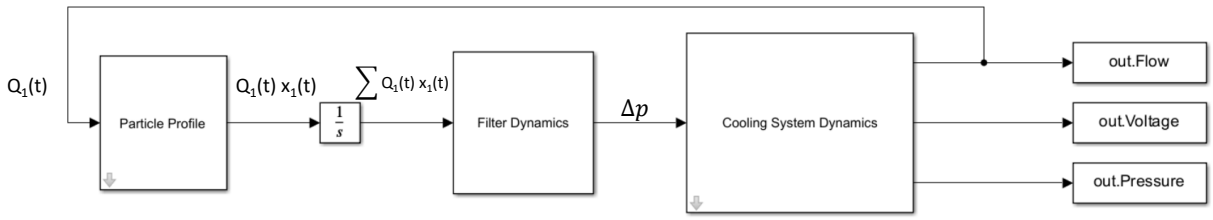


Figure 4.3: Cooling System Simulink Model

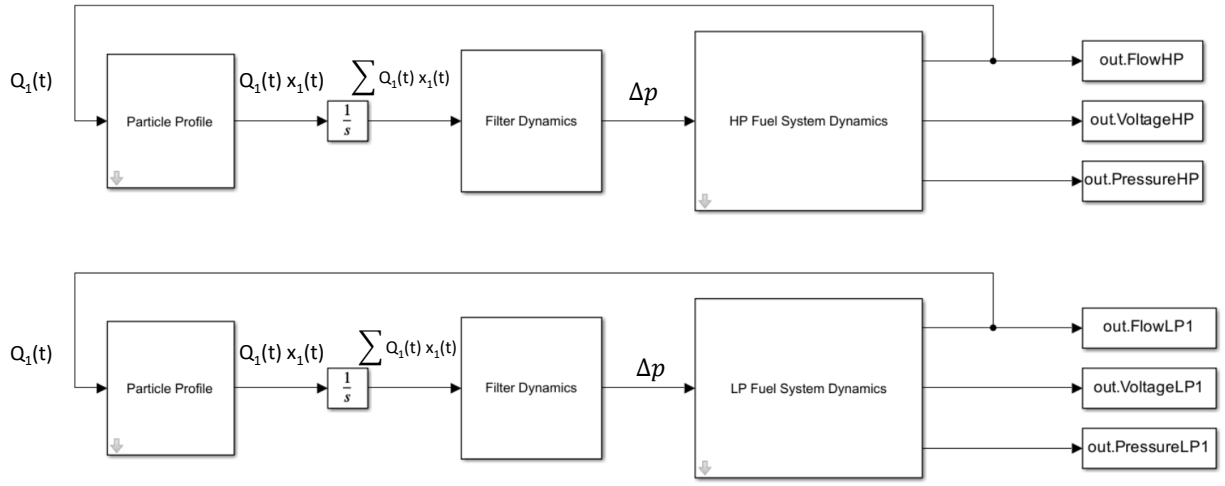


Figure 4.4: Fuel System Simulink Model

The filter dynamics block leveraged the modified Equations 4.1- 4.3 and received input of $\sum Q_1(t) * x_1(t)$ and output of $\Delta p$ into each of the hardware system model blocks which provided an output of control voltage for the proportional valve, flow $Q_1(t)$ and the converted value for system pressure given the system dynamics and drop in pressure across the modeled filter. The output of $Q_1(t)$ was used as feedback into the particle profile. The particle profile produced a time variant value for $x_1(t)$ multiplied by flow.

### 4.2.4 Base Failure Profiles

Using the software simulation models, defined in the past subsection a base run to failure simulation was constructed for both the fuel and cooling systems independently of each other. The Simulink simulation length was set a a maximum duration of 10 sequence-points or until a defined failure limit for the given system (fuel or cooling) met. The cooling system failure limit was set at a flow of less than 15 percent of the nominal valve, or 1 liter per minute. The cooling system limit was determined by the minimum flow rate required to dissipate the no load system waste heat rejection without overheating. The fuel system failure limit was defined as a function of pressure for the low and high pressure systems where the fuel system would fail if the pressure of the low pressure path dropped below 5 PSI or the pressure of the high pressure path dropped below 80 PSI. The fuel system limits were determined by the necessary system pressures to produce the necessary fuel flow out of the injector system for the no load plant operation point. A summary of the system limits is provided below in Table 4.4.

Table 4.4: Fuel and Cooling System Limits

| **System** | **Value** | **Unit** |
|---|---|---|
| Fuel LP | 5 | PSI |
| Fuel HP | 80 | PSI |
| Cooling | 1 | LPM |

To configure the base run to failure simulation for the fuel and cooling systems, a mean particle content with zero variance was determined through a convergence simulation for both systems without any leak injection. The finalized mean value for the fuel and cooling particle content produced a an emulated clog which met individual system limits on sequence-point 9. This base failure configuration is shown below Figure 4.5 for the cooling system and Figure 4.6 for the fuel system.

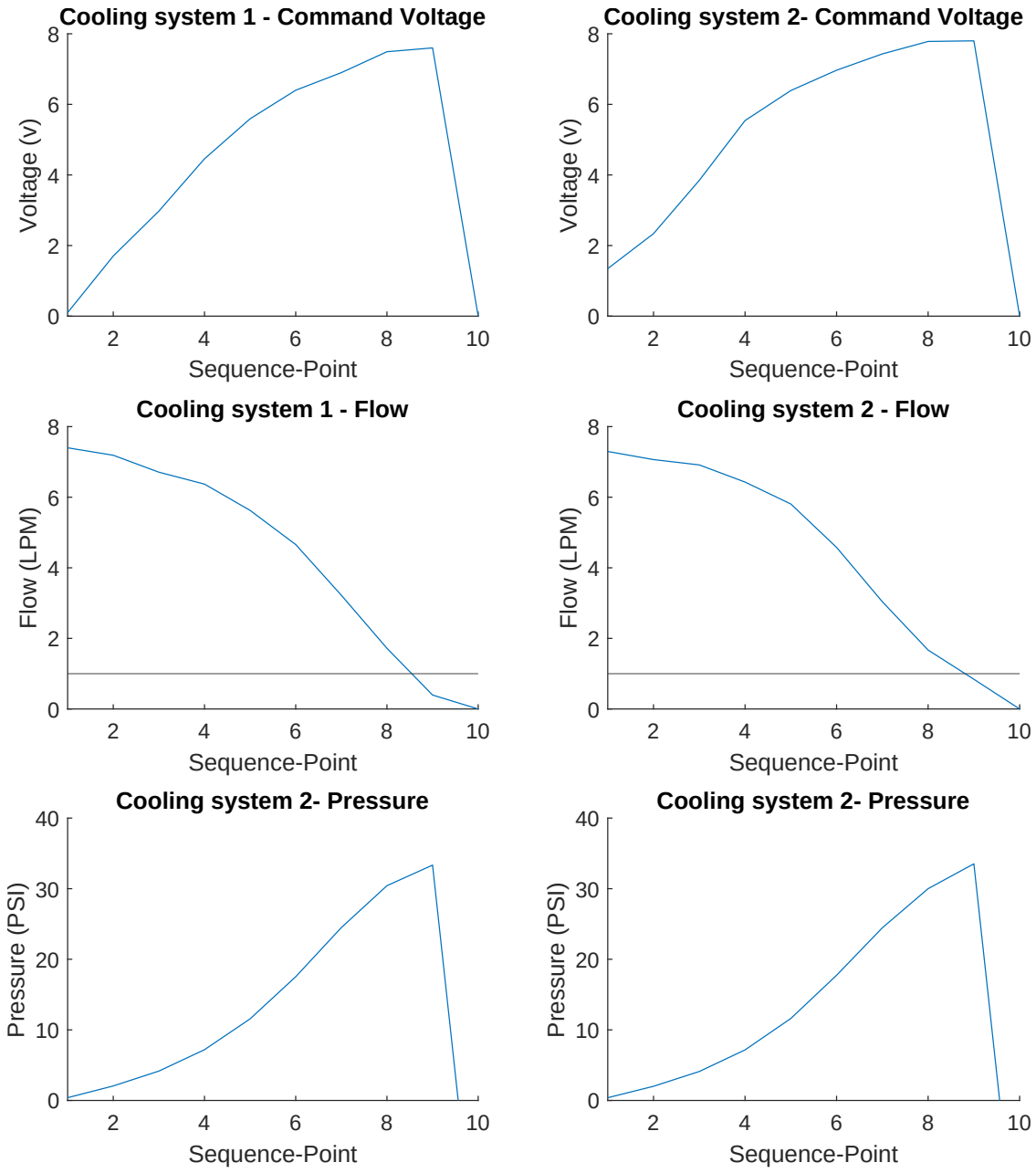


Figure 4.5: Software Simulation of Base Cooling System Failure Profile

As shown above in Figure 4.5, cooling systems 1 and 2 use the same simulation model, however constructed control output for the two proportional valves vary, this variation is a result of two different proportional valves used for clog emulation in system 1 as was used in system 2. The varied curves are produced through two lookup tables for command voltage based on system pressure.

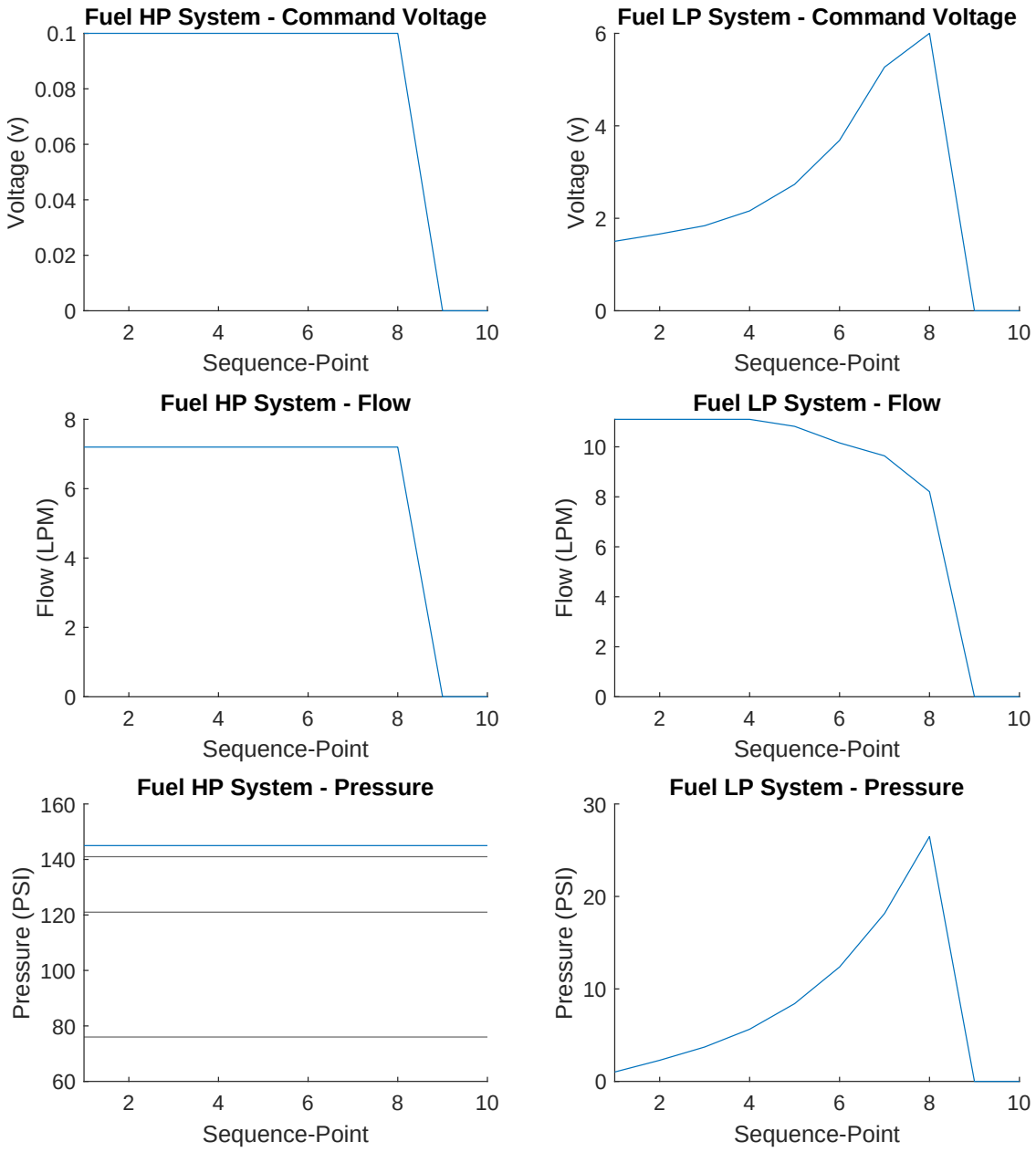


Figure 4.6: Software Simulation of Base Fuel System Failure Profile

Figure 4.6, depicts the base failure profile for both fuel systems. The differences between fuel system 1 and 2 were insignificant allowing both fuel systems to receive the same command voltage for the proportional vales within both fuel systems. The fuel system fails on sequence-point 9 due to restrictions in the LP fuel system. The LP fuel system is the primary source of failures for the fuel systems in the real world, where high pressure fuel system failures are far less common [49].

The base failure profiles shown in Figure 4.5, and Figure 4.6 were used to define the mean

values for particle size in time. To construct the 100 run to failure profiles a randomized distribution was applied to each clog models particle content. The construction of the 100 run to failure profiles is defined further in the following subsection.

### 4.2.5 Software Batch Simulations for Failure Profiles

Using the two constructed Simulink files and base failure profiles, a code was constructed to produce 100 failure profiles for the fuel and cooling systems. The code produced 100 CSV control files compatible with the LabVIEW csv. control mode defined in Section 2.8. The 100 failure profiles leveraged the base run to failure profile defined in Subsection 4.2.3 and integrated a distribution of particle content for each of the three filter models within the three modeled flow paths (cooling system, fuel system low pressure and fuel system high pressure). In addition to the injection of clogs, for each run to failure profile there was a 10 percent chance of a leak being injected for a given failure profile within the first 1-4 sequence-points for all flow paths (cooling system, fuel system low pressure and fuel system high pressure). Particle profile distribution was implemented using Equation 4.4 with variables defined in Table 4.5 for each of three clog models.

$$x_1 = x_a + IF(t_{sim} > t_{step} \ \& \ r_{clogstep} > p_{clogstep}, x_b) \tag{4.4}$$

Where $x_a$ and $x_b$ are both time variant particle profiles with a Gaussian distribution. $x_a$ represents the base continuous particle profile and $x_b$ represents a potential step in particle density triggered if $t_{sim}$ is greater than $t_{step}$ and $r_{clogstep}$ is greater than $p_{clogstep}$. Where $t_{step}$ is a random value between 0 and 4 sequence-points, $r_{clogstep}$ is a random number generated between 0 and 1 and $p_{clogstep}$ is one minus the desired probability for step increase in particle density. The mean value ($\mu$) and distribution ($\sigma$) are defined for each of the clog models below in the following Table 4.2.

Table 4.5: Failure Simulation Parameters - Mean and Variance

| **Variable** | **Value -** $x_a$ | **Value -** $x_b$ |
|---|---|---|
| $\sigma_{cooling}$ | 2 | 1 |
| $\sigma_{Fuel-LP}$ | 2 | 1 |
| $\sigma_{Fuel-HP}$ | 2 | 0 |
| $\mu_{Cooling}$ | $0.058 * (1 \pm P_1)$ | 0.04 |
| $\mu_{Fuel-LP}$ | $0.03 * (1 \pm P_2)$ | 0.02 |
| $\mu_{Fuel-HP}$ | $0.04 * (1 \pm P_3)$ | 0 |
| $p_{clogstep-cooling}$ | - | 0.3 |
| $p_{clogstep-FuelLP}$ | - | 0.2 |
| $p_{clogstep-FuelHP}$ | - | 0.0 |

The Gaussian distribution seed time was set to update four times an hour over the software simulation run. The variables $R_1 - R_3$ represent a randomized value generated prior to each simulation to modify the mean particle content from the base value. The randomized values are listed below in Table 4.6.

Table 4.6: Failure Simulation Parameters - Randomization

| **Parameter** | **Range** |
|---|---|
| $R_1$ | $\pm.30\%$ |
| $R_2$ | $\pm.40\%$ |
| $R_3$ | $\pm.60\%$ |

For each simulation run, a 10% chance of leak leak injection exists for each of the three flow paths (cooling, fuel LP, fuel HP). The status for each system (leak or no Leak) and each failure profile is random with a 10 % probability of occurrence per system per failure profile. If a leak exists for a given failure profile a random sequence-point is selected to inject the leak between 2-4.

Using the random injection of leaks and distribution of particles causing clogs for the fuel and cooling system 100 failure profiles were constructed. A visual of the distributed profiles for the cooling and fuel systems are shown below in Figure 4.7 and Figure 4.8.

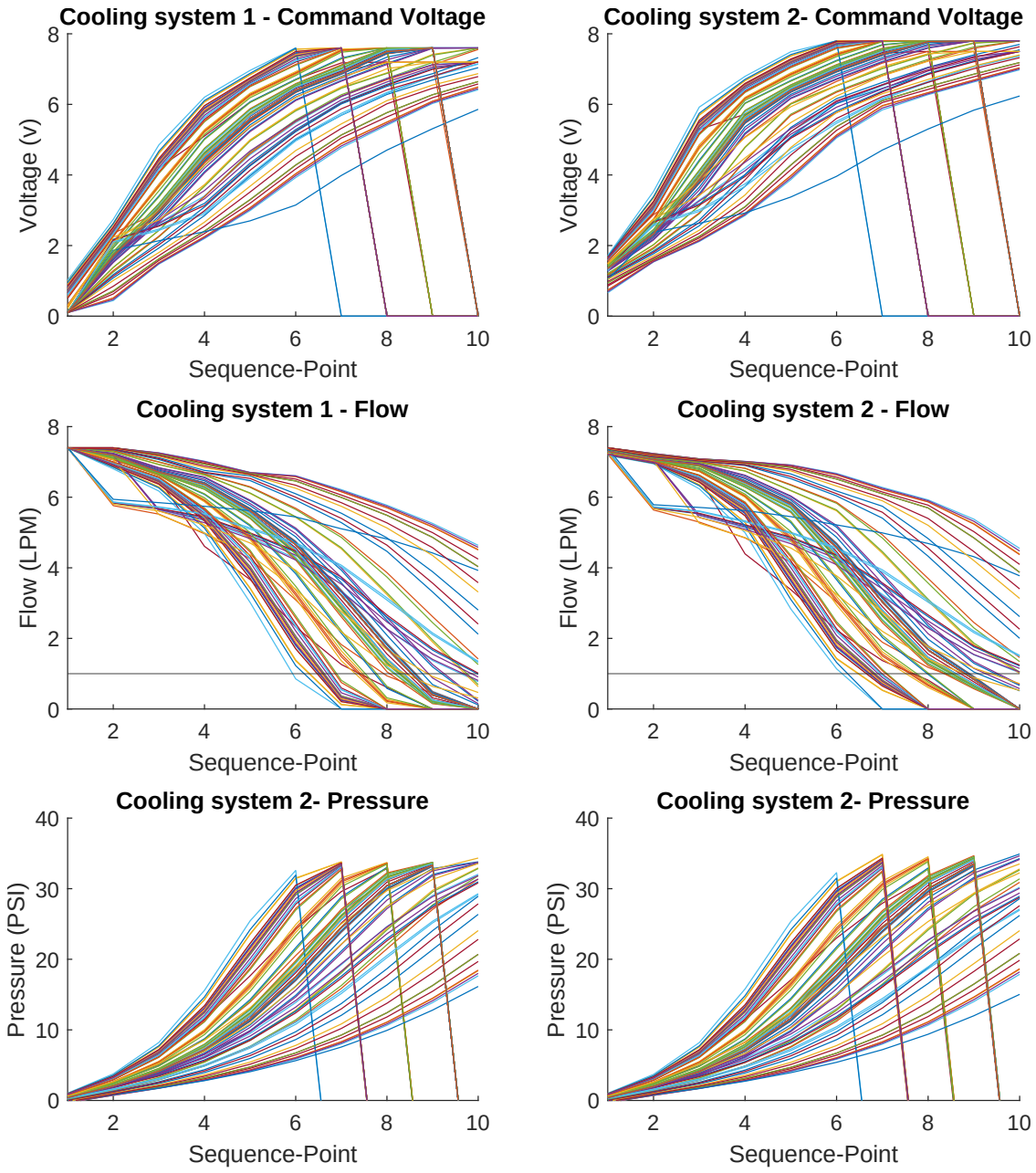


Figure 4.7: Run to Failure Profiles - All - Cooling

As shown above in Figure 4.7 the cooling failure has a mean failure sequence-point of 9 with a minimum failure sequence-point of 6 and a maximum exceeding the 10 sequence-point simulation limit. The sharp changes in flow are indicative of leaks injected into the systems. The drop from max voltage of about 8vDC command to the proportion valve to 0 vDC represents the system returning to full health from failure and corresponds to the drop in pressure shifting from its' maximum value to zero. This is a result of the cooling system being returned to full health (no restrictions or leaks) after failure while the fuel system

continues to run to failure for the given profile. This process is conducted to record both system run to failure profiles and avoid holding the failed system at an operational point that places additional strain on the physical hardware within the system.

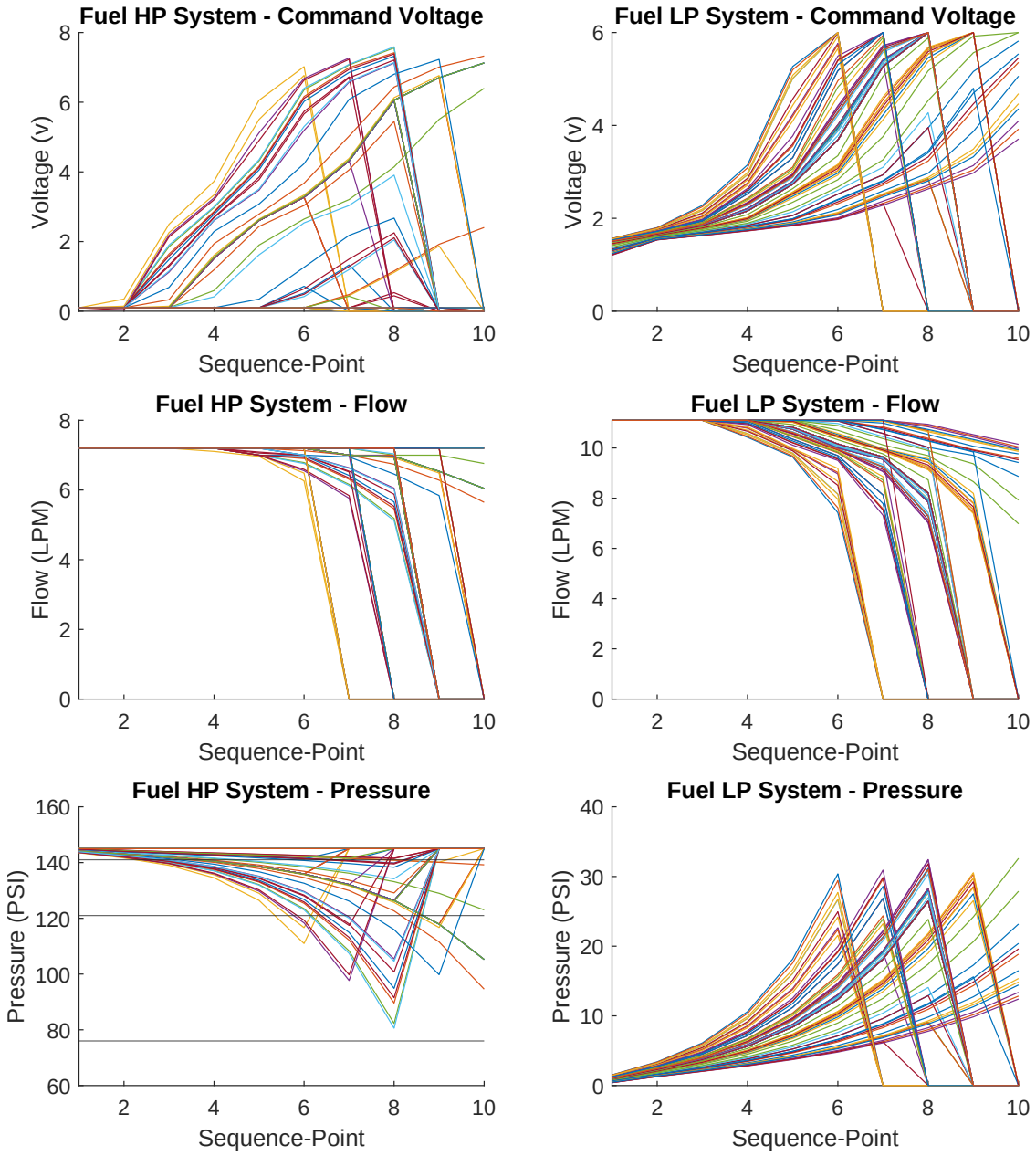


Figure 4.8: Run to Failure Profiles - All - Fuel

As shown above in Figure 4.8 the fuel system also has a mean failure of 9 sequence-points with a minimum failure sequence-point of 6 and a maximum exceeding the 10 sequence-point simulation limit.

Using the 100 constructed run to failure profiles shown visually above in Figure 4.7 and

Figure 4.8 on each sequence-point, discrete state of system health, data for operation of three unique operational profiles was recorded. The three operational profiles are defined in the following subsection.

## 4.3 Design of Operational Profiles

Over the up to 10 sequence-point run to failure profile or until both the fuel and cooling systems reached their failure limit, three operational profiles were simulated in hardware at steady state and data was recorded for a period of 10 seconds. The three operational profiles are defined below in Table 4.7.

Table 4.7: Simulated Ship Operational Profiles

| **Operation Profile** | **Mission Load** | **Propulsion Rate** | **MCR** | **Waste Energy** |
|---|---|---|---|---|
| A | 0% | 20 Hz | 47% | 42% |
| B | 100% | 30 Hz | 97% | 100% |
| C | 0% | 60 Hz | 82% | 67% |

As shown above in Table 4.7 the three operational profiles (A-C) placed varied demands on the cooling and fuel system through differing propulsion and mission system loads. Operational profile B, operated the mission system at 100 percent of its' capacity and the propulsion system in a low speed, low load condition. Operational profile B had the maximum waste heat rejection due to the highly inefficient electrical mission system loads placing the emulated waste heat at 100 percent capacity with the generator system at 97 percent of its' mean continuous power rating (MCR). Operational profile C, placed the propulsion system at full speed ahead (60 Hz) without any mission loads online. Operational C had a MCR of 82 percent and a waste heat of 62 percent. Operational profile C depicts a 15 percent drop in MCR with a 38 percent drop in waste heat rejection as compared to profile B. The nonlinear reduction in waste heat rejection is a result of the more efficient propulsion system load replacing the highly inefficient mission system load. Operational profile A, provides a low load condition with a propulsion speed of 20 Hz and no mission load online. A summary of the operational system commands for the three operational profiles is provided in Table 4.8.

Table 4.8: Simulated Ship Operational Control Inputs

| Operation Profile | Mission Load | Propulsion Rate | Waste Energy |
|---|---|---|---|
| A | 0A DC | 20 Hz | 42% |
| B | 23A DC | 30 Hz | 100% |
| C | 0A DC | 60 Hz | 67% |

The three operational profiles place a wide variation of demands on the cooling and fuel system. Given a degraded state for the cooling system the cooling system will be unable to provided sufficient flow to reject the waste heat created by profile B followed by profile C and finally unable to support the low load condition, profile A, without overheating. Similarly, given a degrading state for the fuel system, the fuel system may be able to provide sufficient fuel delivery to power profile A but insufficient to meet the demands of profile B and C.

## 4.4 Test Procedure

A test procedure was constructed using the 100 modeled run to failure profiles and three operational profiles constructed in the past two sections of this chapter. The test procedure defined in this subsection, and used to record the hardware run to failure data, was formed to minimize the potential for external effects and noise on the acquisition of hardware data. The procedure is as follows.

- Follow the reference `MEL_userguide_V1_.docx` document and complete the following tasks:
  - Turn the NI control system on.
  - Turn the LabVIEW software system on.
  - Prior to starting the application, define the desired failure profile in the box indicated by the red box shown below in Figure 4.9.

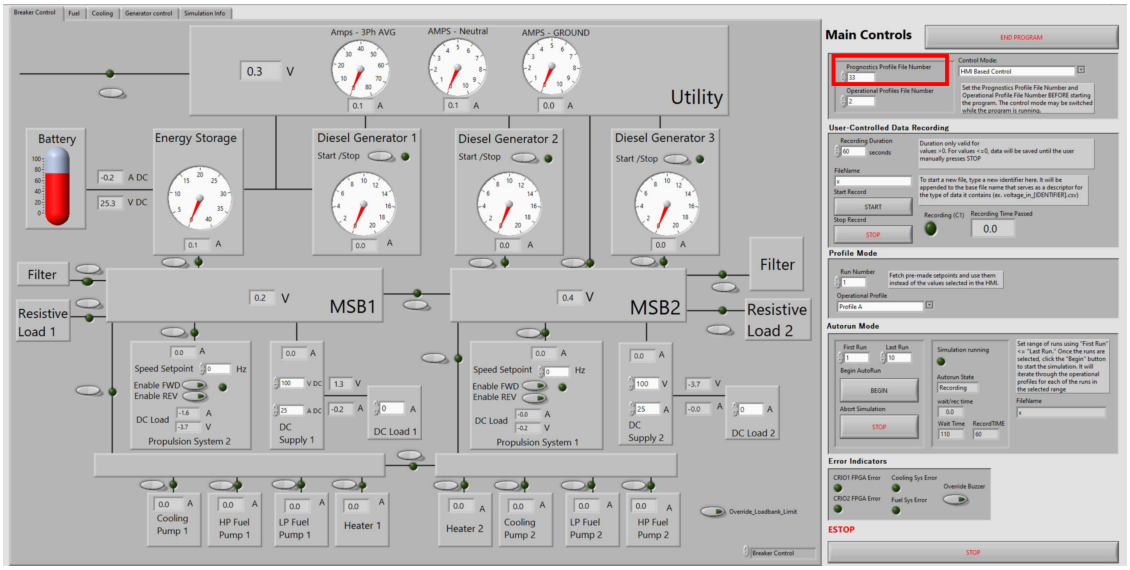


Figure 4.9: Run To Failure Hardware Test Procedure - Profile Selection

  - Start the application
  - Turn the external DC CT sensors on
  - Turn the load banks on and place in Constant Current mode
  - Turn the energy storage system on and place the input as Generator 1
  - Locate the main utility panel and place only the following three breakers online: Main Input, Generator 1, and Generator 3
  - Turn on the 480V AC power supply

- Configure the electrical grid as shown below in Figure 4.10, using the numbering convention shown in the figure as the order to close breakers and start the propulsion systems:

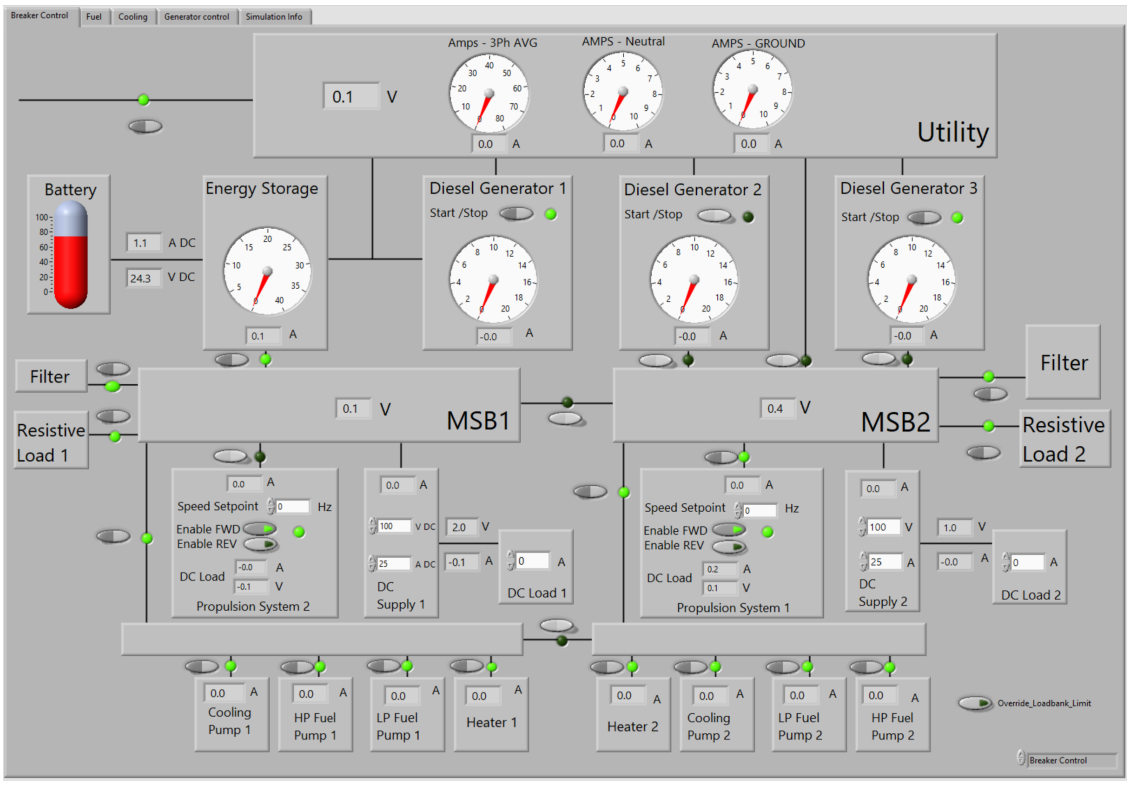


Figure 4.10: Run To Failure Hardware Test Procedure - Breaker Configuration

- Enable The cooling system heaters as shown below Figure 4.11

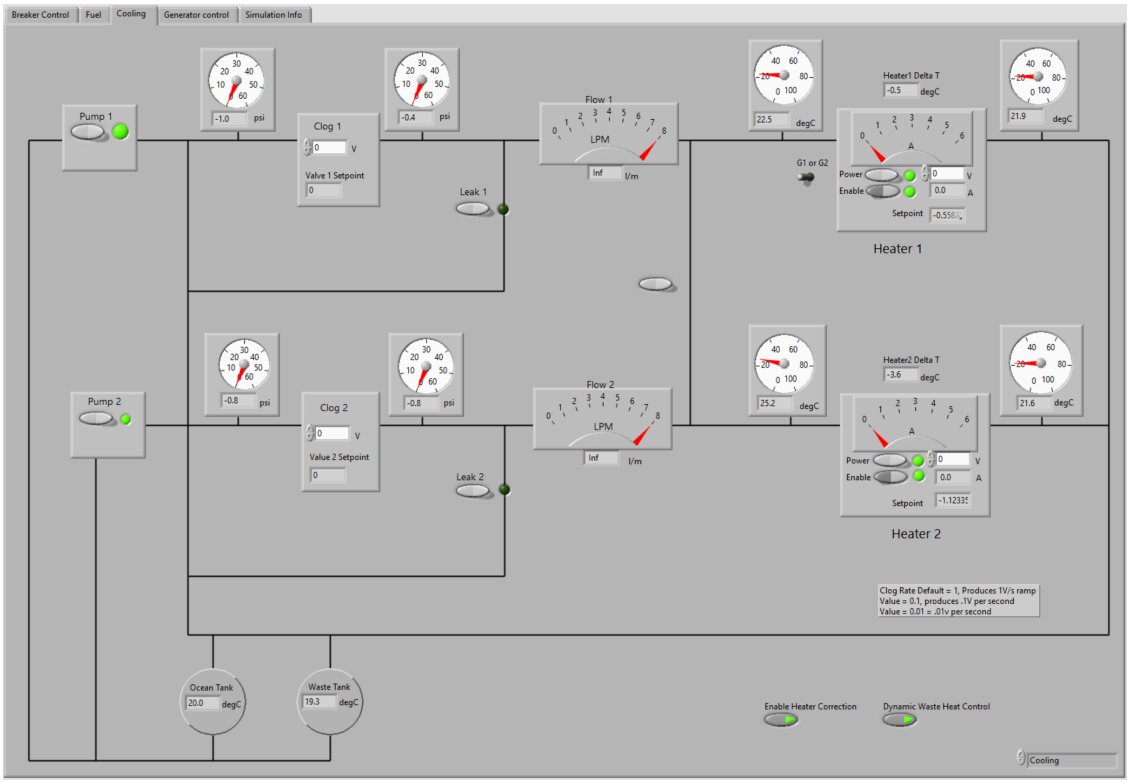


Figure 4.11: Run To Failure Hardware Test Procedure - Cooling Configuration

- Select the Auto-run control mode as shown below

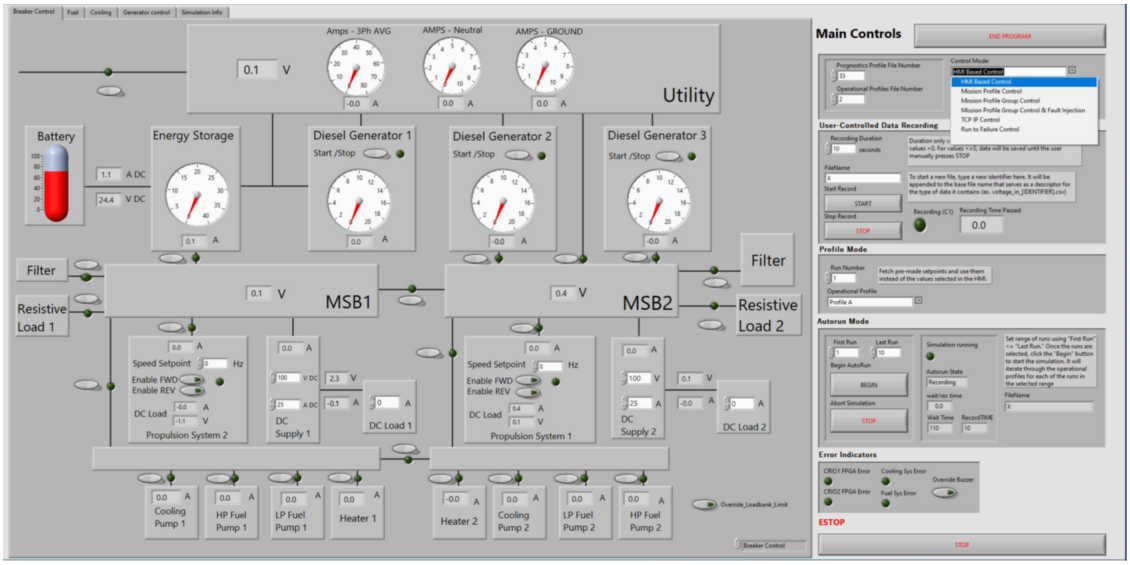


Figure 4.12: Run To Failure Hardware Test Procedure - Run Configuration

- Define the first run as 1 and second run as 10, shown above near the blue arrow.

- Click “Begin” , the automation process is now in process, please standby and ensure the system is operating without any faults present.
- Once the run completes, indicated by the “simulation running” light turning off and system audible alarm is present, place the control mode back to HMI, open all breakers closed and enable switches pressed then click end program
- Transfer the data from each CRIO (1and2) and the Host PC to the corresponding prognostics profile folder, and example is shown below, followed by the necessary file paths.

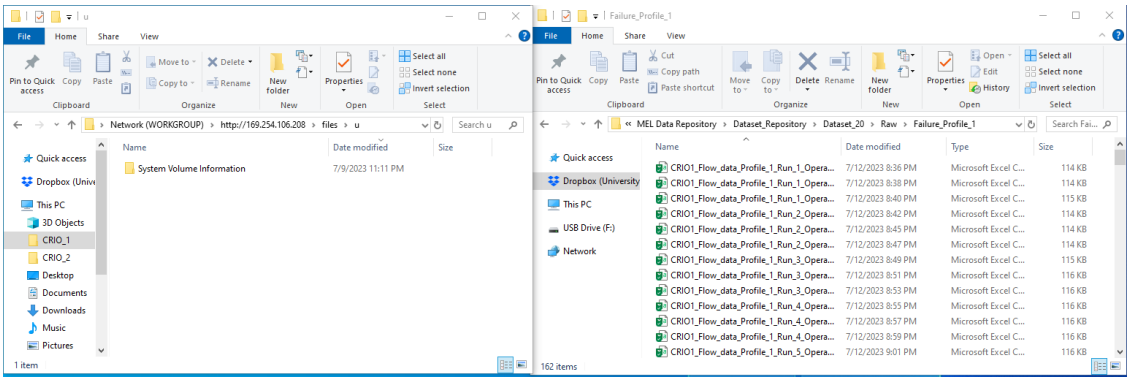

Figure 4.13: Run To Failure Hardware Test Procedure - File Transfer

File Paths:

  - CRIO1: `http://169.254.9.175/files/u`
  - CRIO2: `http://169.254.106.208/files/u`
  - Host PC Data: `C:/Users/Marin/Documents/Output_Variables`
  - Data Repository: `C:/Users/Marin/Dropbox (University of Michigan )/MEL Data Repository/Dataset_Repository/Dataset_15/Raw_Data`

- Once all files are transferred for the given failure profile, delete the original files from CRIO1 CRIO2 and the Host PC.
- Update the failure profile to continue data acquisition or follow the shutdown procedures to complete your data acquisition session.

This process was followed for the 100 run to failure simulations in hardware to ensure consistency across the 100 failure profiles and reduced unwanted patterns and noise in data caused from inconsistencies hardware simulations.

## 4.5 Acquired Laboratory Data

### 4.5.1 Overview

Using the test procedure defined in the previous subsection, 100 run to failure profiles were recorded using the MLSMP. An example of a singular run to failure profile (Profile 20) and the high level system outputs is provided below in Figure 4.14 for the cooling system and Figure 4.15 for the fuel system.

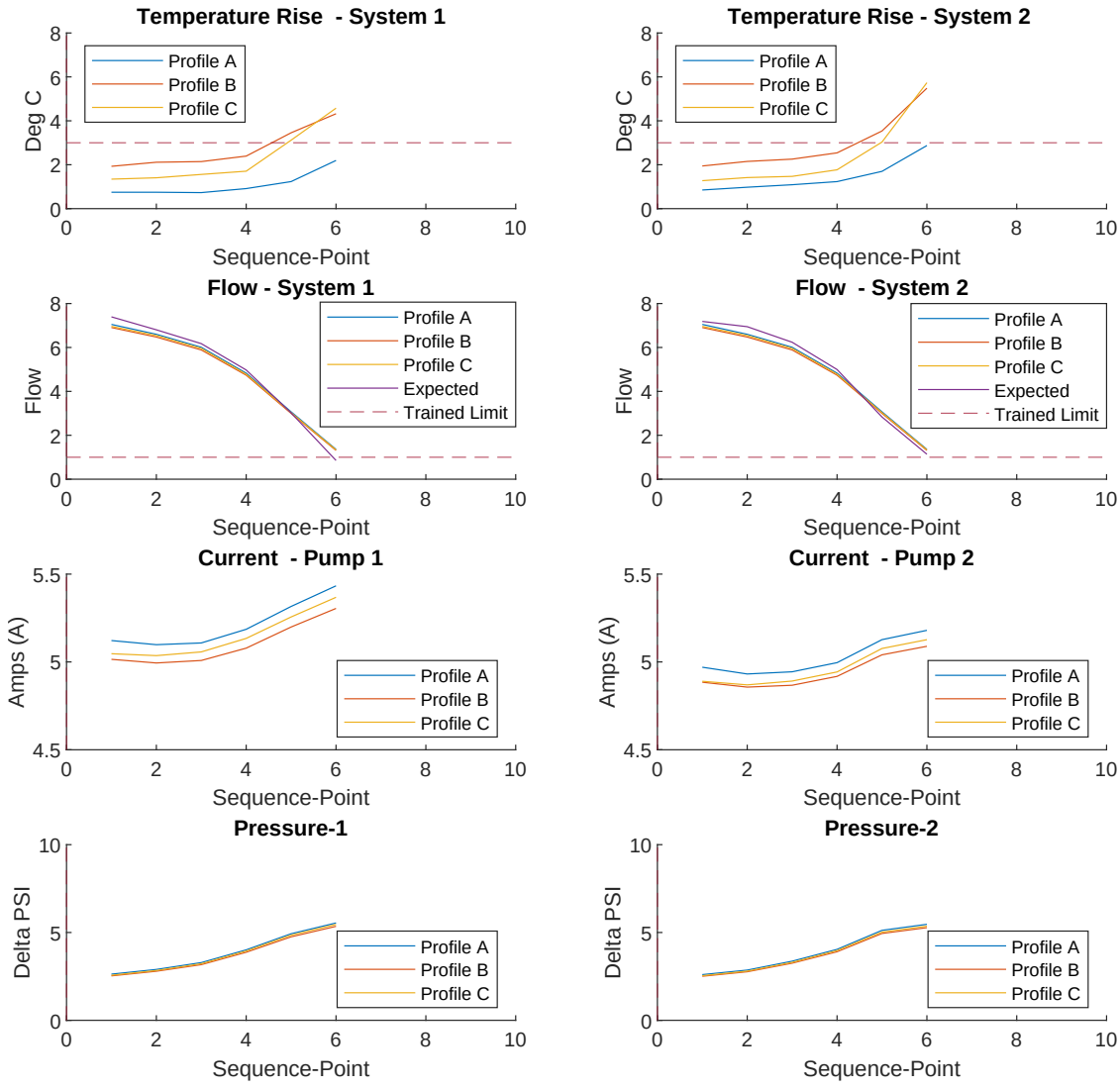


Figure 4.14: RUL Profile 20 - Processed - Cooling

As shown above in Figure 4.14, the cooling system flow drops below 1 LPM triggering a system failure on sequence-point 6 as a result of a clog injected into the system. The temperature profiles shown in the top row of subplots represents the temperature rise across

the heaters which are used to inject the waste heat proportional to the current system losses. The temperature profile rises across the run to failure profile and exceeds an arbitrary thermal limit of 3 degrees Celsius for operational profiles B and C, however the system is able to stay within the thermal limit until sequence-point 6 for operational profile A. The clog profile causes a rise in pressure across the pump depicted in the bottom subplot of Figure 4.14 and a rise in pump current, shown in the third row of subplots for Figure 4.14. The fuel system continues to operate until it fails on sequence-point 8 as shown below in Figure 4.15, while cooling system data is limited to 6 sequence-points due to its failure of all operational profiles on sequence-point 6.

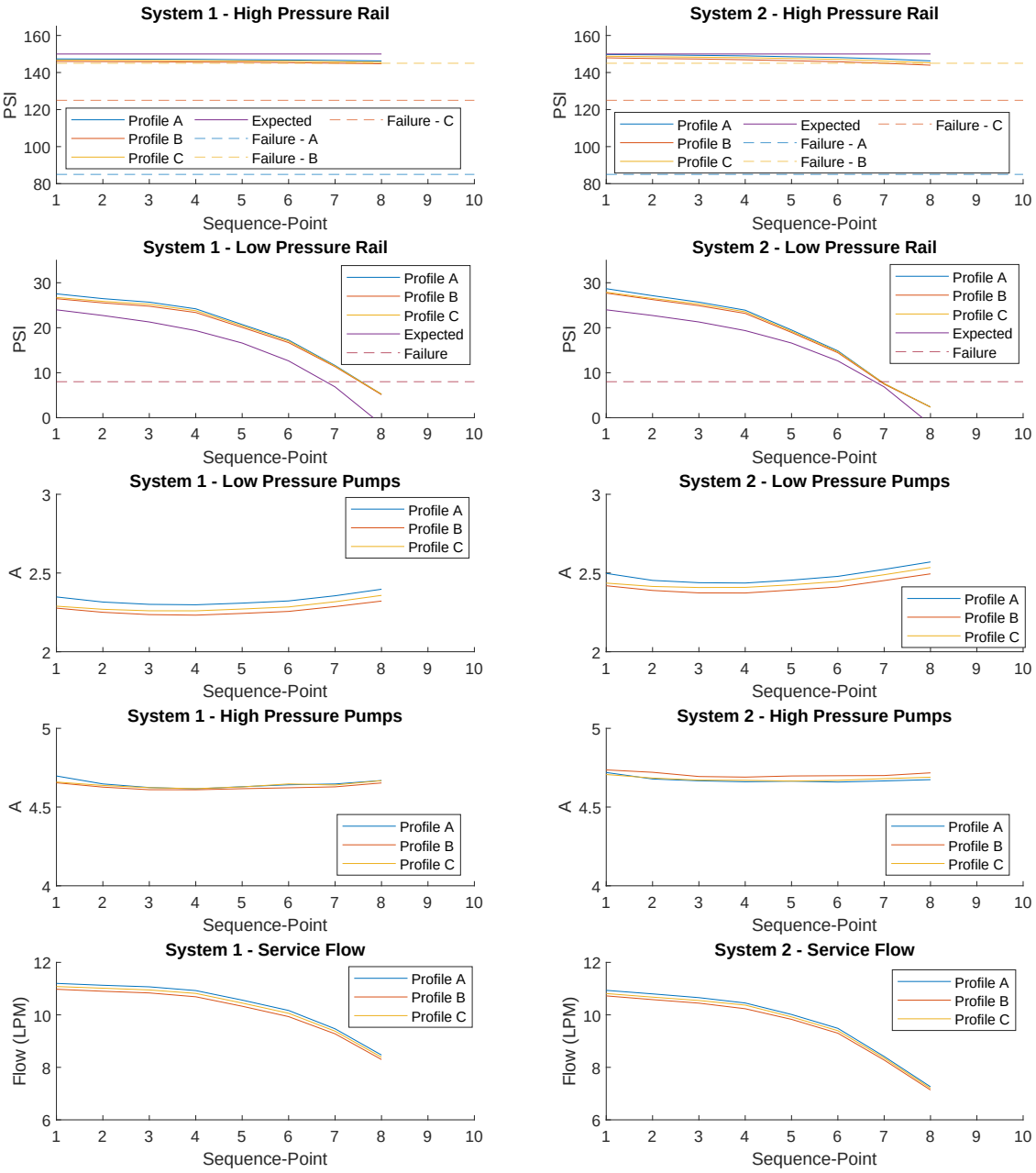


Figure 4.15: RUL Profile 20 - Processed - Fuel

As depicted above in Figure 4.15, the fuel system low pressure system fails on sequence-point 8, due to a clog injected in the system for both fuel systems 1 and 2. The failure limit is met on sequence-point 8, when the rail pressure drops below the system limit of 5 PSI. The system limit trips the fuel system offline failing the fuel system for all three operational profiles on sequence-point 8. The pressure after the clog for the low pressure flow paths gracefully degrades and is shown visually in the second subplot of Figure 4.15. The restriction causes a drop in flow for the service flow paths shown in the 6th row of the

subplot.

Figure 4.15 and Figure 4.14 represent an example of the hardware system run to failure dynamics for the fuel and cooling systems. 99 additional hardware simulation were conducted to produce the data set of 100 run to failure profiles. The additional profiles contain varied distributions of clogs and leaks for the fuel and cooling systems. An example of a leak for the cooling system is shown below in Figure 4.16 and for the fuel system in Figure 4.17 and Figure 4.18.

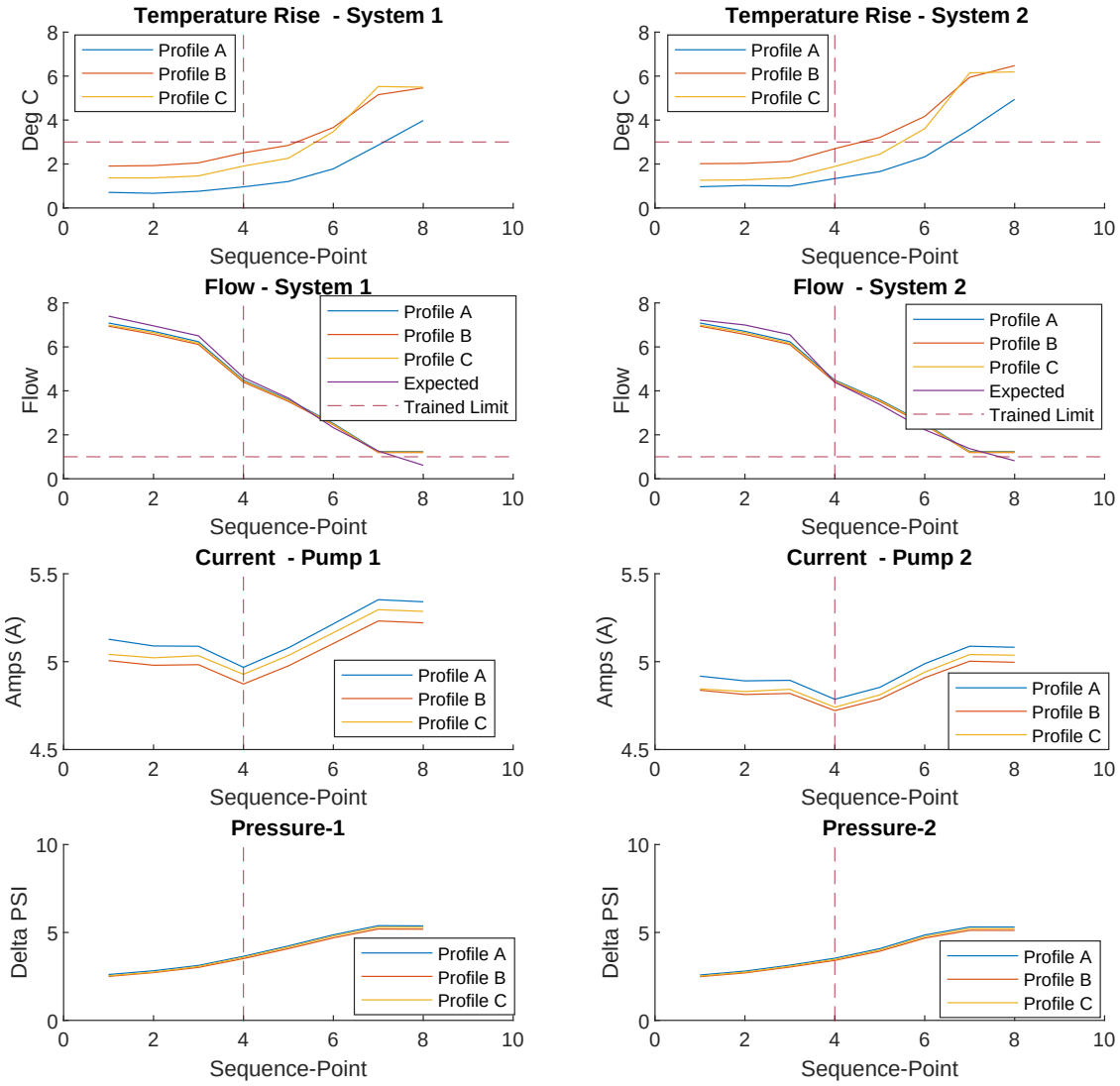


Figure 4.16: RUL Profile 14 - Processed - Cooling - Leak

As shown above in Figure 4.16, a leak in the cooling system was injected between sequence-point 3 and sequence-point 4, which caused a sharp drop in flow between sequence-point 3 and sequence-point 4. The leak is considered a system failure, causing the cooling system to

fail on sequence-point 4, however data was recorded until the failure limit in flow was met on sequence-point 8. For all profiles with leaks, data was recorded until the failure limit in flow was met. The extra data allows miss predictions for leaks to be better quantified, which is described further in chapter 5. The fuel system contained two possibilities for leaks, a low pressure leak shown in Figure 4.17 and a high pressure leak shown in Figure 4.18.

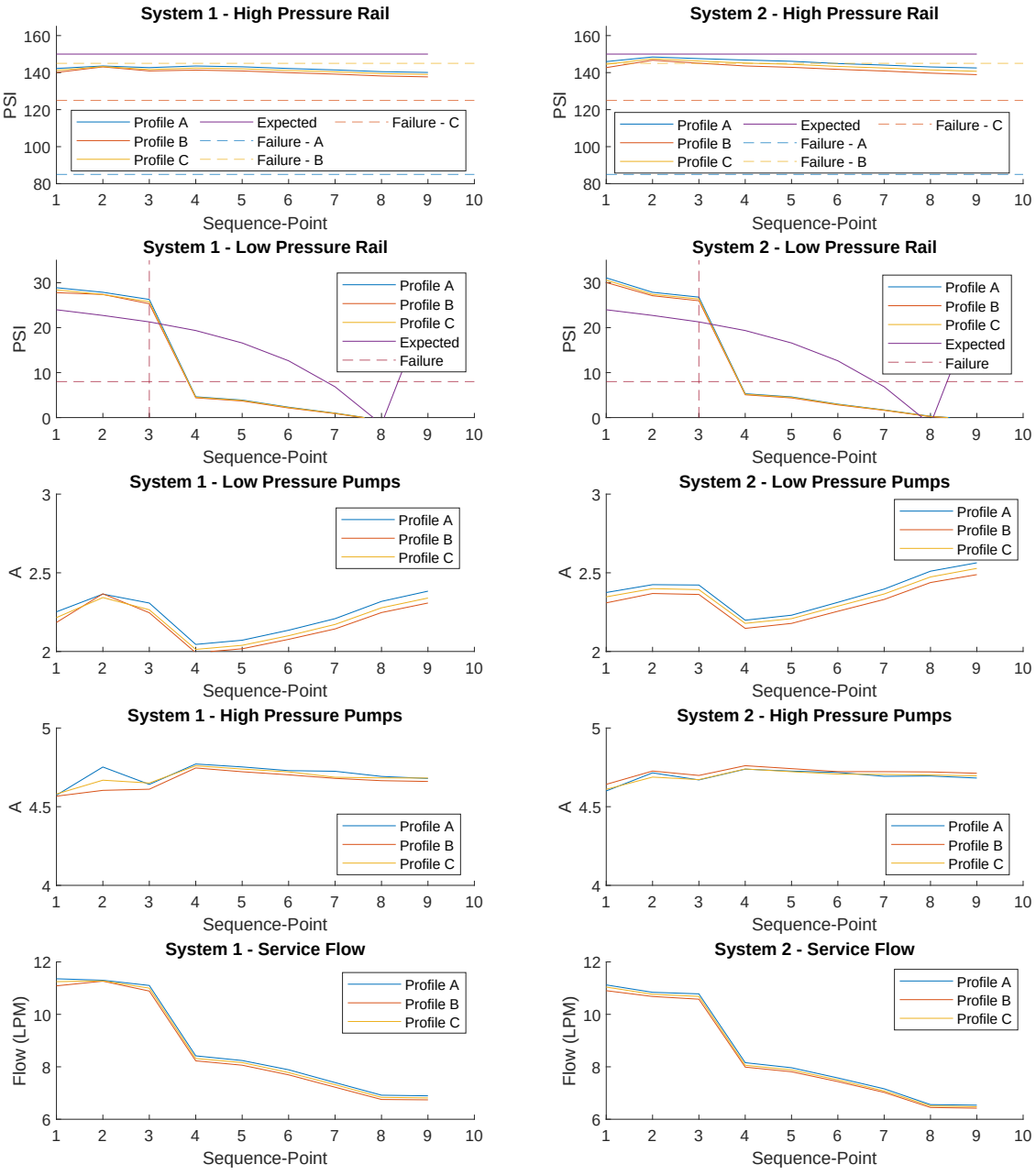


Figure 4.17: RUL Profile 12 - Processed - Fuel - Leak LP

The injection of a low pressure leak into the fuel system (shown above in Figure 4.17)

causes a sharp degradation in system pressure, which normally would trip the system offline, however the system is continues to operate until either the HP fuel system or cooling system fails. Similar to the cooling system leak process, the additional data is collected for the fuel system to improve the error metrics in leak detection, which is described further in the following chapter, Chapter 5.

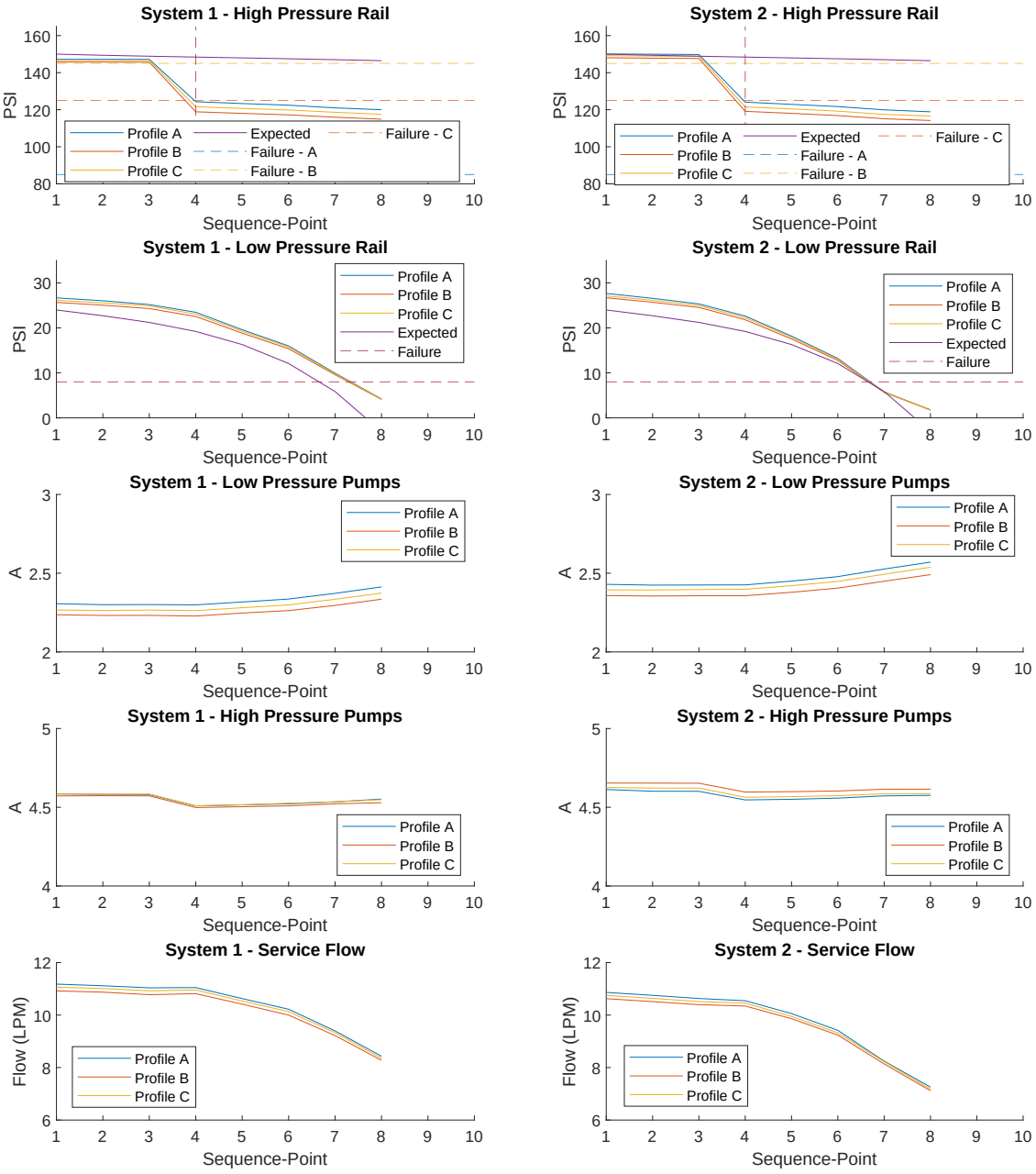


Figure 4.18: RUL Profile 35- Processed - Fuel - Leak HP

The injection of a High pressure leak into the fuel system (shown above in Figure 4.18)

causes a sharp degradation in system pressure, which normally would trip the system offline, however the system is continues to operate until either the LP fuel system or cooling system fails. Similar to the cooling system leak process and LP fuel system leak process, the additional data is collected for the fuel system to improve the error metrics in leak detection, which is described further in the following chapter, Chapter 5.

The 100 failure profiles are injected with clogs and leaks leveraging the distributed failure profiles defined in Subsection 4.2.5. The previous 5 figures and text provide examples of the possible faults for the fuel and cooling system. The 100 failure profiles have a total individual file count of over 16,000 files. This large file count required a post processing code for data scaling and a data repository constructed prior to recording hardware data to ensure data was properly stored and scaled. These processes are discussed in the following subsection. Using the post processed data, further processing was conducted unique to the prognostics and run to failure work, which is defined in Subsection 4.5.3.

### 4.5.2 Initial Post Processing and Data Repository

The total individual file count for all 100 run to failure simulations was estimated to be about 16,200 files. This estimation was determined by:

$$File_{count} = (Failure\ Profiles) * (Days_{avg}) * (fileseachrun) * (Operational\ Profiles) \quad (4.5)$$

Where 100 failure profiles simulated in hardware each containing an average of 9 sequence-points. For each of the $\sim$ 9 sequence-points, three operational profiles were simulated in hardware and recorded. Each of the three operational profiles produce 7 unique output files (due to the varied sample rates within the laboratory). Provided the large estimation for total output files, a post processing code and a structure for the data repository was constructed prior to hardware simulations.

To effectively store this data a nested file structure was constructed where a singular *RUL Dataset* folder contained 5 sub folders; *raw data*, *processed data*, *average value data*, *figures*, *control*, and *detailed processed data* folders. The *raw data*, *processed data* and *average value data* folders are leveraged for saving the original hardware data and initial processing. The *detailed process* and *figures folder* are discussed in the following subsection of this chapter. The control folder contains the 100 run to failure fault injection profiles csv files used for hardware system fault injection and the operational profile csv used for hardware operational profile control.

The raw data folder contains a sub folder for each of the 100 run to failure profiles. Each

sub folder contains the 7 raw output files from a given run to failure hardware simulation profile. The initial processing code was used to load data from each failure profile, scale the data from raw output signal valves to engineering values (flow, pressure, voltage, current, etc.), shift the time vector to start at 0 seconds instead of the original clock time for the embedded controller, and produce average values for all signals across each record window. The scaled and time corrected data is stored in the processed data folder. The average value data is concatenated into three individual files for each failure profile, representative of the three operational profiles. Additional information about the post processing code is provided in subsection 2.9.

### 4.5.3 Failure Profile Processing

Using the processed time series data from the past subsection, the data was then scaled, trimmed and data acquisition errors were mitigated.

In the hardware acquisition of each run to failure profile, when a system failed prior to another, it was returned to the full health position (absent of clogs or leaks) and remained online until the second system failed, terminating the simulation, An example of this is shown visually below in Figures 4.19 and 4.20.

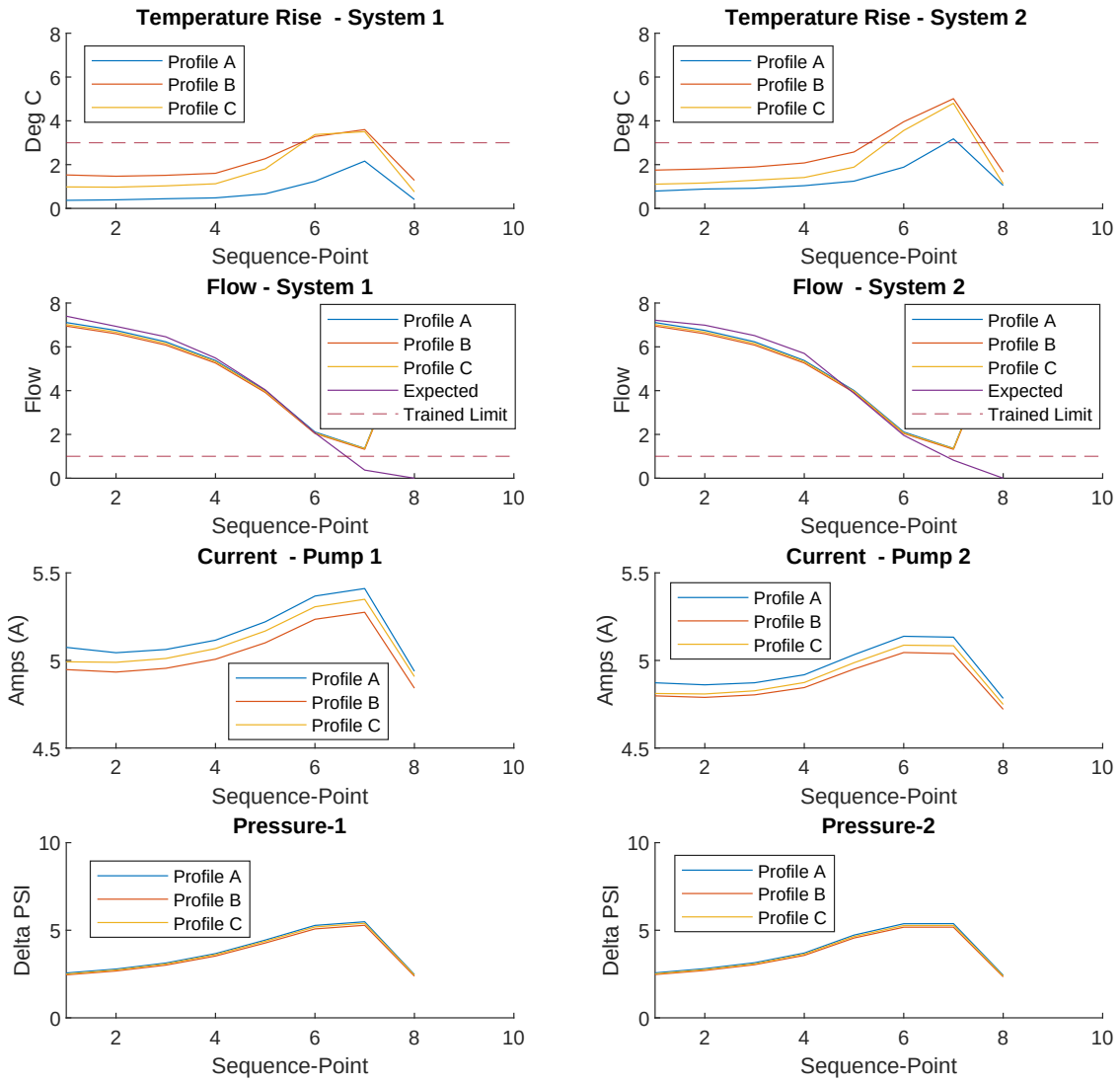


Figure 4.19: Failure Profile 4 - Data Trimming -Not Trimmed - Cooling

As shown above in Figure 4.19 the cooling system reaches the flow failure limit on sequence-point 7. Instead of tripping offline, the system is returned to full health and remained online until the fuel system failed on the following sequence-point. The fuel system failure is shown below in Figure 4.20 followed by the trimmed cooling system profile shown in Figure 4.21.

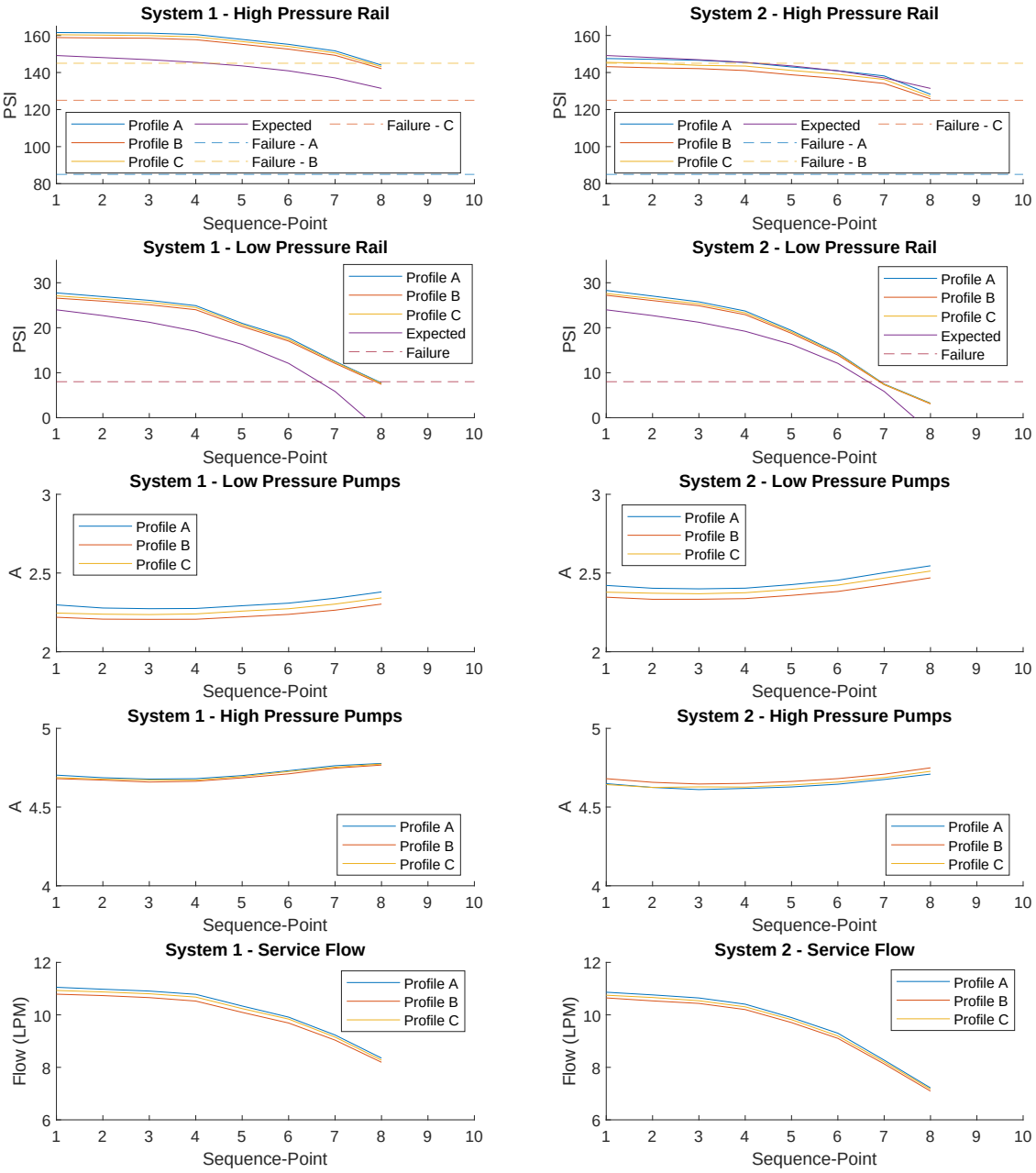


Figure 4.20: Failure Profile 4 - Data Trimming - Fuel

As shown above in Figure 4.20, the LP fuel system limit is met on sequence-point 8, terminating the simulation. Data for the system which fails first, which in this case is the cooling system, is trimmed to its' actual failure sequence-point shown visually in Figure 4.21. The fuel system data did not required any trimming as the simulation terminated when the fuel system failure limit was met. The cooling system however, required removal of the return to steady state data on sequence-point 8, which is shown visually below in Figure 4.21.

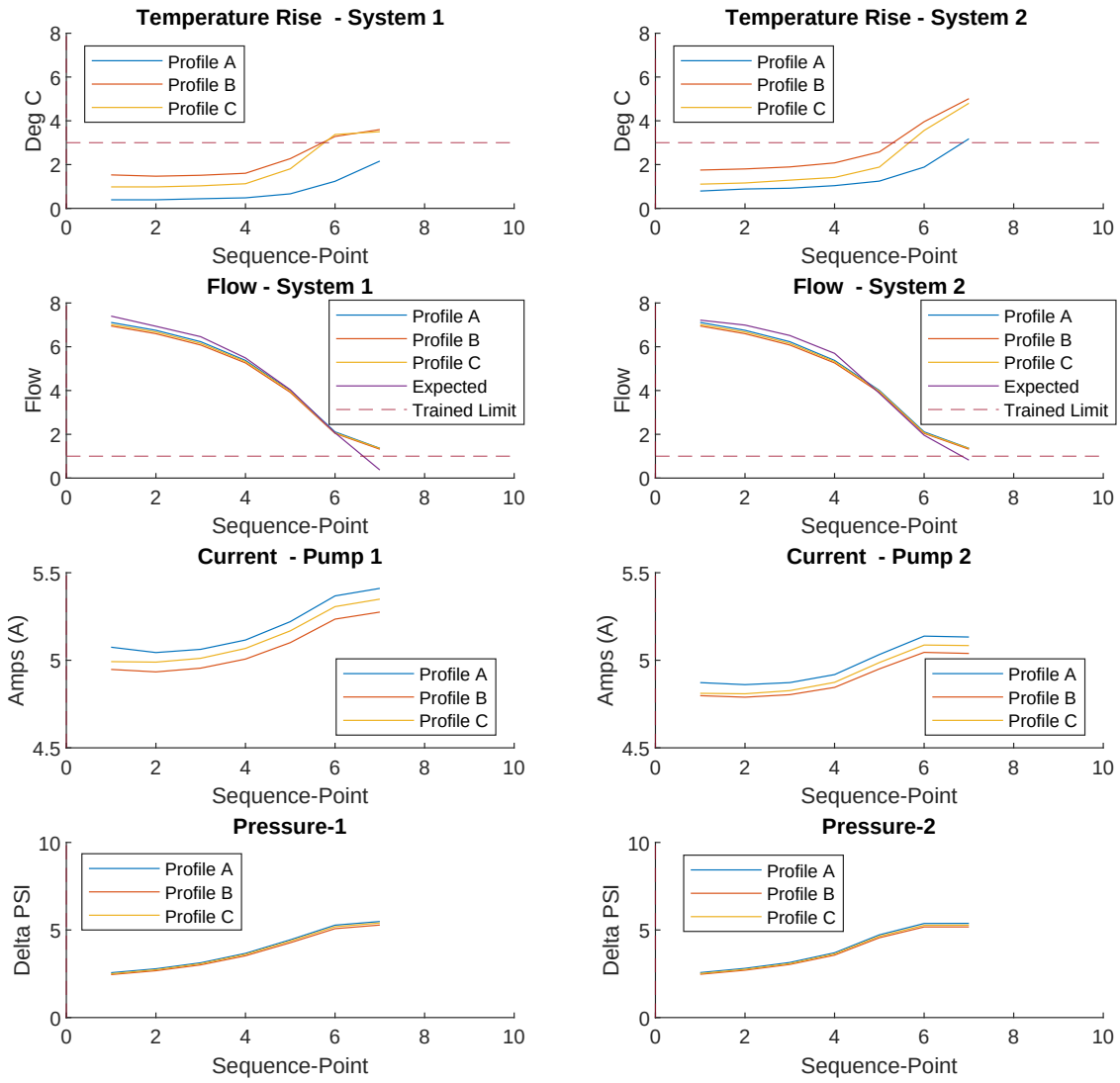


Figure 4.21: Data Trimming - Trimmed - Cooling

As shown above in Figure 4.21, the cooling data was trimmed to 7 sequence-points from the original duration of 8 sequence-points shown in Figure 4.19.

In addition to trimming profiles, profiles with DAQ errors were corrected for the cooling and fuel systems. The correction method varied for each system. An example of a DAQ error for the cooling system is shown visually below in Figure 4.22.

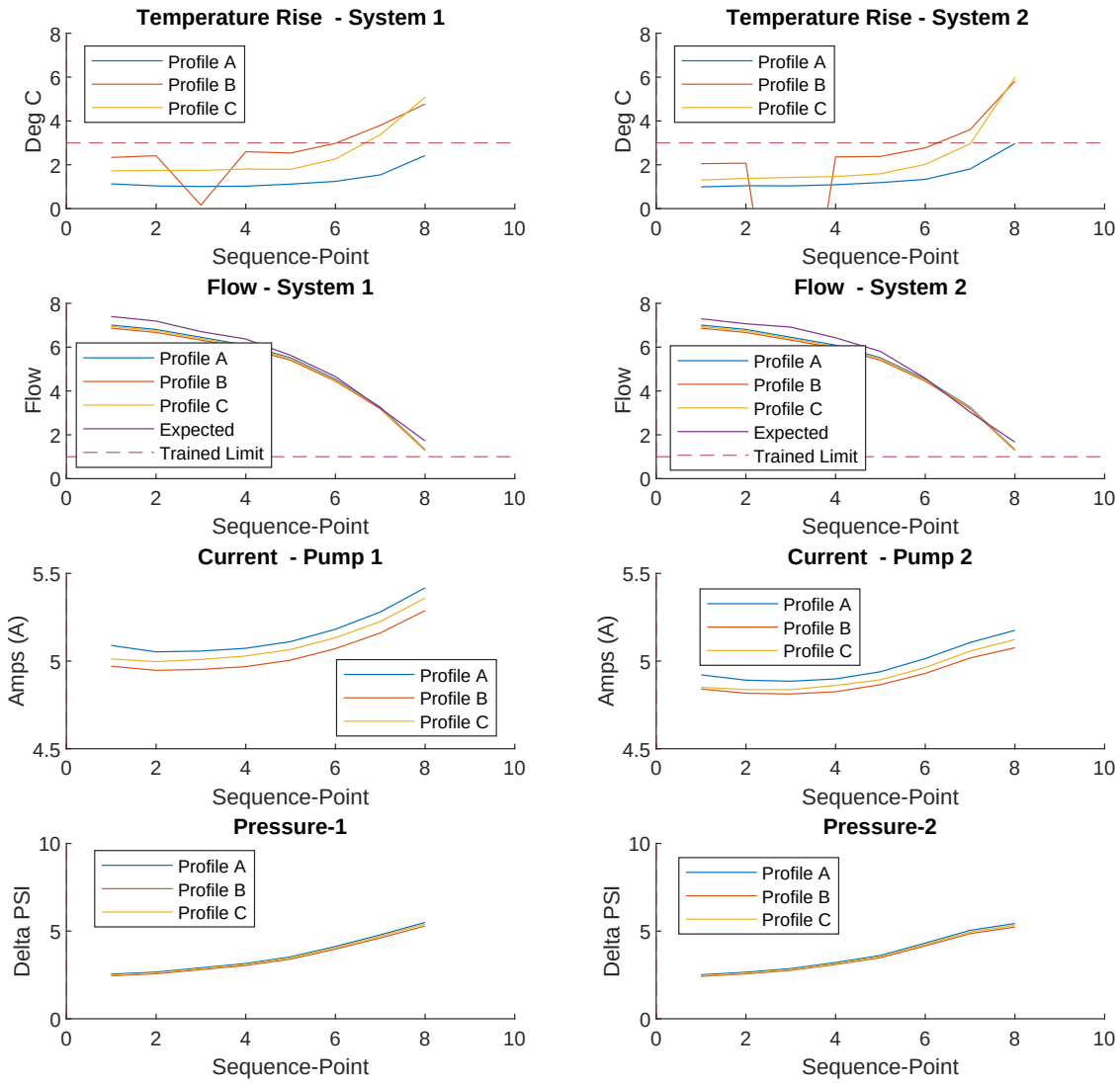


Figure 4.22: Failure Profile 26 - Cooling System - Example DAQ Error

As shown above in Figure 4.22 the change in temperature across the heater for profile B in systems 1 and 2 is below 0.5 °C and visually inconsistent with the other temperature profile patterns. These anomalies exist in voltage based acquisition signals for both the cooling and fuel system in less than 10 % of the profiles. The root cause for the error in temperature delta across the heater was a result of high Electromagnetic interference (EMI) within the laboratory. The EMI caused the DAQ module to exceed module safeguards placing the module in a protection mode, invalidating the data. Given the small data set size of 100 profiles, it was desired to correct for these errors instead of simply throw the profiles out. An example of a corrected profile is shown below in Figure 4.23 where the original profile is shown in Figure 4.22.

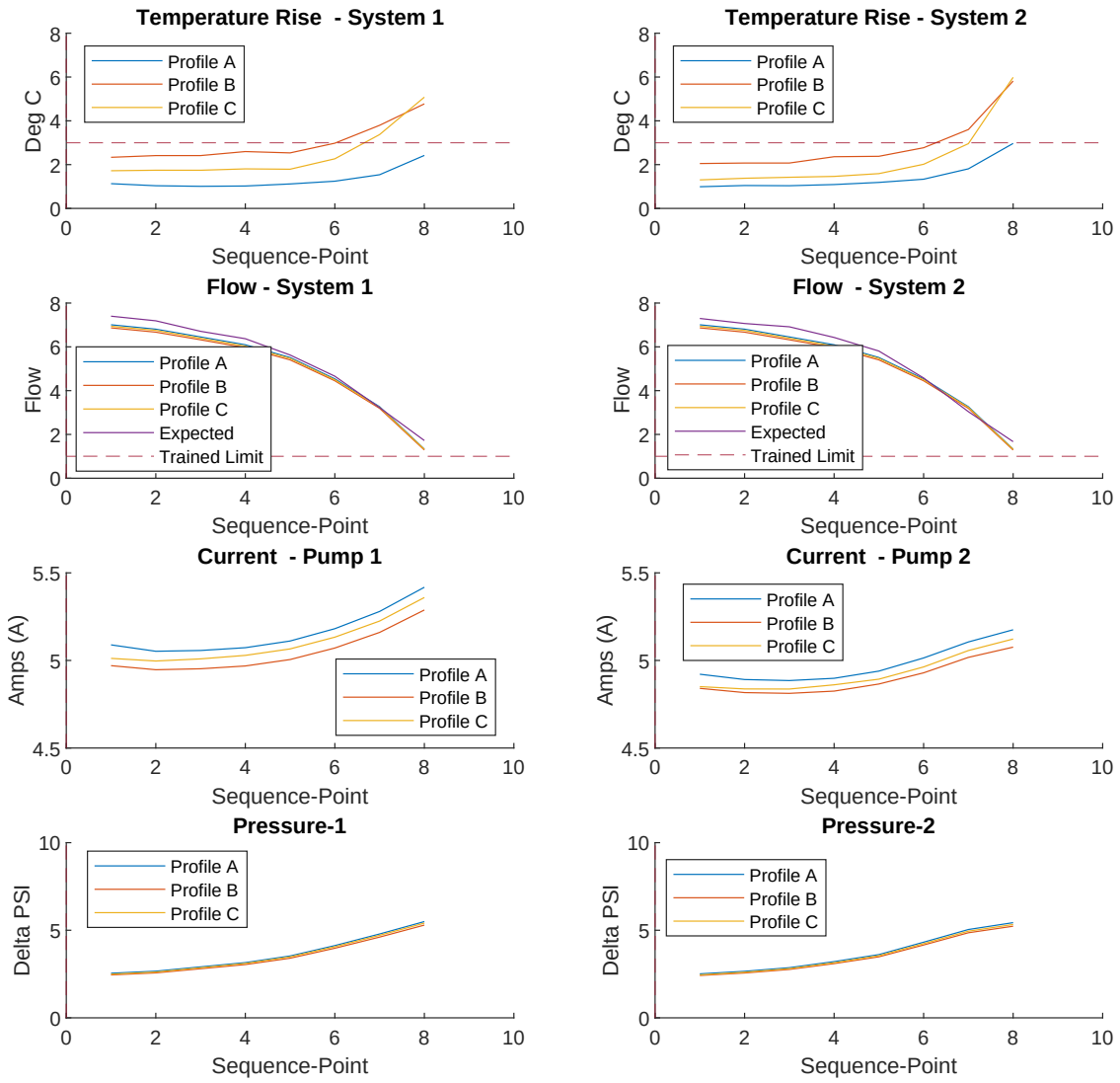


Figure 4.23: Failure Profile 26 - Cooling System - Example DAQ Correction

To do so the following signal limits were used defined below in table 4.9.

Table 4.9: Cooling System - Signal Limits

| Signal | Upper Limit | Lower Limit | Units |
|---|---|---|---|
| Temperature Delta | 0 | 10 | °C |

Using limits defined in table 4.9, if a signal was out of tolerance the previous value replaced the invalid value. The logic was effective as data acquisition errors never occurred for two consecutive runs.

The Fuel systems leveraged a voting system to remove inconsistencies in the fuel system data due to data acquisition errors. A voting system was selected and integrated as a result

of the near identical values for a given run across all three operational profiles. This process was not considered for the cooling system as data varied for a given run across the three operational profiles. A visual of the voting system process is shown below in Figure 4.24.

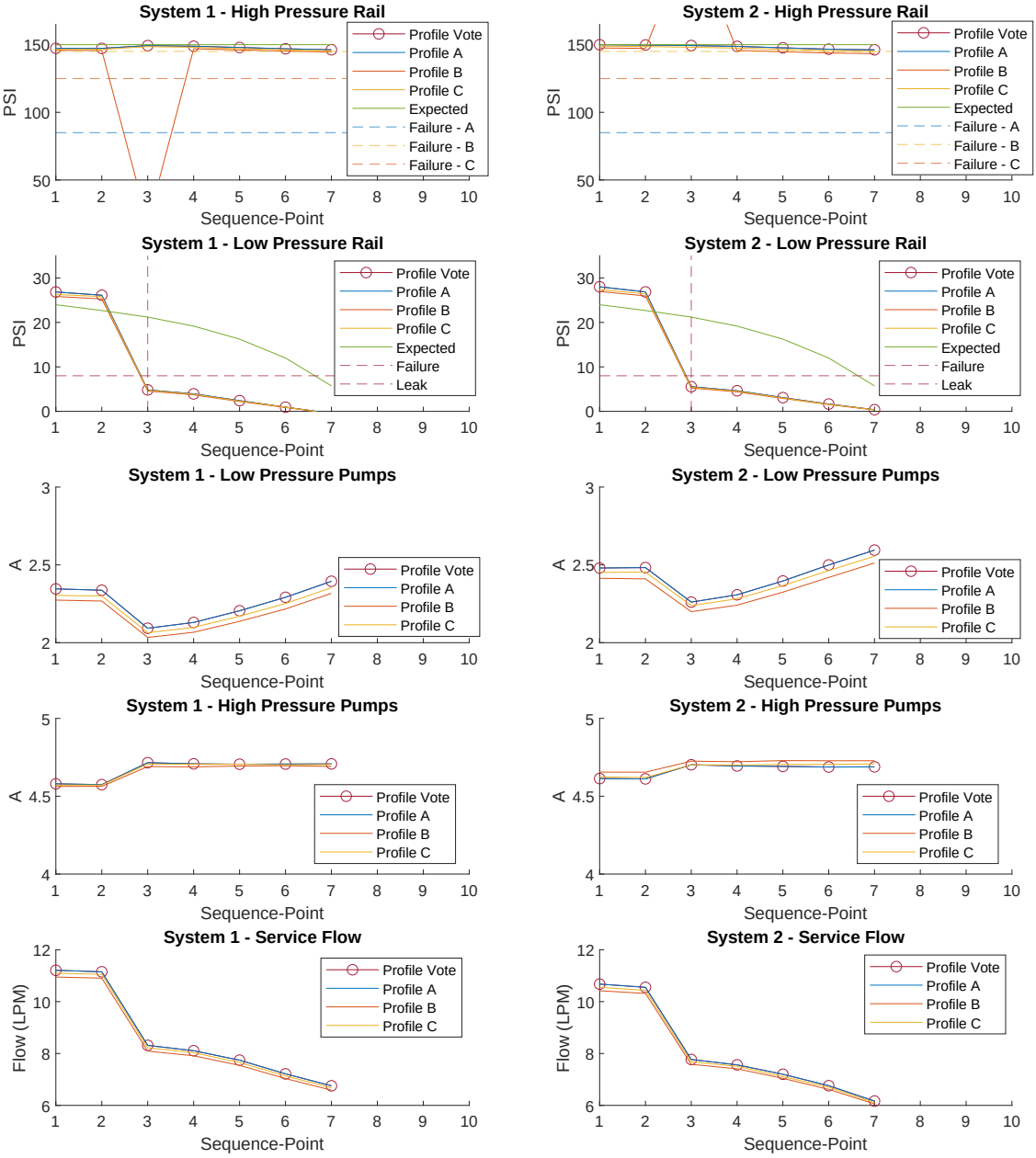


Figure 4.24: Failure Profile 72 - Fuel System - Voting System

Shown above in Figure 4.24, the circular points represent the selected data from the voting system. The for each run and each signal the voting system compares the values for profiles A-C. The voting system uses profile A as the base value, if profile A matches (where a match is defined as a value within a $1 \pm \%$ tolerance of Profile A) profile B or Profile C, the valve for

profile A is selected. However, if profile A does not match profile B or Profile C, then profile B and C are checked for a match, if profile B and C match, profile B is selected. However if profile B and C do not match then there is no agreement between 2 of the three profiles and an error is flagged. In the acquired data an agreement between 2 of the 3 operational profiles for a given run and signal for the cooling system was always achieved. By implementing a voting system, the fuel system data was reduced down to a singular average of the three operational profiles and data acquisition errors were eliminated for the fuel system.

## 4.6 Summary

Using the MLSMP, defined in Chapter 2, 100 run to failure (RTF) profiles were in this Chapter. The failure profiles injected common faults into the cooling and fuel systems, which caused a degradation in system performance until both the cooling and fuel system failed. Data was collected over a period of 10 sequence-points or until both the fuel and cooling systems had failed using the MLSMP. The 100 failure profiles that were recorded in hardware were configured using a constructed software model of the fuel and cooling system in conjunction with a clog model from literature [3]. The RTF dataset constructed within this Chapter provides the necessary inputs to explore the application of Artificial Intelligence for diagnostics and prognostics of the RTF profiles constructed within this chapter.

# CHAPTER 5

# Forecasting Plant Level Capability

## 5.1 Introduction

This chapter explores the applicability of Artificial Intelligence (AI),with the selection of a long short-term memory (LSTM) Recurrent Neural Network (RNN), to perform diagnostics and prognostics on the Michigan Laboratory-scale Ship Machinery Plant (MLSMP) through a multi-layer framework. Using the run to failure (RTF) profiles constructed throughout Chapter 4, a multi-step processes is proposed to form the final multi-layer framework. The diagnostic task will attempt to detect leaks in the supporting plant systems (cooling and fuel). The prognostic task will focus on the prediction of growing clogs in the fuel and cooling system and their future impact on overall plant capabilities in the future. The proposed process to build this novel multi-layer prediction framework is shown in Figure 5.1.

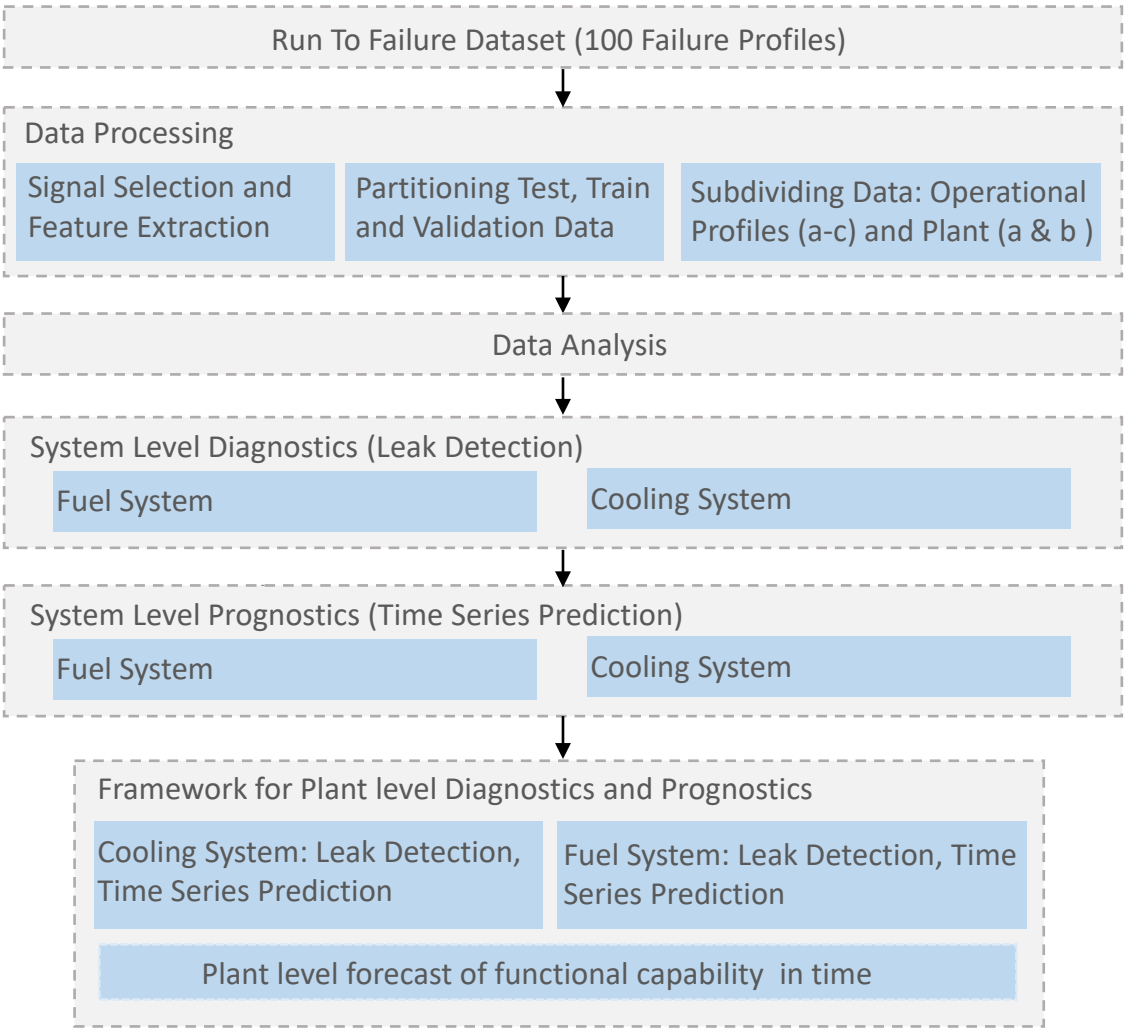


Figure 5.1: Proposed Exploration Process for Plant level Prognostics

The process developed a flexible dataset using indices to enable the ability to efficiently select variations in input parameters including: input signals, plant selection, and operational profile selection, and test, train and validation data partitions. Provided the finalized dataset, initial signal analysis was performed to determine the potential correlation between faults and failures (clogs and leaks) and input signals, providing a initial selection of dataset indices to explore potential AI algorithms for the diagnostic and prognostic tasks. AI algorithms are first explored, selected and evaluated across a range of input data at the system level(for each individual system) for the diagnostic and then for prognostic task. Leveraging the initial diagnostic and prognostic work, a plant level algorithm is formed to enable the diagnosis of current plant state for leaks within the fuel and cooling systems (leak vs. no leak) and predict the ability to complete varying operational profiles in the future given a degrading state of system health. An overview of content found in each of the subsequent sections is

provided in the following paragraph.

Section 5.2 first defines the plant configuration and its respective failure distributions used throughout work in this Chapter. Section 5.3 begins the proposed exploration process illustrated in Figure 5.1 and discusses the conducted data processing. Data processing was conducted to provide necessary indices to extract varied combinations of desired data within the larger run to failure dataset. Using the formed dataset from Section 5.3, the following Section 5.4 reviewed the variance of each input signal with respect to failure sequence-point and leak state to provide initial insight into signal selection which informed the initial data selection for the exploration of AI methods. Section 5.5 reviews common AI based algorithms for Diagnostic applications to determine if a leak is present in the cooling or fuel system. Section 5.6 uses input data without the presence of a leak and applies an Long short-term memory (LSTM) based model to forecast potential limitations to future plant operational capability as a result of degradation in the cooling and fuel system. Section 5.6 focuses on the individual system (cooling or fuel) to forecast if the given system will degrade operational availability (ability to complete operational profiles A-C) in the future, given its current and trending degradation in system health. Section 5.7 combines system level diagnostic and prognostic algorithms into a common framework to diagnose the current state of the plants health and predict operation availability for operational profiles (A-C) in time. Section 5.8 provides a summary of the insight gained throughout this chapter, in efforts to close the knowledge gap for unmanned system operation.

## 5.2 Notional Machinery Plant and Failure Profiles

### 5.2.1 Overview

This section is divided into two key elements, an overview of the plant configuration used for work throughout this chapter and an overview of the faults and run to failure profiles.

### 5.2.2 Plant Configuration

The hardware plant was configured with MSB1 and MSB2 each powered from a single generator and uncoupled from each other. The mission and support loads placed on both busses were identical as well as the faults injected into the respective support systems. The isolation between the two sides of the power plant provides two near identical run to failure profiles on near identical hardware. The portion of the machinery plant with MSB1 and its respective loads and source (generator 1) is defined as plant 1 and the portion of the

machinery plant with MSB2 and its' respective loads and source (generator 3) is defined as plant 2. The two plants within the MLSMP are shown visually below in Figure 5.2.

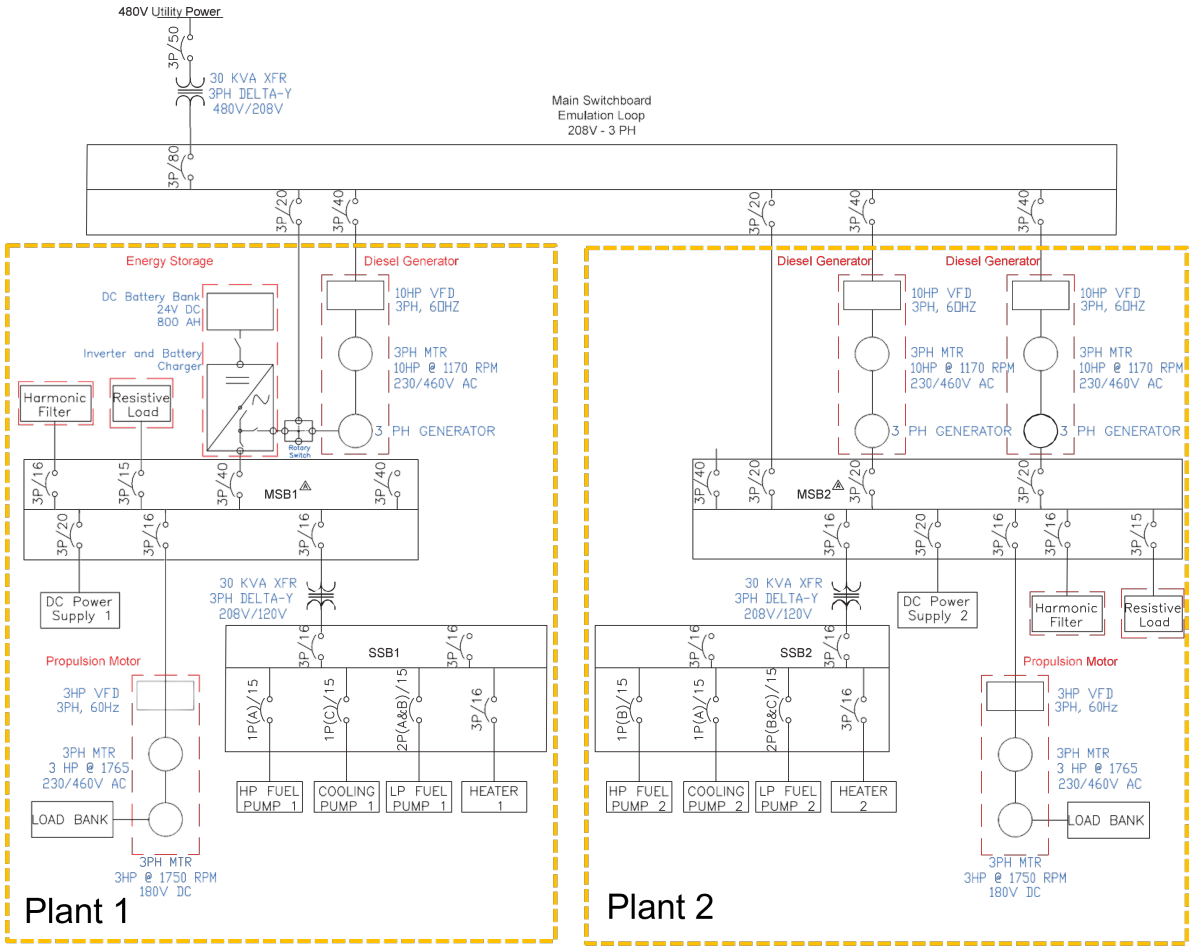


Figure 5.2: Overview - Plant 1 and Plant 2

### 5.2.3 Failure Distribution

The 100 RTF profiles are defined in detail in Chapter 4 and are summarized in this Subsection prior to their use throughout this Chapter. The RTF profiles were conducted over a period of up to 10 sequence-points with each sequence-point recording a 10 second steady state window of data from three operational profiles. For each run to failure profile, there was a probability for failure through through clogs and leaks injected into the fuel and cooling systems. Leaks in both the fuel and cooling system were had a probability of occurrence during sequence-point 2-4 of operation. If a leak occurred in any system, the given RTF profile was considered failed prior to the prediction of clogging in the fuel and cooling system. While the injection of system leaks were small and did not affect system (cooling or fuel) performance, the

leaks were defined as a failure due to the spilling fuel or raw water that would occur in the engine room in the event of a leak. Randomly distributed clogs were injected into the fuel and cooling system (detailed in Chapter 4), these clogs began on sequence-point one and did not cause a degradation in system capability until sequence-point 6-10. The constructed failure profiles were designed to leverage system information up to sequence-point 5, with the flexibility to use data from sequence-points 4-6, and predicted the plant level capability by defining the failure sequence-point for each of the three operational profiles in a given RTF profile. The cooling system failure sequence-point was dependent on the plant losses and thus the plant loading or operational profile. The cooling system experienced a reduction in capability due to decreased cooling capacity as clogs in the system built over time. For example, the cooling system may not have sufficient ability to cool the waste heat for a high load situation (operation B) but has the capacity to cool the system for a low load operation (operation A). The fuel system failure sequence-point was independent of operational loading. Fuel system clogs built slowly in the low and high pressure systems but system capacity was not affected until the clog exceeded the capability of the pumps causing the rail pressure to sharply decrease, reducing fuel injection ability below the necessary threshold for all three operational profiles. The distribution of these failures across the 100 RTF profiles is defined below in Table 5.1.

Table 5.1: Distribution of Actual Dataset Failure Modes

| **System** | **Clog (Profile Count)** | **Leak (Profile Count)** |
|---|---|---|
| **Cooling** | 11 | 18 |
| **Fuel** | 27 | 11 |
| **Fuel and Cooling** | 30 | 3 |
| **Total** | 68 | 32 |

Table 5.1 provides the breakdown of failure modes and their respective system origin. Failures are broken down by system origin and failure type. The leak category defines failure profiles where a leak is present in the cooling system, fuel system or both the cooling and fuel system. Leaks occur between sequence points 1 and 4 and are defined as a plant level failure for the given profile. For the 68 profiles without a leak clogging in the fuel and cooling system cause the given profile to eventually fail. The 11 failure profiles that make up clogging in the cooling system are unable to perform any operations (a-c) due to overheating prior to the fuel system affecting plant level performance. The 27 failure profiles that make up clogging in the fuel system cause the plant to fail due to the insufficient functionality of the fuel system prior to any degradation in operational performance for the cooling system.

The fuel and cooling category for clogging represents the failure profiles where a degradation in cooling system operational availability is present or the cooling system has the capacity for 1-2 operational profiles but not three, and prior to the inability to perform any operational profiles as a result of cooling system degradation, the fuel system degradation causes a plant level failure.

The multiple failure modes and their respective injection distributions for the 100 RTF profiles provide a range of failure sequence-points for operational profiles A-C, which is depicted in Figure 5.3.

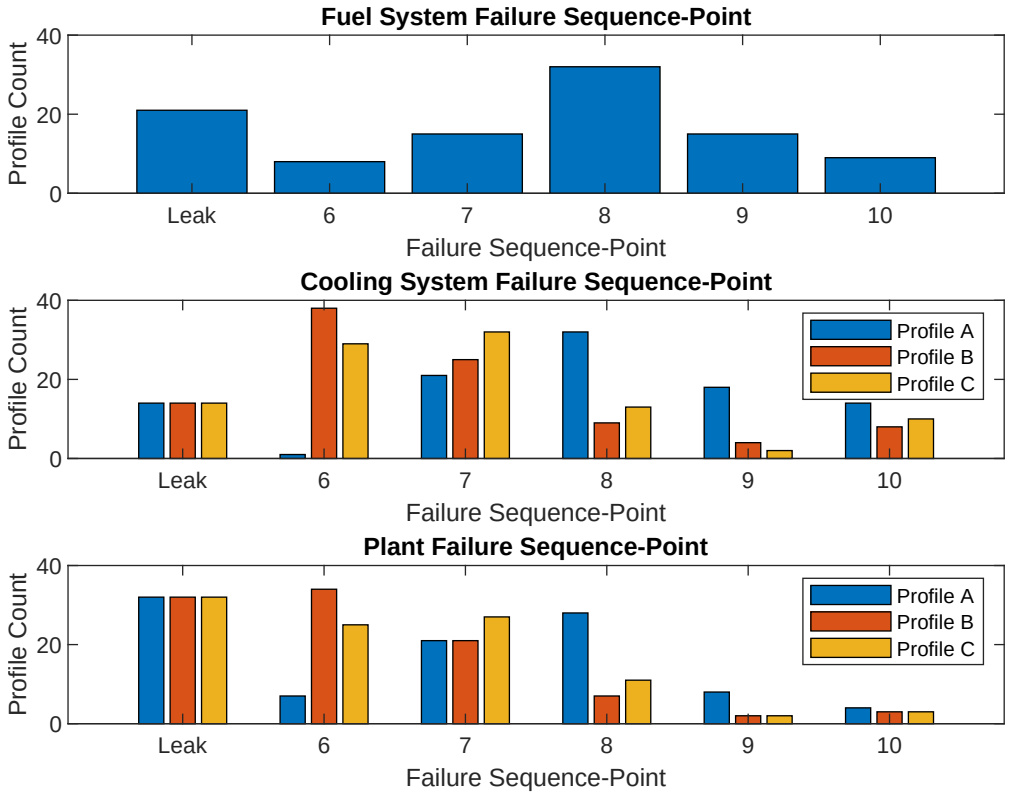


Figure 5.3: Dataset Failure Distribution

Figure 5.3 illustrated the distribution of system and plant level failures for the three operational profiles through three bar charts. The top bar chart depicts the fuel system failure for the 100 RTF failure profiles providing the sequence-point the system fuel system produces a plant level failure. The middle bar chart illustrates the sequence-point the cooling system is unable to provide the necessary capability to dissipated the waste heat produced by the respective operational profile. The final bar chart illustrates the failure sequence-point for each operational profile provided the state of health for both the cooling and fuel systems.

### 5.2.4 Summary

The 100 RTF profiles generated with simulated failures from literature and injected into the MLSMP discussed in detail in Chapter 4 are leveraged as input data for fault detection and prediction of plant capacity in time provided the injection of common fuel and cooling system faults and failures. The MLSMP is operated as two identical and isolated sub-plants with identical equipment, operational loads and fault injection across the 100 RTF profiles. For the work in this Chapter, the MLSMP and the two identical sub-plants are referred to as plant 1 and plant 2. Both plants (1 and 2) simulate in hardware 100 RTF profiles each consistent of up to 10 sequence-points of operation, with each sequence-point recording 10 seconds of steady state data for three operational profiles (A-C). For each of the 100 RTF profiles there is a randomized and independent probability of a leak in the fuel high pressure and low pressure systems as well as the cooling system. In addition to leaks there is a randomly distributed and independent clog, which increases across the RTF profile for the cooling system and fuel high pressure and low pressure systems. The multiple modes of failure and system degradation for the cooling and fuel system produce complex and interdependent interactions within the machinery plant, affecting overall operational performance until plant failure.

## 5.3 Input Data and Data Prepossessing

### 5.3.1 Overview

This section defines the processing and finalized input data, with respective indices leveraged throughout this chapter for the detection of system leaks and prediction of plant capacity in time. Using the 100 RTF profiles defined in Chapter 4 and the defined MLSMP configuration and failure distribution defined in Section 5.2 laboratory data from the 100 RTF profiles was processed to produce input data for AI framework exploration. Indices were created to allow selection of desired operational profile(s), desired plant subsystems (plant 1 and plant 2), desired signals and features, and desired allocation for partitioning data into test, train and validation groups. The first Subsection of this section discusses signal and feature selection, followed by the second Subsection, which defines the partitioning of data into test, train and validation. The final selection summarizes the formed input data and indices.

### 5.3.2 Signal and Feature Extraction

The discussion of signal selection and feature extraction in the subsequent paragraphs of this subsection are with respect to each individual plant (plant 1 and plant 2). Steady state, average value data was first extracted and used to form a singular value for each of the desired signals for a given failure profile, sequence-point and operational profile. The input signals are listed below in Table 5.2.

Table 5.2: Input Signals - Average Value Data

| **Signal Name** | **System** | **Unit** |
|---|---|---|
| Heater Inlet Temperature | Cooling | °C |
| Heater Outlet Temperature | Cooling | °C |
| Flow | Cooling | LPM |
| Pump Current | Cooling | $A_{RMS}$ |
| Pressure 1 | Cooling | PSI |
| Pressure 2 | Cooling | PSI |
| Flow - LP | Fuel | LPM |
| Flow - HP Rail | Fuel | LPM |
| Flow - HP Relief | Fuel | LPM |
| Pressure - LP | Fuel | PSI |
| Pressure - HP | Fuel | PSI |
| Pump Current - LP | Fuel | $A_{RMS}$ |
| Pump Current - HP | Fuel | $A_{RMS}$ |

The 13 signals listed above are identical for cooling system 1 and 2, producing a total of 23 selected signals of average value data. For both sides of the plant cooling system heater input and output signals were used to form a singular input signal representing heater temperature delta. Similarly, the pressure signals before and after the clog for both cooling systems were used to form a singular input signal for pressure delta across the restriction. The average value signals were indexed into three groups (signal groups: 1-3) to enable trade off studies between input signal and prediction accuracy. The average value input signals and their respective indices are provided below in Table 5.3.

Table 5.3: Input Data - Average Value Signals

| **Signal Name** | **System** | **Unit** | **Signal Group(s)** |
|---|---|---|---|
| Heater Temperature Delta | Cooling | °C | 1 |
| Flow | Cooling | LPM | 1 |
| Pump Current | Cooling | $A_{RMS}$ | 1,2,3 |
| Pressure Delta | Cooling | PSI | 1,2 |
| Flow - LP | Fuel | LPM | 1 |
| Flow - HP Rail | Fuel | LPM | 1 |
| Flow - HP Relief | Fuel | LPM | 1 |
| Pressure - LP | Fuel | PSI | 1,2 |
| Pressure - HP | Fuel | PSI | 1,2 |
| Pump Current - LP | Fuel | $A_{RMS}$ | 1,2,3 |
| Pump Current - HP | Fuel | $A_{RMS}$ | 1,2,3 |

In addition to the average value signals defined above, power spectrum data was also collected and grouped to enable trade off studies between input signal and prediction accuracy. The four main components of interest for extracting power spectrum data are defined in Table 5.4.

Table 5.4: Desired Load and source power spectrum data

| **System** | **Component** |
|---|---|
| Fuel | Pump LP |
| Fuel | Pump HP |
| Cooling | Pump |
| Energy | Generator Ph A,B,C |

Data for both plant 1 and plant 2 is extracted for the desired loads and sources listed above in Table 5.4 using signals defined below in Table 5.5.

Table 5.5: Input Data - Waveform Signals

| Signal | System | Unit |
|---|---|---|
| Pump Current | Cooling | A |
| Pump Current LP | Fuel | A |
| Pump Current HP | Fuel | A |
| Gen Phase A Current | Genset | A |
| Gen Phase B Current | Genset | A |
| Gen Phase C Current | Genset | A |
| Bus Voltage Phase A | MSB | V |
| Bus Voltage Phase B | MSB | V |
| Bus Voltage Phase C | MSB | V |
| Bus Voltage Phase A | SSB | V |
| Bus Voltage Phase B | SSB | V |
| Bus Voltage Phase C | SSB | V |

The signals defined above in Table 5.5 are used as inputs to extract power spectrum harmonics for each of the four devices listed in Table 5.4. For each device the magnitude and frequency for carrier frequency and 5 largest harmonic frequencies are extracted and saved as input data. An example of the extracted data is provided below in Figure 5.4.

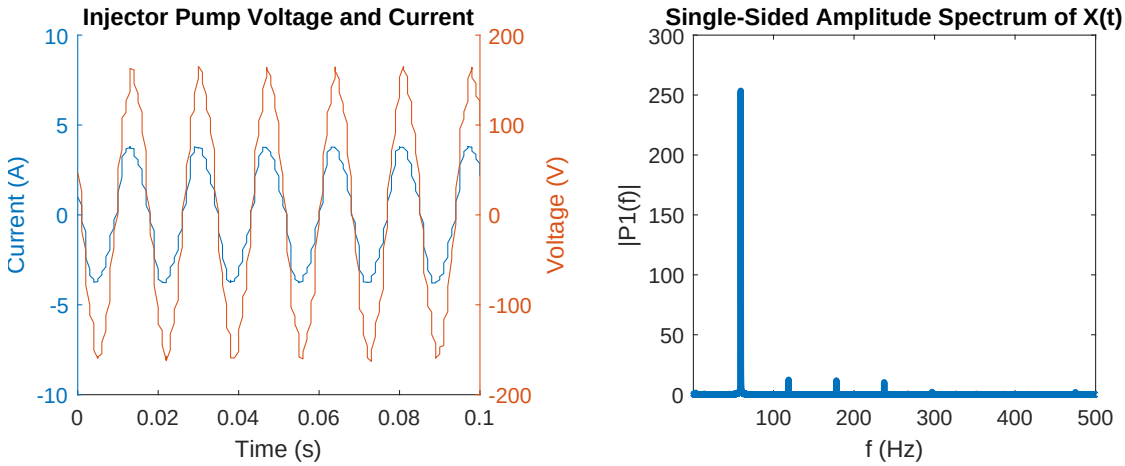


Figure 5.4: Power Spectrum Data

Figure 5.4 provides an example of a single extraction of power spectrum data for cooling pump 1 in failure profile 20, sequence-point 4 and operational profile 1. The power spectrum data was indexed into three groups (signal groups: 0,1,2) to enable trade off studies between

input signal and prediction accuracy. The power spectrum data input signals and their respective indices are provided below in Table 5.6.

Table 5.6: Power Spectrum Data Indices

| **System** | **Component** | index |
|---|---|---|
| Fuel | Pump LP | 1,2 |
| Fuel | Pump HP | 1,2 |
| Cooling | Pump | 1,2 |
| Energy | Generator Ph A,B,C | 2 |

### 5.3.3 Selection of Test and Train, Validation data

Given the 100 run to failure profiles defined in Chapter 4, and desired signals defined in the previous subsection, test and train datasets were constructed to serve as input data to explore prediction algorithms and accuracy through the prediction framework. The partitioning of test, train and validation data was done by the individual RTF profiles and their respective indices 1-100.

Given the limitation on dataset size, due to the time intensive process of collecting real hardware run to failure profile data, a resampling process was necessary and implemented to help reduce over fitting. The resampling process selected test, train and validation data 50 times, producing 50 varying selections of the 100 RTF profiles for the selection of test train and validation data. The first 20 samples are applied for the individual system level diagnostic and prognostic task and the full 50 samples are used for the final plant level framework.

Three test and train datasets were constructed with variation is percentage of validation, test and train data. The varied allocations for test, train and validation data for each of the three datasets are defined below in Table 5.7.

Table 5.7: Partitions of Test, Train and Validation Data

| **Partition** | **Train** | **Validation** | **Test** |
|---|---|---|---|
| Partition A | 0.8 | 0.1 | 0.1 |
| Partition B | 0.6 | 0.2 | 0.2 |
| Partition C | 0.8 | 0.15 | 0.15 |

The variations in test, train and validation provide selection options dependent on the required data allocations for a potential AI model. Partition A will serve as the primary

partition with partition B-C reserved for future work if required.

In summary, for each of the three unique partitions of test, train and validation data, the selection of test, train and validation data was repeated 50 times to produce 50 varying selections of the 100 failure runs for the selection of test train and validation data. Training set 1 served as the base selection and training set 2 and 3 were constructed in the event selected algorithms would required a larger set of validation and test data.

### 5.3.4 Summary of Input Data

Leveraging the RTF data defined in Chapter 4, 50 signals were extracted across the two sub-portions of the MLSMP (plant 1 and plant 2).The following data indices were formed to allow selection of input data for plant level predictions.

Table 5.8: RTF Dataset Indices

| **Parameter** | **Range** |
|---|---|
| Prediction sequence-point | 4-6 |
| Plant | 1 - 2 |
| Operational Profile | 1-3 |
| Avg. Value Signal Options | 1-3 |
| Cooling Diagnostic Data | 0-1 |
| Power Spectrum Data | 0-2 |
| Partition (test,train,val) | 1-3 |
| RTF Profiles | W or W/O Leaks |

The Prediction sequence-point represents how many sequence-points of input data is used for diagnostic and prognostics. The selection of plant determines data and response information is selected from plant 1 or plant 2. The operational profile corresponds to the three variations in system loading defined further in Chapter 4. The Avg. value signal options determine which of the three average value signal data groups was used for input data, as defined in Table 5.3. The selection of cooling diagnostic data determines if data from the chosen operational profile (A,B or C) is used, selection of index 0, or data from all three operational profiles is used, selection of index 1. The selection of partition (test,train,val) 1 is used as the default selection for the division of test, train, and validation data percentages. Partition values 1 and 2 are reserved in the event larger portions of train and validation data are required by a given AI algorithm. Power Spectrum Data values of 0-3 correspond to varying groups of input data in 1-3 and a value of 0 excludes all power spectrum data from

use as an input. Finally, RTF Profiles can be selected to include all 100 profiles or only profiles without leaks.

## 5.4 Initial Signal Evaluation

### 5.4.1 Overview

Using the formed dataset from Section 5.3, data was first analyzed for its initial applicability for the diagnosis of leaks and forecasting of plant level operational availability. This preliminary analysis served as a baseline for signal exploration to provided an initial set of input parameters to evaluate potential AI based algorithms in the subsequent Sections of this Chapter. The analysis was limited to two metrics and is not exhaustive, however all potential input signals were reviewed for their potential applicability in leak detection and failure prediction. This analysis focused on two metrics for each signal of interest. The two metrics are defined as follows:

- Metric 1 (Leak Detection): The change in each signal value between each sequence-point for sequence-points 1-5 was computed across all 100 RTF profiles and operational profiles (A-C). The minimum and maximum value for each instance was recorded in conjunction with the class label (Leak / No Leak) for the given RTF profile.
- Metric 2 (Prognostics): The difference in signal value between sequence-point 1 and sequence-point 5 was computed across the 100 RTF profiles not containing leaks and their respective operational profiles (A-C). The value and the corresponding failure sequence-point for the given RTF profile and operational profile was recorded as an entry alongside the numerical value for each signal.

Figure 5.5 and Figure 5.6 showcase the simplistic process used to evaluate signals for their initial potential as predictors for both leak detection and failure sequence-point forecasting. This process was repeated for all indexed signals in the constructed dataset defined in Section 5.3. Both Figure 5.5 and Figure 5.6 use data from plant 2 and operational profile C to compare signal viability for the average value signal of cooling pump current and the power spectrum (5th Harmonic) data for the corresponding pump. Figure 5.5 illustrates signal viability for cooling system leak diagnosis and Figure 5.6 illustrates signal viability for failure sequence-point prediction.

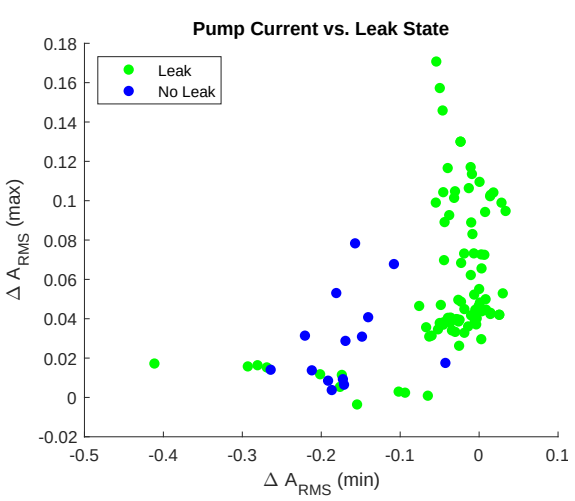


(a) Avg. Current Data

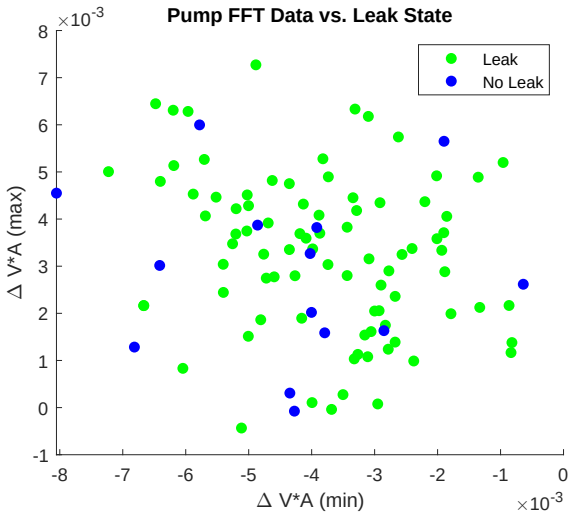


(b) Power Spectrum (5th Harmonic) Data

Figure 5.5: Example Signal Analysis for Diagnostic Predictor Evaluation (Cooling System, Plant 2 and Operational Profile C)

As depicted in Figure 5.5a a clear correlation exists between the cooling system leak state (leak vs. no leak) and the minimum and maximum change in average value pump current between each sequence-point for the cooling system in plant 2 on operational profile c. This relationship was formed using analysis Metric 1 and provides initial promise that changes in sequence data for pump current is a strong predictor of leak state.

The process was followed to analyze the extracted (5th Harmonic) power spectrum data from the line current and voltage for the cooling system pump in plant 2 on operational profile C. The result is depicted in Figure 5.5b and illustrates weak to no correlation between leak state and changes in sequence data for extracted (5th Harmonic) power spectrum data.

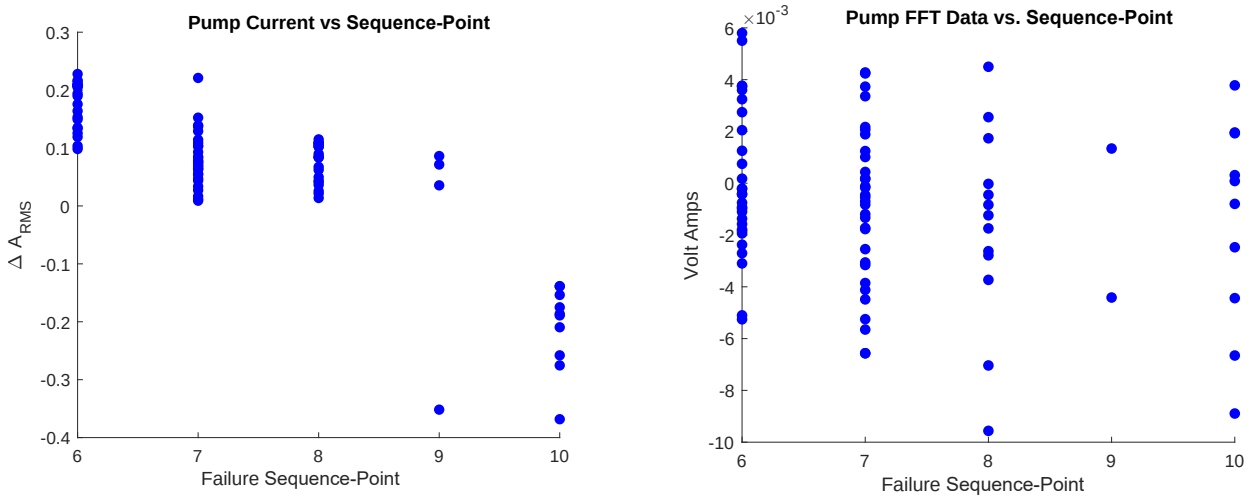


(a) Avg. Current Data

(b) Power Spectrum (5th Harmonic) Data

Figure 5.6: Example Signal Analysis for Prognostic Predictor Evaluation (Cooling system, Plant 2 and Operational Profile C)

Figure 5.6 provides the visual correlation between average value pump current and (5th Harmonic) power spectrum data and their respective change in value between sequence-point 1 and sequence-point 5 and its' correlation to cooling system failure sequence-point for operational profile C on plant 2. Figure 5.6a depicts a potential correlation between change in average value pump current from sequence-point 1 to sequence-point 5 and failure sequence-point. However, Figure 5.6a shows little to no correlation between the 5th Harmonic power spectrum data and the cooling system failure.

A second example of the simplistic evaluation process for the FFT pump data is shown below in Figure 5.7 and Figure 5.8. In both these figures, power spectrum data from the line current and voltage for the cooling system pump in plant 2 on operational profile C was used. The two subplots for the following two figures analyze the first and third harmonics. Figure 5.7 illustrates this analysis for leak detection and Figure 5.8 illustrates this process for prediction sequence-point.

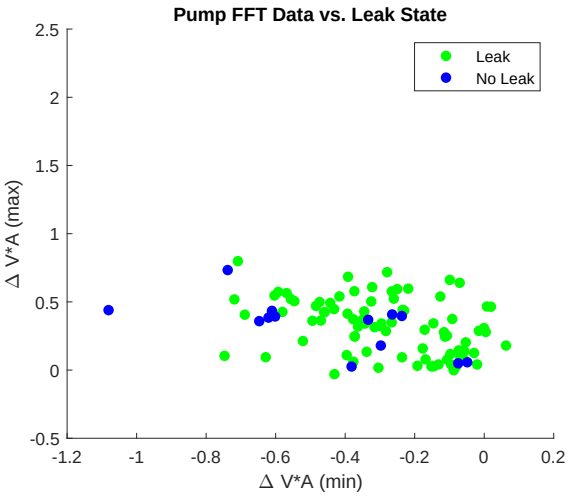


(a) Power Spectrum (1st Harmonic) Data

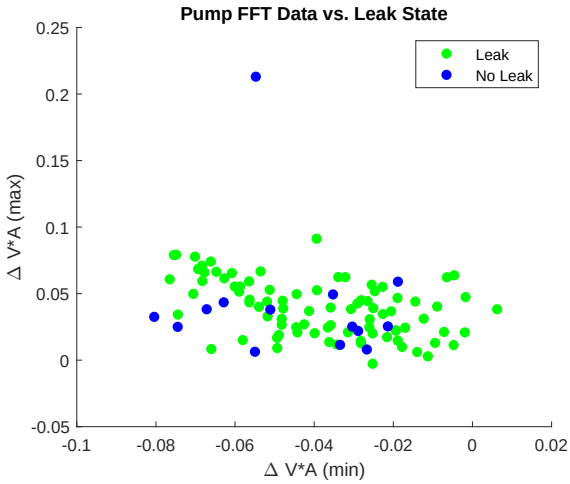


(b) Power Spectrum (3rd Harmonic) Data

Figure 5.7: Example Signal Analysis for Diagnostic Predictor Evaluation (Cooling System, Plant 2 and Operational Profile C)

As shown in Figure 5.8a a grouping pattern appears for the first harmonic with respect to the leak no leak classification. However this pattern is not as strong of a correlation as was depicted in Figure 5.5a. The third harmonic shown in Figure 5.7b shows a reduced correlation with respect to the first, but slightly tighter than the 5th harmonic.

Following this process Figure 5.8 reviews the potential of the first and third harmonic for failure sequence-point prediciton.

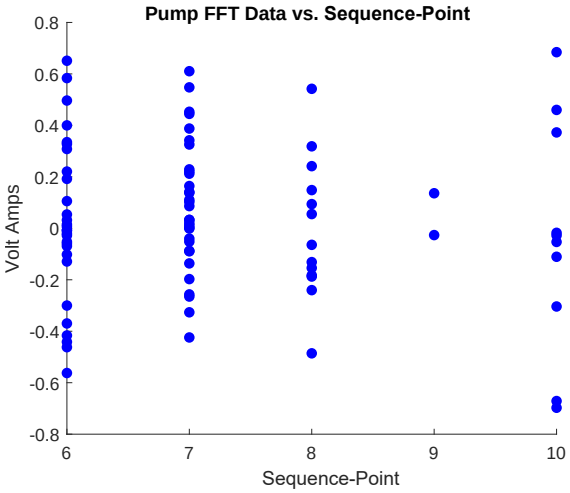


(a) Power Spectrum (1st Harmonic) Data

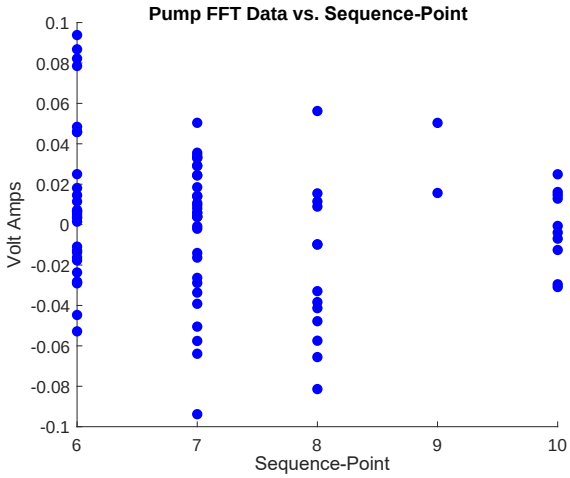


(b) Power Spectrum (3th Harmonic) Data

Figure 5.8: Example Signal Analysis for Prognostic Predictor Evaluation (Cooling system, Plant 2 and Operational Profile C)

As depicted in Figure 5.8 the two plots show little to no correlation between failure sequence-point and the 1st and third harmonics. The two metrics were applied across all potential signals to visually determine their applicability for the diagnostic and prognostic tasks. The following Subsection provides a summary of the correlations between signals and future and current plant state.

### 5.4.2 Summary

Leveraging the simplistic analysis method defined and showcased in the previous subsection. The two methods were applied to all indexed signals within the formed dataset. A simple visual inspection was used to select and rank predictor signals. These efforts were necessary due to the large state space of possible combinations for input signals and parameters. The down selection of signals enabled a feasible starting point to evaluate AI algorithms, with the selection of a long short-term memory (LSTM) Recurrent Neural Network (RNN), for leak detection and failure prediction. The key findings are summarized as follows and are grouped by index parameters redefined in Table 5.9:

- (Operational Profile (A-C) and Plant (1 or 2)): Little to no variation in signal correlation as a predictor of failure sequence-point or diagnoses of leak state was found between a singular signal across operational profiles (A-C) and between the two plants (plant 1 and plant 2). Given the uniformity between the two plants, and operational profiles (A-C) with respect to an individual signals correlation to current or future state of health, the variation of signal correlation between the possible input signals can be jointly summarized for both plants and all operational profiles.

- Power Spectrum Data: Little to no correlation was found between any harmonic amplitude or component data was extracted from and the current state for the cooling and fuel systems or the failure sequence-point for the fuel and cooling systems. This initial analysis removed the power spectrum data from initial consideration as input for leak detection or the prediction of fuel or cooling system failures.

- Average Value Data: A strong correlation was found between the average value signals and the current state for the cooling and fuel systems as well as the failure sequence-point for the fuel and cooling systems. This initial analysis placed a high consideration on varied combination of average value data as input data.

The three core findings defined above successfully reduce the state space for possible input signal combinations to a manageable level with the remaining possible combinations

to evaluate within the AI based diagnostic and prognostics framework listed below in Table 5.9.

Table 5.9: Data Indices - Initial Selection and Evaluation Range

| **Parameter** | **Initial Selection** | **Range** |
|---|---|---|
| Prediction sequence-point | 5 | 4-6 |
| Plant | 2 | 1-2 |
| Operational profile | 3 | 1-3 |
| Cooling diagnostic data | 1 | 1-2 |
| Avg. value signals option | 3 | 1-3 |
| Partition (test,train,val) | 1 | 1 |
| RTF Profiles | W & W/O Leaks | W & W/O Leaks |

Table 5.9 removes the power spectrum data from consideration for input data for work in this chapter given the low correlation between the extracted harmonic points and system failure sequence-point as well as leak status for the cooling and fuel systems. Provided the minimal variation in correlation for a signal across operational profile (A-C), and plant (1 and 2) a fixed set of inputs was formed to explore varying AI based diagnostic and prognostic algorithms, the selection of these parameters is listed in Table 5.9 under the column titled "Initial Selection". The parameter values listed in rightmost column titled "Range" represent the full bandwidth of signal combinations that will be reintegrated after the selection of a detection and prediction Algorithm to compare the effects on diagnostic and prognostic accuracy.

## 5.5 System Level Diagnostics

### 5.5.1 Overview

Prior to the prediction of plant level capability it was critical to evaluate the current state of health for the plant. Using the RTF dataset leveraged in this chapter, the current state for the machinery plant contained a probability of a critical failure (leak) in the fuel and cooling system. The injection of a leaks in the cooling or fuel system was independent to one another with a randomly distributed probability of occurrence between sequence-point 2-4 of a given RTF profile. Data from sequence-point 1 to sequence-point (4-6) will be used as input data to evaluate common AI algorithms for the detection of a leak in the cooling and fuel systems. Throughout this section leak detection and the application of potential

AI algorithms is done independently for both the cooling and fuel systems but identical algorithms are considered for each system. The first subsection of this chapter proposes and selects a potential AI algorithm building from initial work completed in Chapter 3. An LSTM based model is chosen in Subsection 5.5.2 as a potential algorithms for the diagnostics task. Initial feasibility of the LSTM model is confirmed in Subsection 5.5.3. The following two Subsections 5.5.4-5.5.5 provide an exploration of varied input signals and the respective diagnostic performance for the cooling and fuel system respectively. The final subsection provides a summary of the key takeaways for system level diagnostics.

### 5.5.2 Algorithm Selection

Building from work completed in Chapter 3, common classification methods were first considered for the diagnostic task in the plant prediction framework. The considered classifiers included: K-Nearest Neighbors (KNN), Decision Tree, Logistic Regression, and Support Vector Machines. Initial efforts revealed little potential and many challenges for the use of common classifiers in the diagnostic task. A critical shortcoming of common classification method was the inability to receive sequence based data as input. Feature extraction was attempted to circumvent this limitation, however these methods were unable to extract the hidden correlations between profile to profile signal variation and variations in signals due to changes of system state (no leak to leak). These challenges served as motivation to apply an AI algorithm with the ability to receive sequence based input data to diagnose if a leak was present or not for the fuel and cooling systems.

A long short-term memory (LSTM) neural network was selected and configured for this task based on the algorithms prevalence in diagnostic applications from literature using time series based input data. These applications used to perform diagnostic tasks include: Abnormality detection in nuclear power plants [50]-[51], Bearing fault diagnosis [52], unmanned aerial vehicle (UAV) actuator failures [53], and high impedance faults in solar Photovoltaic integrated power systems [54].

Data from sequence-points 1 to (4-6) for each RTF profile was used as the input predictor time series data to provide the prediction response of whether or not a leak was present in the given profile. The LSTM model was provided a numerical value of 0 or 1 for the response value of each profile in the training dataset. The numerical value of 0 was used to define a profile without a leak and the value of 1 was used to defined a profile with a leak. The LSTM model parameters and configuration for the diagnostic task are defined below in Table 5.10.

Table 5.10: LSTM Model Parameters for Diagnostics

| **Parameter** | **Value** |
|---|---|
| Normalization | Zscore |
| Hidden Units | 200 |
| Output Mode | Last |
| Fully Connected Layers | 1 |
| Max Epochs | 500 |
| Validation Data | 10 % |
| Output Network | best-validation-loss |
| Initial Learn Rate | 0.005 |
| Sequence Length | shortest |
| Verbose | false |

Using the selected and defined LSTM model, a preliminary evaluation of its feasibility for the diagnosis of system leaks is provided in the following Subsection.

### 5.5.3 LSTM Model - Initial Evaluation

Expanding work from Chapter 3 exposed clear limitations of traditional classification methods for state detection provided the input of sequence based data. An LSTM based algorithm was used to attempt to improve the ability to detected the current state (leak no leak) for the fuel and cooling system. A key benefit of this approach is the ability to take sequence based input data and provide a response of an integer value correlated to a leak or no leak state. To determine initial feasibility the initial initial indices for parameters defined in Table 5.9 are used.

Provided the defined input data for the fuel and cooling system predictions an LSTM model was applied to diagnose the current state of the cooling and fuel systems independently. The LSTM output produced a single value, where a value of 1 represents a leak and a value of 0 represents no leak. Of the 100 RTF profiles, the model for this test used 80 % of the profiles to train, 10 % for validation and 10 % for testing. The LSTM train, validation and test process was repeated 20 times with random selections of test, train and validation indices to provide a more accurate indication of true prediction performance given the small dataset. The LSTM results for the test predictions are depicted in Figure 5.9a for the fuel system and Figure 5.9b for the cooling system.

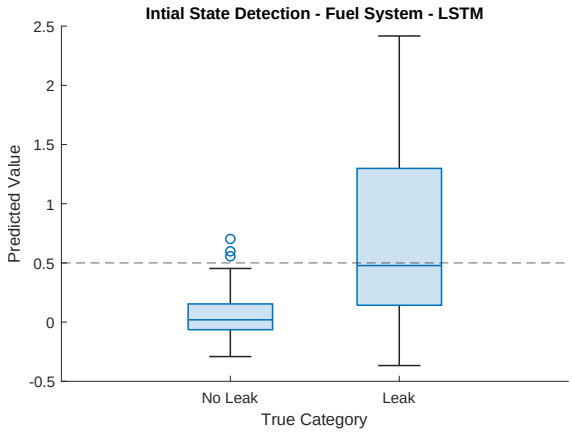


(a) Fuel System

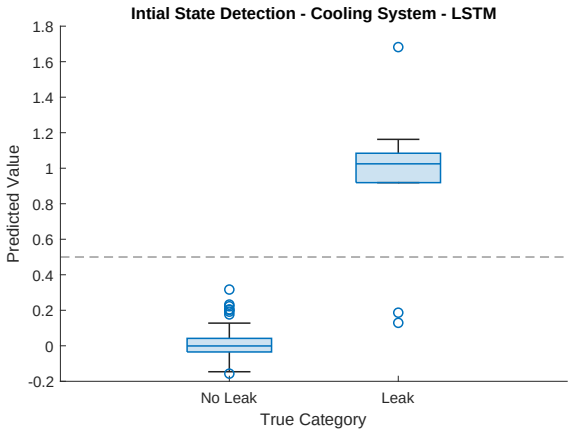


(b) Cooling system

Figure 5.9: System Diagnostics - Initial Results

A decision threshold of 0.5 was set to determine the class of leak or no leak based on the prediction value. The threshold was chosen as an even division between the true state of leak represented as an integer 1 and a true state of no leak represented as an integer 0. The 0.5 threshold was adopted for classifying the predicted state of leak or no leak, where a value greater than 0.5 was a prediction of a leak and a value less than 0.5 was classified as no leak. The initial prediction accuracy for the 0.5 cutoff threshold is defined below in Table 5.11.

Table 5.11: Initial Results for Leak Detection - LSTM

| System | Parameter | Error |
|---|---|---|
| **Cooling** | **Total Error** | **2** % |
| **Fuel** | **Total Error** | **15** % |
| Cooling | False Positive | 0 % |
| Cooling | False Negative | 2 % |
| Fuel | False Positive | 3 % |
| Fuel | False Negative | 15% |

As defined in Table 5.11 the LSTM model showed initial promise for cooling system and fuel system leak detection with initial results showing a minimal error of 2 % for the cooling system and an acceptable error of 15 % for the fuel system. The model and parameters used for these initial findings in this subsection are leveraged in the following subsection to evaluate diagnostic accuracy for a varying combinations of input data.

### 5.5.4 Cooling Leak Detection - LSTM Model Exploration

This Subsection expands the initial diagnostic work conducted in the prior subsection to consider detection accuracy for leaks in the cooling system with varied input signals, plant selections and operational profile selections. The evaluation ranges are defined below in Table 5.12.

Table 5.12: Input Data - Cooling System - LSTM Exploration for Leak Detection

| **Parameter** | **Value** |
|---|---|
| Prediction sequence-point | 4-6 |
| Plant | 1 & 2 |
| Operational Profile | 1-3 |
| Cooling diagnostic data | 1 and 2 |
| Avg. value signals option | 1-3 |
| Partition (test,train,val) | 1 |
| RTF Profiles | W Leaks |

The evaluation state space defined in Table 5.12 contains 72 unique combinations of model inputs, each evaluated combination is defined as a test. For the 72 tests total prediction error was calculated and compared across all tests. Across the 72 tests the maximum total error was 8.5 %. Across the 72 tests excluding cooling profiles leak data option 2, the use of average value data from all three operational profiles instead of a singular profile, decreased the maximum total prediction error to 5 %. The remaining 54 test cases and the correlation to input signal and diagnostic accuracy is summarized below in Table 5.13

Table 5.13: Results - Cooling System - LSTM Exploration for Leak Detection

| **Parameter** | **Value** | **Error** |
|---|---|---|
| Avg. Value Signals Options | 1 | 3.03% |
| Avg. Value Signals Options | 2 | **1.47**% |
| Avg. Value Signals Options | 3 | 2.36% |
| Prediction sequence-point | 4 | 2.80% |
| Prediction sequence-point | 5 | **1.92**% |
| Prediction sequence-point | 6 | 2.14% |
| Plant | 1 | **2.13**% |
| Plant | 2 | 2.45% |
| Operational Profile | 1 | 2.28% |
| Operational Profile | 2 | 2.45% |
| Operational Profile | 3 | **2.14**% |

The resultant diagnostic accuracy defined in Table 5.13 provides insight into the correlation between input parameters and diagnostic accuracy for cooling system leaks. The key trends are as follows:

- Avg. Value Signals Options: Option 2, the use of only pump current and pressure, provided the highest overall accuracy. Option 1, the use of all average value signals, had the lowest overall accuracy. With option 3, the use of only electrical current data providing the midpoint in diagnostic accuracy. These results show a strong correlation between electrical pump current and pressure and overall diagnostic accuracy. Providing the model additional information reduced diagnostic accuracy and only relying on pump current had a slightly worse performance than pump current and pressure.

- Prediction sequence-point: sequence-point 5 provided produced the least error, followed by sequence-point *6* then sequence-point 4. These results show information before and the sequence-point after the injection of a leak provide the best results and additional sequence-points after increase error.

- Plant: Little variation was found between the two plants with plant 1 having slightly less diagnostic error than plant 2.

- Operational Profile: Data from operational profile 3 provided the least error followed by operational profile 2, then 1.

The correlation between input parameters and diagnostic error shown in Table 5.13 align with the input variables shown across the 10 test cases with the least amount of prediction error shown in Table 5.14.

Table 5.14: Results - Cooling System - LSTM Exploration for Leak Detection (Top 10 cases)

| Sequence-Point | System | OP Profile | Signals | FP(%) | FN(%) | Total(%) |
|---|---|---|---|---|---|---|
| 5 | 1 | 3 | 2 | 0 | 0 | 0 |
| 5 | 1 | 1 | 2 | 0 | 0.5 | 0.5 |
| 6 | 1 | 1 | 2 | 0 | 0.5 | 0.5 |
| 5 | 2 | 3 | 2 | 0 | 1 | 1 |
| 5 | 2 | 2 | 2 | 0 | 1 | 1 |
| 5 | 1 | 2 | 2 | 0 | 1 | 1 |
| 6 | 1 | 3 | 2 | 0 | 1 | 1 |
| 6 | 1 | 3 | 1 | 0 | 1 | 1 |
| 5 | 2 | 1 | 2 | 0 | 1.5 | 1.5 |
| 5 | 1 | 3 | 1 | 0 | 1.5 | 1.5 |

The 52 test conducted confirmed the LSTM models ability to predict leaks within the cooling system for the RTF dataset and provided insight into correlations between chosen input parameters and leak detection accuracy.

The case with the largest error and least error are defined below in Table 5.15.

Table 5.15: Results - Cooling System - LSTM Exploration for Leak Detection (Best and worst case)

| Sequence-Point | System | OP Profile | Signals | FP (%) | FN (%) | Total (%) |
|---|---|---|---|---|---|---|
| 5 | 1 | 3 | 2 | 0 | 0 | 0 |
| 6 | 1 | All | 1 | 7.5 | 1 | 8.5 |

### 5.5.5 Fuel Leak Detection - LSTM Model Exploration

This subsection expands the initial diagnostic work conducted in Subsection 5.5.3 to consider detection accuracy for leaks in the fuel system with varied input signals, plant selections and operational profile selections. This subsection follows the same process as the previous subsection followed to evaluate detection accuracy in the cooling system. The evaluation ranges are defined below in Table 5.16.

Table 5.16: Input Data - Fuel System - LSTM Exploration for Leak Detection

| **Parameter** | **Value** |
|---|---|
| Prediction sequence-point | 4-6 |
| Plant | 1 & 2 |
| Average Value Signals Options | 1-3 |

The evaluation state space defined in Table 5.16 contains 18 unique combinations of model inputs, each evaluated combination is defined as a test. For the 18 tests total prediction error was calculated and compared across all tests. The prediction results for the 18 test cases and the correlation of input parameter selection to diagnostic accuracy is summarized below in Table 5.17

Table 5.17: Results - Fuel System - LSTM Exploration for Leak Detection

| **Parameter** | **Value** | **Error** |
|---|---|---|
| Average Value Signals Options | 1 | **6.75**% |
| Average Value Signals Options | 2 | 7.33% |
| Average Value Signals Options | 3 | 10.88% |
| Prediction sequence-point | 4 | 9.17% |
| Prediction sequence-point | 5 | 8.08% |
| Prediction sequence-point | 6 | **7.67**% |
| Plant | 1 | **8.17**% |
| Plant | 2 | 8.45% |

The resultant diagnostic accuracy defined in Table 5.13 provides insight into the correlation between input parameters and diagnostic accuracy for fuel system leaks. The key trends are as follows:

- Avg. Value Signals Options: Option 1, the use of all average value signals, had the lowest overall error followed by option 2 then 3. Providing a clear trend that the reduction in input data signals reduced increased overall error.
- Prediction sequence-point: sequence-point 6 provided produced the least error, followed by sequence-point *5* then sequence-point 4 providing evidence that an increase in input data improved results.
- Plant: Little variation was found between the two plants with plant 1 having slightly less diagnostic error than plant 2.

The correlation between input variables and diagnostic error shown in Table 5.17 align with the input variables shown across the 10 test cases with the least amount of prediction error shown in Table 5.18.

Table 5.18: Results - Fuel System - LSTM Exploration for Leak Detection (Top 10 cases)

| **Sequence-Point** | **System** | **Signals** | **Fuel FP(%)** | **Fuel FN(%)** | **Fuel Total(%)** |
|---|---|---|---|---|---|
| 5 | 2 | 1 | 1 | 3.5 | 4.5 |
| 5 | 2 | 2 | 1.5 | 4.5 | 6 |
| 6 | 1 | 1 | 2 | 4 | 6 |
| 6 | 2 | 1 | 2 | 4.5 | 6.5 |
| 6 | 1 | 2 | 2 | 4.5 | 6.5 |
| 5 | 1 | 1 | 2.5 | 4.5 | 7 |
| 5 | 1 | 2 | 2 | 5.5 | 7.5 |
| 6 | 2 | 2 | 2 | 5.5 | 7.5 |
| 4 | 2 | 1 | 1 | 6.5 | 7.5 |
| 4 | 1 | 2 | 1.5 | 6 | 7.5 |

The 18 tests conducted confirmed the LSTM models ability to predict leaks within the fuel system for the RTF dataset and provided insight into correlations between chosen input parameters and leak detection accuracy.

The case with the largest error and least error are defined below in Table 5.19.

Table 5.19: Results - Fuel System - LSTM Exploration for Leak Detection (Best and worst case)

| **Sequence-Point** | **System** | **Signals** | **Fuel FP (%)** | **Fuel FN (%)** | **Fuel Total (%)** |
|---|---|---|---|---|---|
| 5 | 2 | 1 | 1 | 3.5 | 4.5 |
| 5 | 2 | 3 | 1.5 | 13.5 | 15 |

Table 5.19 illustrates that as the complexity of the system increases the selection of input parameters plays a more critical role in the accuracy of the models response. This analysis is formed from the increased in change in error between the best and worst cases for the simpler cooling system to the more complex fuel system. Where the complexity is driven by the increase from 1 to 2 flow paths between the cooling and fuel systems.

### 5.5.6 Summary

An LSTM based approach to diagnose the current state of leak or no leak for the cooling and fuel systems had less than a 10 % classification error for each individual system with respect to their best performing input parameters. The LSTMs ability to use sequence input data provided an improvement in prediction accuracy for the cooling and fuel system diagnostic process.

## 5.6 System Level Prognostics

### 5.6.1 Overview

Machinery plant state of health experiences constant degradation in time with repair to improve the system state of health both as preventative maintenance or corrective maintenance as a result of failure. Provided the notional machinery plant used throughout this chapter is not in a current failed state of health, determined through diagnostic work completed in the previous section, and has some unknown degradation to system health which at the current time has no effect on system performance, it is desired to predict the duration until operational performance is effected. Provided an unknown and degrading state of clogging for the cooling and fuel system it is desired to predict the failure sequence-point for each of the three defined operational profiles, or the sequence-point the fuel and or cooling system has insufficient capacity to support a given operational profile. Data from sequence-point 1 to sequence-point (4-6) will be used as input data to evaluate common AI algorithms and their ability to predict system operational availability in time. This prediction of machinery plant state of health in this section is done independently for the cooling and fuel systems.

The following Subsections in this Section follow a similar process to the past Section. The first Subsection proposes and selects a potential AI algorithm building from initial work completed in Chapter 3. An LSTM based classifier is chosen in Subsection 5.5.2 as a potential algorithms for the prognostic task. Initial feasibility of the LSTM model is confirmed in Subsection 5.5.3. The following two Subsections 5.5.4-5.5.5 provide an exploration of varied input signals and the respective prognostic performance for the cooling and fuel system respectively. The final Subsection provides a summary of the key takeaways for system level prognostics.

### 5.6.2 Algorithm Selection

Initial prognostic work attempted to build from work completed in Chapter 3. These initial efforts attempted to use input data from sequence-points 1-5, to forecast the future values of signals within the machinery plant that directly represent system health such as cooling system heat rise and fuel system rail pressure. First an LSTM based model was used to predict cooling system heat rise in one application and fuel system rail pressure in a second application. However, these initial studies found that the LSTM model forecast capability sharply degraded after the first sequence-point and little transfer of knowledge between signal trends in one signal transferred to the future response of another signal. Trends in cooling pump current had little effect on future changes in heat rise. These findings provided insight that either the prediction method or process of inputs and outputs was not optimal or the LSTM model did not fit the prediction method. To follow on, using the same input and output data process, and following [55] a CNN was considered and evaluated in using the same process. The CNN model results also provided little transfer of knowledge between signal trends in one signal transferred to the future response of another signal. These two unsuccessful applications of prognostics served as motivation to attempt a prediction process.

Provided the success of an LSTM model to diagnose the status of leak or no leak for the fuel and cooling system, this model was evaluated for its potential in system prognostics. The LSTM model used for leak detection is a variant of the past LSTM model attempted. The new LSTM model leveraged input data from sequence-points 1-5, and instead of attempting to predict a given signal as the response (i.e. cooling system heat rise or fuel system rail pressure) the model provided a response of failure sequence-point. LSTM model parameters are redefined below in Table 5.20.

Table 5.20: LSTM Model Parameters - Prognostics

| **Parameter** | **Value** |
|---|---|
| Normalization | Zscore |
| Hidden Units | 200 |
| Output Mode | Last |
| Fully Connected Layers | 1 |
| Max Epochs | 500 |
| Validation Data | 10 % |
| Output Network | best-validation-loss |
| Initial Learn Rate | 0.005 |
| Sequence Length | shortest |
| Verbose | false |

The following Subsection implements the proposed LSTM model for initial evaluation of the models ability to perform prognostics on the cooling and fuel system.

### 5.6.3 LSTM - Initial Evaluation

Using the defined model parameters in Table 5.20 and input data defined in Table 5.9 the LSTM model was implemented to predict the failure sequence-point of plant 2 in operational profile 3. For the 100 RTF profiles, the model for this test used 80 % of the profiles to train, 10 % for validation and 10 % for testing. The LSTM train, validation and test process was repeated 20 times with random selections of test, train and validation indices to provide a more accurate indication of true prediction performance given the small dataset. The LSTM results for the test predictions are depicted in Figure 5.10a for the cooling system and Figure 5.10b for the fuel system.

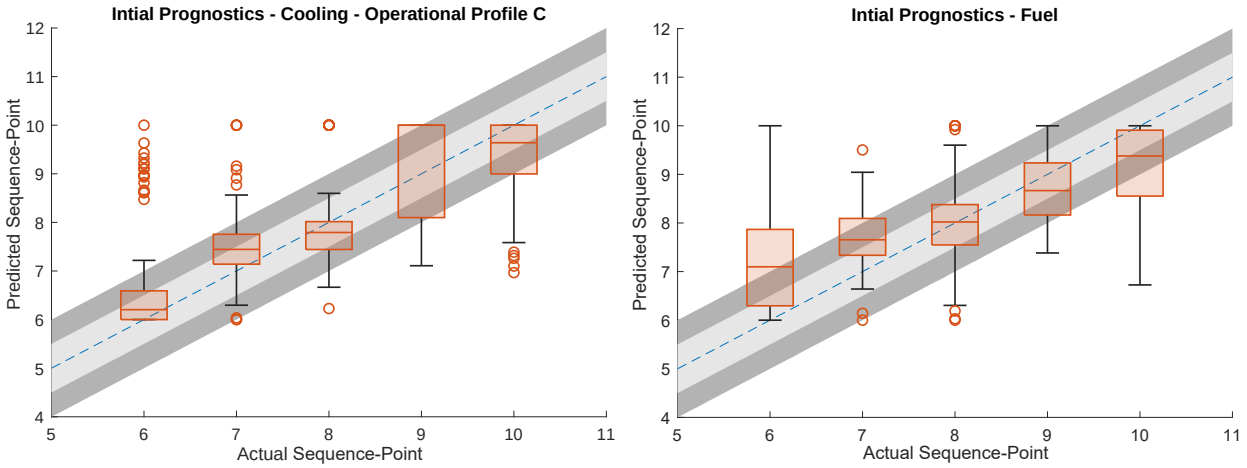


(a) Cooling System

(b) Fuel System

Figure 5.10: Initial Prognostic Results

As shown in Figure 5.10 the dotted blue line represents a perfect actual vs. predicted failure sequence-point, the surrounding light grey shared area on the graph provides a +- 0.5 sequence-point error band for the prediction results with respect to actual failure sequence-point. Similarly, the dark grey band represents a +- 1 sequence-point prediction error.

The visual results shown in Figure 5.10 are quantified by the respective system RMSE which was calculated across the 200 prediction and actual response values. The RMSE for the fuel system was 1.01 sequence-points and for the cooling system was 0.94 sequence-points. The RSME values and visual results for the initial test data confirmed the potential for an LSTM based system level prediction algorithm. The following two subsections provide a further exploration for the fuel and cooling system prognostic accuracy across the potential signal and parameter combinations.

### 5.6.4 Cooling Prediction - LSTM Model Exploration

Building from the initial LSTM test, this section evaluates a total of 54 input combinations exist for failure sequence-point prediction on the cooling system. The same model parameters, test-train-validation data partitions and iteration process is followed. The ranges of parameters evaluated are listed below in Table 5.21

Table 5.21: AI Prediction Input Data - Cooling

| **Parameter** | **Range** |
|---|---|
| Prediction sequence-point | 4-6 |
| Plant | 1-2 |
| Cooling Profiles Leak Data | - |
| Operational Profile | 1-3 |
| Average Value Signals Options | 1-3 |
| Power Spectrum Data | - |
| RTF Profiles | Without Leaks |

Using the input data combinations listed in Table 5.21 the RMSE value was computed for 200 test points in each of the 54 unique tests conducted. Using all 54 tests, the RMSE values were averaged across tests filtered by each parameter to provide insight into input parameter correlations to prediction accuracy. These values are provided below in Table 5.22.

Table 5.22: Cooling System Prognostic Results

| **Parameter** | **Value** | **RMSE (sequence-points)** |
|---|---|---|
| Average Value Signals Options | 1 | 0.51 |
| Average Value Signals Options | 2 | 0.66 |
| Average Value Signals Options | 3 | 0.87 |
| Prediction sequence-point | 4 | 0.73 |
| Prediction sequence-point | 5 | 0.70 |
| Prediction sequence-point | 6 | 0.61 |
| Plant | 1 | 0.69 |
| Plant | 2 | 0.67 |
| Operational Profile | 1 | 0.54 |
| Operational Profile | 2 | 0.82 |
| Operational Profile | 3 | 0.68 |

The RMSE values provided in Table 5.22 show clear correlations in prediction accuracy for all variables with exception to the selection of which plant was used. Plant 1 and plant 2 showed little variation in their prediction accuracy's. The trends for the remaining inputs are as follows:

- Avg. Value Signals Options: Option 1, the use of all average value signals, had the lowest overall error followed by option 2 then 3. Providing a clear trend that the reduction in input data signals reduced increased overall error.
- Prediction sequence-point: sequence-point 6 provided produced the least error, followed by sequence-point *5* then sequence-point 4 providing evidence that an increase in input data improved results.
- Operational Profile: Operational profile 1, followed by operational profile 3 then 2 produced the least prediction error. This order was in order of low to high plant loading.

These trends are confirmed through the input data found in the 10 (of 54) tests with the lowest RMSE values. The 10 lowest RMSE values and their corresponding input data parameters are defined below in Table 5.23.

Table 5.23: Results - Cooling System - LSTM Exploration for Prognostics

| **Sequence-Point** | **System** | **Profile** | **Signal** | **RMSE (sequence-points)** |
|---|---|---|---|---|
| 6 | 2 | 1 | 1 | 0.32 |
| 5 | 2 | 1 | 1 | 0.36 |
| 6 | 1 | 1 | 1 | 0.40 |
| 6 | 2 | 2 | 1 | 0.43 |
| 6 | 2 | 3 | 1 | 0.43 |
| 6 | 1 | 3 | 1 | 0.45 |
| 4 | 2 | 1 | 1 | 0.46 |
| 5 | 2 | 3 | 1 | 0.46 |
| 6 | 2 | 1 | 2 | 0.48 |
| 5 | 2 | 2 | 1 | 0.49 |

The lowest RMSE test case is shown visually in Figure 5.11a and depicts a tight grouping of data points within a +- 0.5 sequence-point band around the predicted value with respect to the actual value. The second subplot 5.11b, illustrates the prediction case with the largest error.

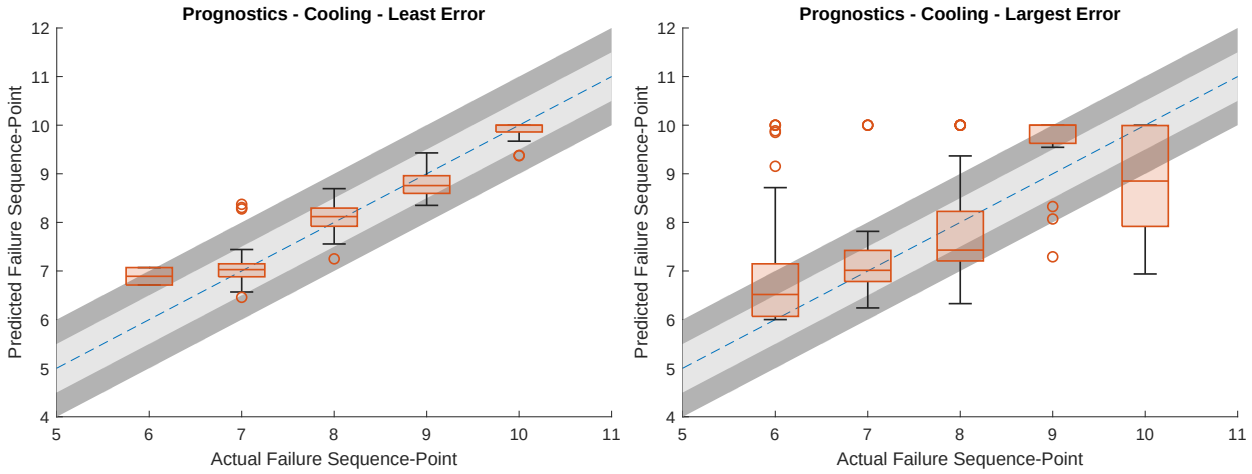


(a) Least Error

(b) Largest Error

Figure 5.11: Cooling System Failure Sequence-Point Prediction

As shown in Figure 5.11 the selection of input parameters is plays a critical role in the accuracy of the prediction model.

### 5.6.5 Fuel Prediction - LSTM Model Exploration

The process followed in the previous Subsection to evaluate the cooling system is repeated within this Subsection to evaluate the fuel system. A total of 18 input combinations exist for failure sequence-point prediction on the fuel system. The ranges of parameters evaluated are listed below in Table 5.24.

Table 5.24: AI Prediction Input Data - Cooling

| **Parameter** | **Range** |
|---|---|
| Prediction sequence-point | 4-6 |
| Plant | 1-2 |
| Cooling Profiles Leak Data | - |
| Operational Profile | - |
| Average Value Signals Options | 1-3 |
| Power Spectrum Data | - |
| RTF Profiles | Without Leaks |

Using the input data combinations listed in Table 5.24 the RMSE value was computed for 200 test points in each of the 18 unique tests conducted. Using all 18 tests, the RMSE values

were averaged across tests filtered by each parameter to provide insight into input parameter correlations to prediction accuracy. These values are provided below in Table 5.25.

Table 5.25: Results - Fuel System - LSTM Exploration for Prognostics

| **Parameter** | **Value** | **RMSE (sequence-points)** |
|---|---|---|
| Average Value Signals Options | 1 | 0.86 |
| Average Value Signals Options | 2 | 0.82 |
| Average Value Signals Options | 3 | 1.1 |
| Prediction sequence-point | 4 | 1.06 |
| Prediction sequence-point | 5 | 0.92 |
| Prediction sequence-point | 6 | 0.79 |
| Plant | 1 | 0.95 |
| Plant | 2 | 0.90 |

The RMSE values provided in Table 5.25 show clear correlations in prediction accuracy for all variables with exception to the selection of which plant was used. Plant 1 and plant 2 showed little variation in their prediction accuracy's. The trends for the remaining inputs are as follows:

- Avg. Value Signals Options: Option 1, the use of all average value signals, had the lowest overall error followed by option 2 then 3. Providing a clear trend that the reduction in input data signals reduced increased overall error.
- Prediction sequence-point: sequence-point 6 provided produced the least error, followed by sequence-point *5* then sequence-point 4 providing evidence that an increase in input data improved results.
- Plant: plant 2 had a lower error than plant 1.

These trends are confirmed through the input data found in the 10 (of 54) tests with the lowest RMSE values. The 10 lowest RMSE values and their corresponding input data parameters are defined below in Table 5.26.

Table 5.26: Results - Fuel System - LSTM Exploration for Prognostics

| **Sequence-Point** | **System** | **Signals** | **RMSE (sequence-points)** |
|---|---|---|---|
| 6 | 2 | 2 | 0.71 |
| 6 | 2 | 1 | 0.74 |
| 6 | 1 | 1 | 0.75 |
| 6 | 1 | 2 | 0.76 |
| 5 | 1 | 2 | 0.80 |
| 5 | 2 | 2 | 0.80 |
| 6 | 2 | 3 | 0.81 |
| 5 | 1 | 1 | 0.84 |
| 5 | 2 | 1 | 0.89 |
| 4 | 1 | 2 | 0.91 |

The lowest RMSE test case is shown visually in Figure 5.12a and depicts a tight grouping of data points within a +- 0.5 sequence-point band around the predicted value with respect to the actual value. Figure 5.12b depicts the parameter selection with the largest error.

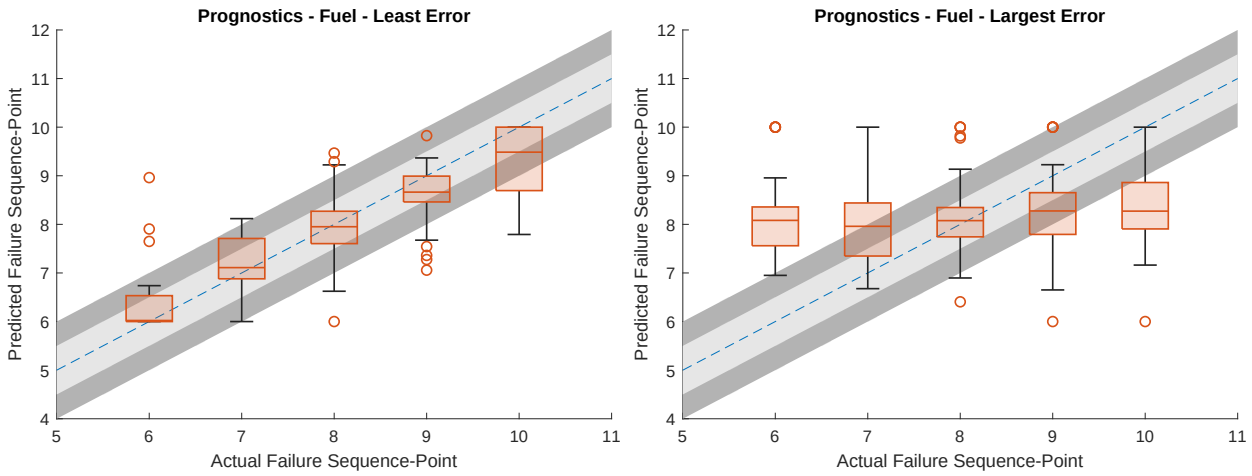


(a) Least Error

(b) Largest Error

Figure 5.12: Fuel System Failure sequence-point Prediction

As shown in Figure 5.12 the selection of input parameters is plays a critical role in the accuracy of the prediction model.

### 5.6.6 Summary

An LSTM based approach to predict the future sequence-point of failure for the cooling and fuel systems had less than a 1.10 RMSE value for each individual system, illustrating the LSTM model applicability for the prognostic task in this work. The selection of input parameters for both the cooling and fuel system models play a critical role in the accuracy of the model.

## 5.7 Plant Level Prediction

### 5.7.1 Overview of Prediction framework

The plant prediction framework leveraged the four individual LSTM based algorithms built in past Sections for leak detection within the fuel system, leak detection within the cooling system, fuel system failure prediction and cooling system prediction of cooling capacity in time. An overview of the plant framework is shown below in Figure 5.13.

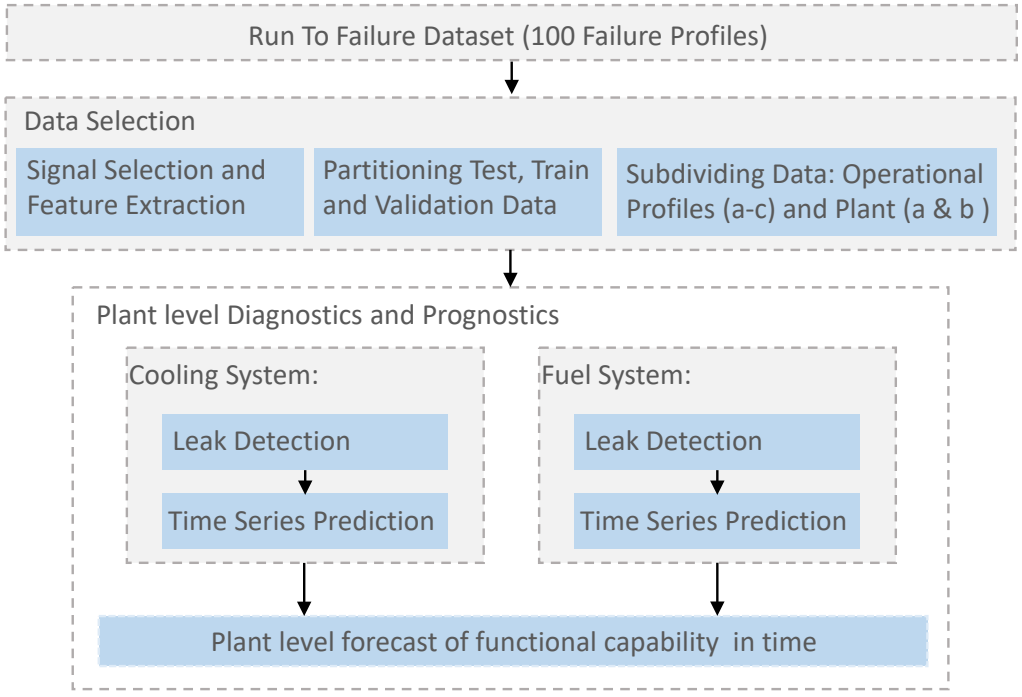


Figure 5.13: Overview - Prediction Framework

The multi-layer plant prediction framework depicted in Figure 5.13 used data without leaks in the train and validation categories to build the prediction LSTM models. The

diagnostic LSTM models were fed all train and validation in the training process. For the test process, all data points were fed into the Algorithms for leak detection. If a leak was detected for the cooling or fuel systems test profile was classified as a leak and considered failed. If a leak was not detected for the cooling or fuel systems test profile was classified as no leak and considered healthy. The healthy profiles were then passed to the cooling and fuel prediction algorithms where each LSTM model predicted its' respective systems failure sequence-point for the given inputs and the minimum of the two predictions was used as the output response.

### 5.7.2 Prediction Framework - Exploration

An initial test was performed to validate the feasibility of the grouped system level algorithms to perform plant level diagnostics and prognostics. The input data leveraged the initial indices defined Table 5.27 with model parameters remanding unchanged and listed for the fuel and cooling diagnostic LSTM model in Table 5.20 and parameters for the prognostic LSTM model listed in Table 5.10.

Table 5.27: Input Data - Plant Level Prognostics and Diagnostics

| **Parameter** | **Initial** | **Range** |
|---|---|---|
| Prediction sequence-point | 5 | 4-6 |
| Plant | 2 | 1-2 |
| Cooling Profiles Leak Data | 1 | 1 |
| Operational Profile | 3 | 1-3 |
| Average Value Signals Options | 3 | 1-3 |
| Power Spectrum Data | - | - |
| RTF Profiles | All | All |

Following a similar process used in the past Sections a 80 % of the profiles were used as training data, 10 % for validation and 10 % for testing. The LSTM train, validation and test process was repeated 50 times with random selections of test, train and validation indices to provide a more accurate indication of true prediction performance given the small dataset. The LSTM results for the initial test are shown below in Figure 5.14.

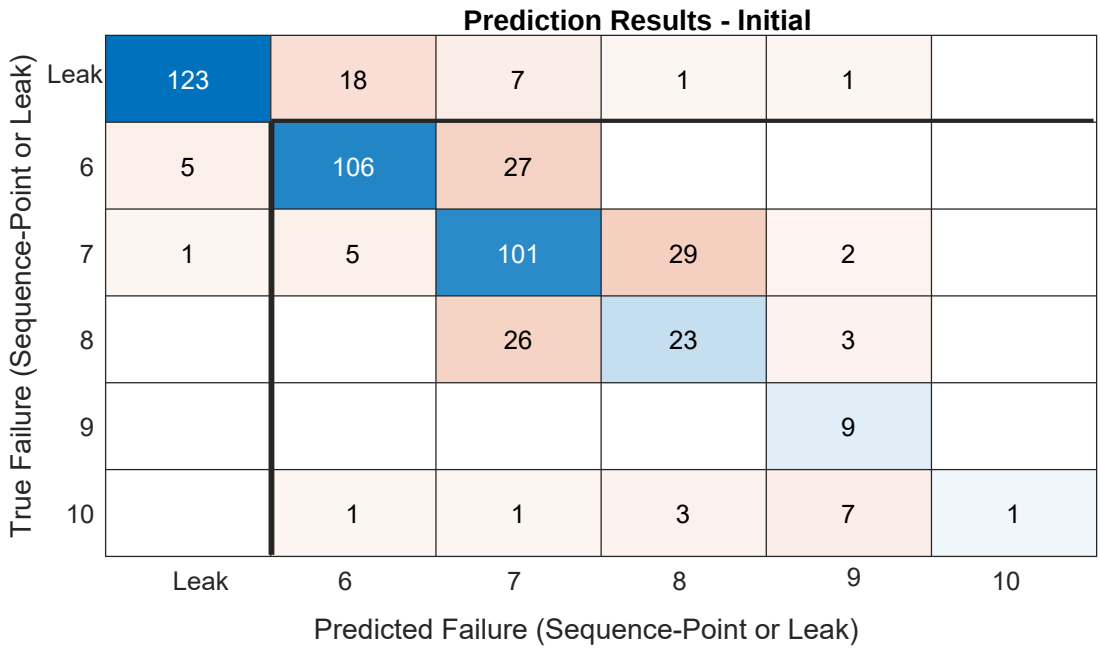


Figure 5.14: Plant Level Prediction - Initial Results

As depicted in Figure 5.14, test response data for the 50 iterations was divided into leak, no leak, and prediction sequence-point vs actual classes and placed in a confusion matrix for visual representation. A cutoff of +-0.5 was used place response data into the correct classes. The grid line in bold illustrates the division between leak classification for both systems and the prediction of failure sequence-point for both systems.

The process was repeated across the 54 possible combinations of input parameters listed in Table 5.10. The 54 input tests were first reviewed for low preforming predictors and excluded data from average value signals option 3. After removing average value signals option 3 the remaining parameters results were averaged across the test cases to evaluated diagnostic and prediction accuracy as shown in Table 5.28.

Table 5.28: Results - Plant Level Prognostics

| **Parameter** | **Value** | **Diagnostic Error(%)** | **Prognostic Error(RMSE)** |
|---|---|---|---|
| sequence-point | 4 | 9.87% | 0.91 |
| sequence-point | 5 | 7.93% | 0.70 |
| sequence-point | 6 | **7.35%** | **0.70** |
| System | 1 | **8.18%** | **0.74** |
| System | 2 | 8.59% | 0.79 |
| Operational Profile | 1 | **8.35%** | 0.78 |
| Operational Profile | 2 | 8.53% | **0.75** |
| Operational Profile | 3 | 8.27% | 0.79 |
| Avg. Value Signals Options | 1 | 8.49% | 0.79 |
| Avg. Value Signals Options | 2 | **8.28%** | **0.75** |

As defined in Table 5.28. The main driving factors in prediction error are as follows:

- Avg. Value Signals Options: Option 2 followed by Option 3 then Option 1 had the lowest error for both the diagnostic and prognostic tasks.
- Prediction sequence-point: Sequence-point 6 produced the least error, followed by sequence-point 5 then sequence-point 4 providing evidence that an increase in input data improved results.
- Operational Profile: Operational profile 1 had the lowest leak detection error, however operational profile 2 had the lowest overall prediction error.

The main driving factors are confirmed through the input parameters selected for the 10 best preforming tests and are listed below in Table 5.29.

Table 5.29: Results - Plant Level Prognostics

| **Sequence-Point** | **Plant** | **Profile** | **Signals** | **Diagnostic Error (%)** | **Prognostic RMSE (in sequence-points)** |
|---|---|---|---|---|---|
| 6 | 1 | 2 | 1 | 6.0% | 0.68 |
| 6 | 1 | 1 | 1 | 6.8% | 0.79 |
| 6 | 1 | 3 | 1 | 7.0% | 0.73 |
| 5 | 1 | 2 | 2 | 7.0% | 0.77 |
| 5 | 2 | 2 | 1 | 7.2% | 0.63 |
| 5 | 2 | 1 | 2 | 7.2% | 0.68 |
| 6 | 1 | 3 | 2 | 7.2% | 0.71 |
| 6 | 2 | 1 | 1 | 7.2% | 0.74 |
| 6 | 1 | 1 | 2 | 7.4% | 0.61 |
| 6 | 2 | 2 | 1 | 7.4% | 0.70 |

Over the 54 unique test cases, the plant level prediction tests with the minimum and maximum error are provided below in Table 5.30.

Table 5.30: Results - Plant Level Prognostics - Individual

| **Test** | **Sequence-Point** | **Plant** | **Profile** | **Signals** | **Diagnostic Error (%)** | **Prognostic RMSE (sequence-points)** |
|---|---|---|---|---|---|---|
| 22 | 6 | 1 | 2 | 1 | **6.0%** | 0.68 |
| 30 | 6 | 2 | 1 | 3 | 13.4% | **0.48** |
| 12 | 5 | 2 | 1 | 3 | *14.2%* | 0.62 |
| 47 | 4 | 2 | 1 | 2 | 10.4% | *1.09* |

The prediction values shown in bold in Table 5.30 represent the lowest error test for leak detection and prediction. The values shown in italicized represent the worst case for leak classification and prediction. The cases are illustrated visually in Figures 5.15-5.18.

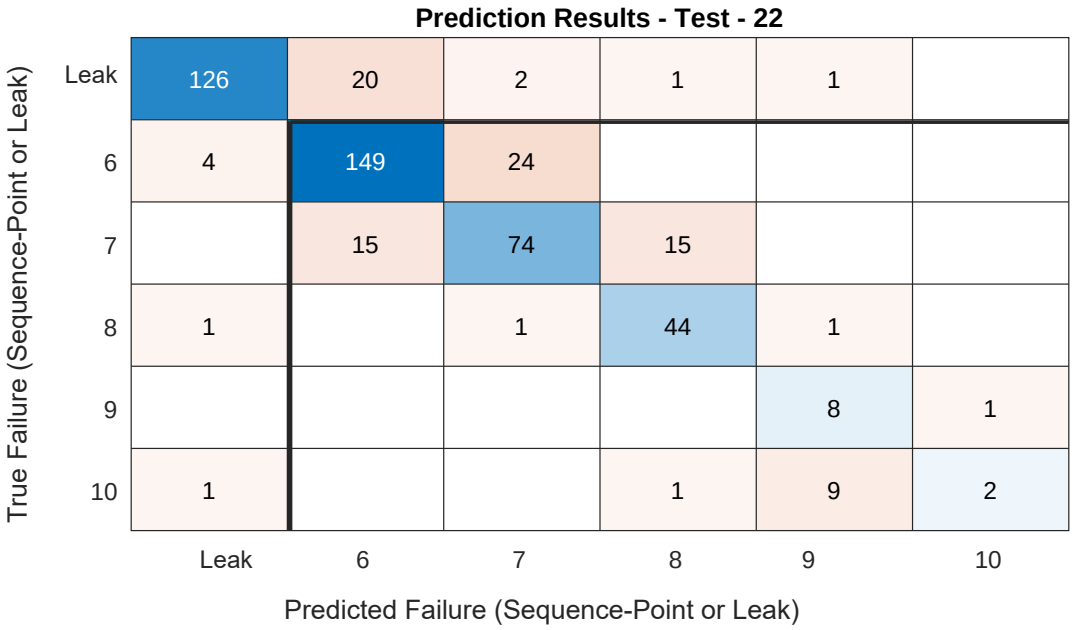


Figure 5.15: Plant Level Prediction - Results - Least Error (Leak,Predict)

Figure 5.15 depicts the results for input parameters which produced the least error for the diagnostic task at the plant level. The test case depicts a tight grouping for the prediction of a leak in the plant around the true state shown in the top left corner of the graph, where a leak is present in a support system and detected by the algorithm. Cases where a leak is not present and the prediction of no leak is provided are depicted by the values outside of the first row and column of the matrix. The error for the prediction of a leak within the plant when no leak is present is shown in the first column. The first row represents the prediction of no leak where a leak is present in the plant. The largest grouping for missed predictions is the prediction of sequence-point 6, when the system already has the presence of a fault (leak within the plant). These results illustrate a highly accurate prediction for the diagnostic task at the plant level with only 6 % overall error and the largest source of error caught by the prognostic task with a prediction of the following sequence-point being the failure point.

The following Figure 5.16, showcases input parameters that resulted in the largest error for the diagnostic task.

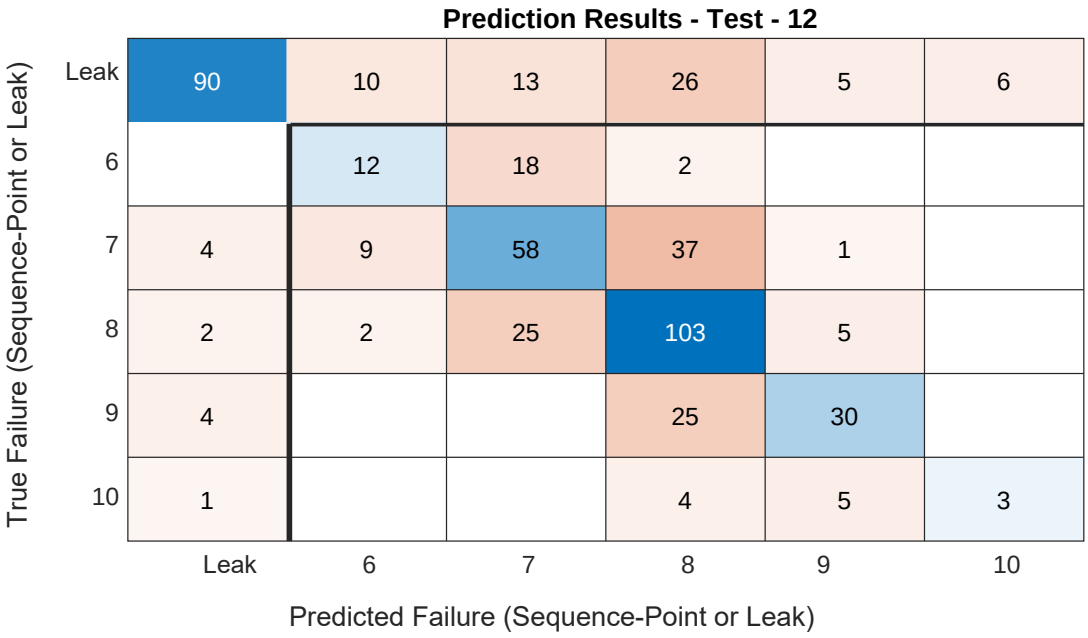


Figure 5.16: Plant Level Prediction - Results - Largest Error (Leak,Predict)

As shown in Figure 5.16, input parameters have a significant effect on overall accuracy for the diagnostic task and the distribution of error. The parameters which produced the largest error for the diagnostic task were also less effective at predicting the first sequence-point for cases when a diagnostic detection error was made.

Figure 5.17 depicts the results for input parameters which produced the least error for the prognostic task at the plant level.

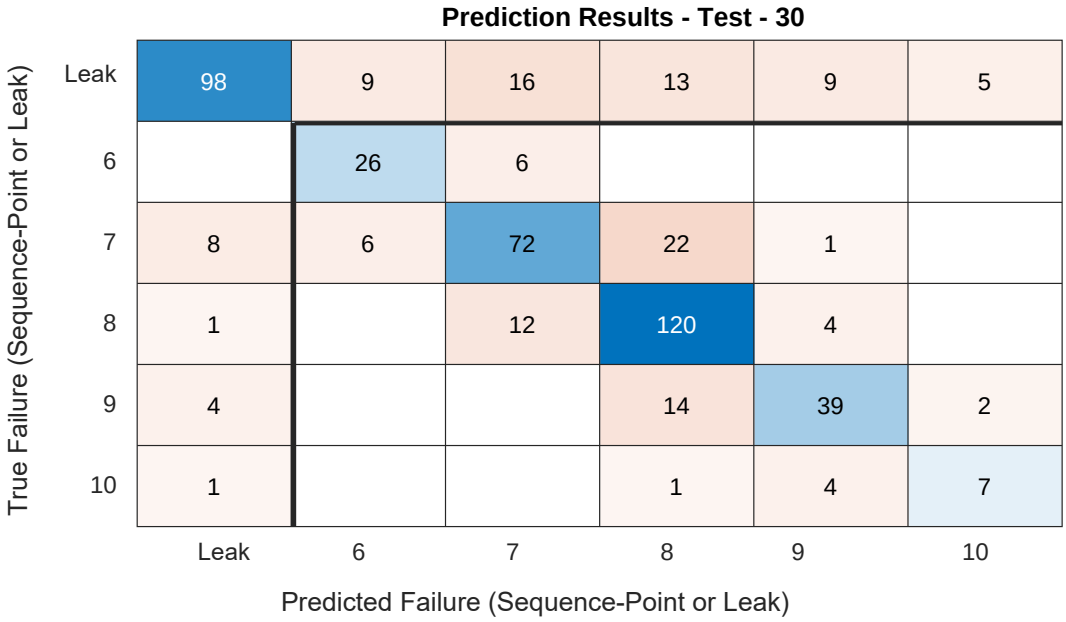


Figure 5.17: Plant Level Prediction - Results - Least Error (Predict,Leak)

As shown in Figure 5.17 the optimal input parameters for prediction at the plant level does not provide the highest accuracy for the diagnostic task. For the prognostic task, a tight grouping is shown across for the true prediction of sequence-point, illustrated in blue along the diagonal row and column set in the matrix. Prediction error is within a single sequence-point for 99.4 % of the total prediction points.

Figure 5.17 depicts the results for input parameters which produced the largest error for the prognostic task at the plant level.

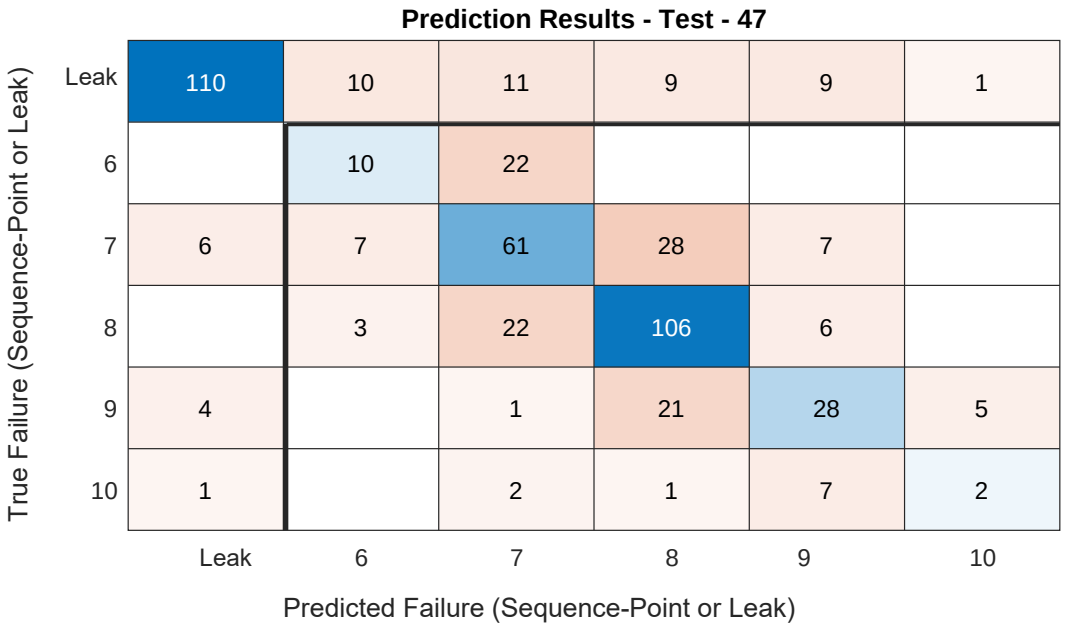


Figure 5.18: Plant Level Prediction - Results - Largest Error (Predict,Leak)

As shown in Figure 5.17 the input parameters that provided the least accurate prediction of failure sequence-point also produced a larger percent outside of a single sequence-point in prediction error, an increase from 0.6 % in the previous test case to 5 % of the prediction points in this test case. These results showcase the importance of parameter selection in the prognostics task.

### 5.7.3 Summary

The overall diagnostic and prognostic accuracy within the plant level prediction was heavily driven by the worst performing individual systems. At the plant level error was marginally 1 % larger on average than the worst performing system (fuel) for the diagnostic task. At the plant level the prognostic error was inline with that of the worst performing system (fuel) for the prognostic task.

The process illustrated throughout this section chose to follow the same evaluation process used in the past two sections in the evaluation of system level performance. Future work should include the evaluation of varied input parameters for each algorithm within the multi-layer framework to improve overall performance accuracy.

## 5.8 Conclusion

This chapter showcased the application of an LSTM driven AI framework for diagnostics, leak detection, and prognostics, failure sequence-point prediction, at the system and plant level.

In the diagnostic task initial attempts for leak detection highlighted the a critical shortcoming of common classification methods and their inability to receive sequence based data as input. This critical shortcoming was resolved through use of an LSTM based classification model. The diagnostic task also showcased that system complexity had a large effect on signal selection. The simpler cooling system performance was improved with less input signals as compared to the more complex fuel system, which preferred additional input signals for optimal performance. The fuel system also illustrated that with increase in system complexity leak detection error increased.

In the prognostic task for failure sequence-point prediction initial attempts highlighted the limitations of LSTM and CNN time series prediction models and their inability to correlate past values of several input signals with future values of the desired response signal in time such as fuel rail pressure. These limitations were resolved using a LSTM sequence to one model, which received sequence input data for several signals and provided a singular numerical value as the response. Using this process the LSTM sequence to one model effectively predicted failure sequence-point for the fuel and cooling systems. Similar to the trends found for leak detection between the cooling and fuel systems the cooling system outperformed the fuel system for prediction accuracy. Contrary to the leak detection process both the fuel and cooling prediction algorithms had the best performance leveraging all average value signals as inputs.

Using a multi-model framework the diagnostic and prognostic tasks were performed and provided a the response of a "failed" state where a leak is present or provided a the predicted sequence-point of failure. Using this multi-model approach the performance of the algorithm was heavily driven by the worst performing system, in this case the fuel system. The multi-model framework analysis also depicted a clear correlation between input parameters and plant level leak detection and prediction accuracy. The selection of input parameters varied for best performance in the diagnostic task as compared to the best performance for the prognostics task, providing insight signal selection plays a critical role in model accuracy.

The final multi-model prediction framework evaluated the applicability of LSTM models at the plant level and illustrated promising results. The two best performing models were able to detect faults within the plant with a 95 % accuracy rate and predict the failure sequence-point with a RMSE error of 0.48 sequence-points. These findings illustrate the

potential of a multi-model approach to perform diagnostics and prognostics on complex, and interdependent systems to provide an understanding of plant level health.

# CHAPTER 6

# Conclusion and Future Work

## 6.1 Summary

This PhD research evaluated the performance of common Artificial Intelligence (AI) models, with the selection of a long short-term memory (LSTM) Recurrent Neural Network (RNN), in diagnosing and prognosticating tasks on a notional laboratory scale ship machinery plant to diagnose potential failures within the plant and predict future operational capacity of the plant until failure. This work was done to evaluate the potential for AI based models to improve operational resilience in a fault prone environment. This work additionally showcases the potential for fault mitigation through real time control, provided knowledge of plant health, by providing examples of unconventional control methods for fault mitigation. This research aims to improve the shortcomings of unmanned and autonomous vessels and associated inabilities to maintain an operational machinery plant over long deployment periods in absence of human intervention onboard the vessels.

To complete the objective of this PhD it was required to design and construct a notional laboratory-scale ship machinery plant or MLSMP with the capability to injection common faults and failures that with increasing severity can cause the machinery plant to fail without causing physical damage to components within the MLSMP. This functionality was achieved through novel software-based system to system connections in conjunction with physical system to system linkages. The software-based linkages enable the injection of faults until failure, without physical damage to components. The software-based linkages also provide system to system interactions that would be present in an actual shipboard system but which are not possible in the lab scale environment. For example, at this small lab scale, water cooled equipment is not available whereas marine equipment is normally water cooled. This environment provided an ability to record repetitive run to failure profiles and explore the potential of control based fault mitigation techniques.

A group of three exemplary simulations using the MLSMP were designed and conducted

to showcase the ability to simulate and evaluate potential control based fault mitigation techniques using the MLSMP. The three simulations provide examples of unconventional control mitigation techniques to improve operational resilience in a fault prone and present environment.

A simple diagnostic and prognostic task was completed for a singular subsystem within the cooling system to confirm initial feasibility prior to plant level applications. This application explored the use of a long short-term memory (LSTM) recurrent neural network (RNN) to predict future temperature rise and common classification methods to detect the presence of system leaks. This initial study showcased the potential for AI driven methods,including the selected LSTM model, in the diagnostics and prognostics of machinery plant systems.

To explore the application of AI, including the selected LSTM model, for detection of common faults and prediction of future plant operational availability for the MLSMP, a large dataset with common run to failure profiles was modeled, acquired and archived. A software model of the MLSMP was constructed and integrated with a model of clogging from literature. The model simulated a distribution of clogs and leaks for the cooling and fuel systems, providing control points to repeat the distributed run to failure profiles in hardware. A dataset of 100 run to failure profiles (RTF) for the MLSMP was obtained by simulating the software control points on the hardware machinery plant through a real time automated control code.

The constructed dataset was used as input data to explore potential AI models,including the selected LSTM model, for the detection of individual system leaks and the prediction of when an individual system would fail to provide necessary functionality to support the required operational mission demands on the respective system. The applications of diagnostics and prognostics are used to form a multi-model diagnostic and prognostic prediction algorithm for the MLSMP. The formed plant level algorithm is tested and evaluated through the 100 RTF profiles to showcase the algorithms successes and prediction accuracy with respect to input parameter selection.

## 6.2 Contributions

The contributions of this work can be summarized into four primary groups. An overview of each of the four key groups and their specific contributions is provided below:

1. A laboratory scale ship machinery plant (MLSMP) was designed, constructed, and validated with the necessary physical and virtual system interconnections to accurately represent plant dynamics and common faults of machinery plants found on vessels in the real world. The plant consisted of a cooling system, fuel system, emulated diesel generator sets,

energy storage system, electrical system, mission system, propulsion system, and a real time control and data acquisition system. The lab based plant contains unique virtual linkages, in addition to physical system to system linkages, to enable injection of common faults and failures within the machinery plant. The injection of faults and failures into the physical hardware plant provided the novel ability to increase the severity of the desired faults until plant failure, without causing physical damage to the components or systems within the laboratory, thereby enabling the ability to collect repetitive run to failure datasets. The MLSMP provides a second capability to explore alternative fault mitigation techniques through real time system control.

2. A run to failure (RTF) dataset was modeled in software and simulated in hardware through an automated process to build an archive of 100 RTF profiles to serve as input data for the exploration of data-driven diagnostic and prognostic algorithms and their ability to detect common faults, system leaks, and to predict when the vessel machinery plant will be unable to support a given operational profile. The RTF model incorporated common faults and failures for the cooling and fuel systems, clogs and leaks, and leveraged an existing model of real world clogs from literature to build a software model which simulated the buildup of particles on filters in time for the cooling system and fuel high and low pressure systems.

3. A multi-model LSTM driven framework was developed and evaluated for the ability to perform prognostic and diagnostic tasks to determine the current state of health for the MLSMP and predict future plant operational availability over a deployment period, until failure. The novel multi-model LSTM driven framework, evaluated using failure data from the MLSMP, provides a step forward in improving operational resilience for unmanned and autonomous vessels in a laboratory environment. Additional contributions under this group are as follows:

- An initial application of AI, including common classifiers (decision trees, Logistic regression, naïve bayes classifiers, support vector machines, and nearest neighbor classifiers) and an LSTM time series prediction model, was applied to a subsystem within the cooling system and demonstrated the ability to detect a common cooling system fault (i.e., a leak) in the presence of an unknown system state of health caused by clogging. In addition, this work demonstrated an ability to leverage the response of the cooling system to a known change in loading, to predict the temperature rise at full load, and to provide knowledge of the system's capacity given a degraded state of system health.

- A critical shortcoming of common classifiers and associated inability to receive sequence

based data as input was resolved through use of an LSTM based classification model. Although common classification models and feature extraction are commonly used on model data in literature, these practices were unsuccessful when applied to the MLSMP hardware data. This progression provided a clear depiction of the significance of sequence based information for the diagnostic task in real world hardware signals.

- Initial attempts for prognostics highlighted the limitations of LSTM and CNN time series prediction models and their inability to correlate past values of several input signals with future values of a desired response signal in time. These limitations were resolved using a LSTM sequence to one model, which received sequence input data for several signals and provided a singular numerical value as the response. Using this process the LSTM sequence to one model effectively predicted failure point for the fuel and cooling systems.

- Through the formation of a multi-model plant level diagnostic and prognostic framework, a clear correlation between input parameters and model response for both plant level leak detection and failure point prediction was formed. The selection of input parameters varied for best performance in the diagnostic task as compared to the best performance for the prognostics task. These variations highlight the importance of parameter selection for individual models or tasks as a critical driver to optimize prediction accuracy in large and complex coupled systems.

4. Unconventional control mitigation techniques are explored through a group of plant level hardware simulations using the MLSMP. This process illustrates the potential of real time control to improve operational resilience in a fault prone environment. Additional contributions under this group are as follows:

- Insight into the potential of energy storage for fault mitigation a critical mission operation.

- Application of an unconventional droop control strategy to mitigate support system faults and maintain operational capacity, in effort to improve operational resilience.

- Application of an unconventional load shedding practice to mitigate support system faults at a reduced operational capacity, in effort to improve operational resilience.

## 6.3 Recommendations for Future Work

The recommendations for future work are as follows:

- Investigate the application of prognostics and diagnostics on continuous low fidelity run to failure profiles for their performance in prognostic and diagnostic tasks. The work completed as part of this dissertation used windows of data to enable the high acquisition of data at a high sample rate, however, exploration showed that steady state data was the primary indicator for diagnostic and prognostic applications. Steady state data can be recorded continuously using a slower sample rate. A continuous run to failure dataset would provide the ability to predict across a continuous domain not limited by discrete sequence-points.

- Investigate alternative models and input signal processing methods for their application in the diagnostic and prognostic task. Additional signals include further analysis of power spectrum data and average power data. Alternative models include traditional statistics based data processing techniques, fuzzy classifiers, and variations in model configuration including a single AI driven model to perform all prognostic and diagnostic tasks through multiple model outputs. This work provided an initial extraction of signals and proposed a potential AI driven model. This work however, did not perform an exhaustive analysis on potential signals or models.

- Incorporation of additional failure modes for all systems within the laboratory scale ship machinery plant. This work provided an initial study of failure modes limited to common failures in the cooling and fuel systems. Failures to the electric plant, mission systems, propulsion system, and control system are some examples of failure modes not yet explored.

- Evaluate the potential of transfer learning by analyzing the performance of a model trained and tested on different plants within the MLSMP as well as the use of a digital twin to augment training data. This work compared prediction accuracy for two identical plants however did not evaluate the potential of transfer learning.

- Implementation of real time diagnostics and prognostics in conjunction with control mitigation strategies in the laboratory setting. This work illustrated the potential for control based fault mitigation techniques with knowledge of system health but did not incorporate a diagnostic or prognostic framework into a real time application for fault mitigation. The diagnostics and prognostics completed in this dissertation were all completed offline.

- Evaluation of other existing diagnostics and prognostics approaches in combination with the methods studied in the present research.

# BIBLIOGRAPHY


[1] E. T. Almquist, T. J. McCoy, S. A. Olson, A. Kerkmaz, M. Williamson, and H. Zayko, "Hardware modeling of diesel engine fuel system failure modes and coupled shipboard dynamics," in *2023 IEEE Electric Ship Technologies Symposium (ESTS)*, 2023, pp. 290–298.

[2] S. A. Olson, T. J. McCoy, M. Williamson, H. Zayko, and A. Kerkmaz, "Hardware simulation of a multiphysics ship machinery system for autonomous machinery research," in *2023 IEEE Electric Ship Technologies Symposium (ESTS)*, 2023, pp. 284–289.

[3] O. F. Eker, F. Camci, and I. K. Jennions, "Physics-based degradation modelling for filter clogging," in *PHM Society European Conference*. https://doi.org/10.36001/phme.2014.v2i1.1478, 2014.

[4] M. M. Abaei, R. Hekkenberg, A. BahooToroody, O. V. Banda, and P. van Gelder, "A probabilistic model to evaluate the resilience of unattended machinery plants in autonomous ships," *Reliability Engineering & System Safety*, vol. 219, p. 108176, 2022. [Online]. Available: https://www.sciencedirect.com/science/article/pii/S0951832021006608

[5] A. BahooToroody, M. M. Abaei, O. V. Banda, P. Kujala, F. De Carlo, and R. Abbassi, "Prognostic health management of repairable ship systems through different autonomy degree; from current condition to fully autonomous ship," *Reliability Engineering & System Safety*, vol. 221, p. 108355, 2022. [Online]. Available: https://www.sciencedirect.com/science/article/pii/S0951832022000345

[6] A. BahooToroody, M. M. Abaei, O. Valdez Banda, J. Montewka, and P. Kujala, "On reliability assessment of ship machinery system in different autonomy degree; a bayesian-based approach," *Ocean Engineering*, vol. 254, p. 111252, 2022. [Online]. Available: https://www.sciencedirect.com/science/article/pii/S0029801822006473

[7] S. Olson, "Alternative architecture analysis for design of resilient unmanned marine propulsion and energy generation systems." Master's thesis, University of Michigan, Ann Arbor, MI, May 2021.

[8] B. Finley and E. A. Schneider, "ICAS: the center of diagnostics and prognostics for the United States Navy," in *Component and Systems Diagnostics, Prognosis, and Health Management*, P. K. Willett and T. Kirubarajan, Eds., vol. 4389, International

Society for Optics and Photonics. SPIE, 2001, pp. 186 – 193. [Online]. Available: https://doi.org/10.1117/12.434237

[9] G. D. Blyden, "Modeling ship air conditioning maintenance costs using the integrated condition assessment system (icas)," in *NAVAL POSTGRADUATE SCHOOL MONTEREY CA GRADUATE SCHOOL OF BUSINESS AND PUBLICPOLICY*, 2002.

[10] N. R. Joshi, A. D. Ramirez, D. W. Brock, and S. D. Russell,, "Monitoring of high-power microwave tube systems using the integrated condition assessment system (icas)," in *SPACE AND NAVAL WARFARE SYSTEMS COMMANDSAN DIEGO CA*, 2002.

[11] A. Aboulian, D. H. Green, J. F. Switzer, T. J. Kane, G. V. Bredariol, P. Lindahl, J. S. Donnal, and S. B. Leeb, "Nilm dashboard: A power system monitor for electromechanical equipment diagnostics," *IEEE Transactions on Industrial Informatics*, vol. 15, no. 3, pp. 1405–1414, 2019.

[12] J. W. O'Connell, "Shipboard fault detection, marine micro-grid power diagnostics and vessel ventilation monitoring," Ph.D. dissertation, Massachusetts Institute of Technology, 2021.

[13] P. A. Lindahl, D. H. Green, G. Bredariol, A. Aboulian, J. S. Donnal, and S. B. Leeb, "Shipboard fault detection through nonintrusive load monitoring: A case study," *IEEE Sensors Journal*, vol. 18, no. 21, pp. 8986–8995, 2018.

[14] P. Lindahl, S. Leeb, J. Donnal, and G. Bredariol, "Noncontact sensors and nonintrusive load monitoring (nilm) aboard the uscgc spencer," in *2016 IEEE AUTOTESTCON*, 2016, pp. 1–10.

[15] Z. Chang, W. Yuan, and K. Huang, "Remaining useful life prediction for rolling bearings using multi-layer grid search and lstm," *Computers and Electrical Engineering*, vol. 101, p. 108083, 2022. [Online]. Available: https://www.sciencedirect.com/science/article/pii/S004579062200338X

[16] A. Zollanvari, K. Kunanbayev, S. Akhavan Bitaghsir, and M. Bagheri, "Transformer fault prognosis using deep recurrent neural network over vibration signals," *IEEE Transactions on Instrumentation and Measurement*, vol. 70, pp. 1–11, 2021.

[17] C. Cheng, G. Ma, Y. Zhang, M. Sun, F. Teng, H. Ding, and Y. Yuan, "A deep learning-based remaining useful life prediction approach for bearings," *IEEE/ASME Transactions on Mechatronics*, vol. 25, no. 3, pp. 1243–1254, 2020.

[18] A. Stetco, A. Mohammed, S. Djurović, G. Nenadic, and J. Keane, "Wind turbine operational state prediction: towards featureless, end-to-end predictive maintenance," in *2019 IEEE International Conference on Big Data (Big Data)*, 2019, pp. 4422–4430.

[19] A. Saxena, K. Goebel, D. Simon, and N. Eklund, "Damage propagation modeling for aircraft engine run-to-failure simulation," in *2008 International Conference on Prognostics and Health Management*, 2008, pp. 1–9.

[20] W. Xu, Q. Jiang, Y. Shen, Q. Zhu, and F. Xu, "New rul prediction method for rotating machinery via data feature distribution and spatial attention residual network," *IEEE Transactions on Instrumentation and Measurement*, vol. 72, pp. 1–9, 2023.

[21] C. Chen, J. Shi, M. Shen, L. Feng, and G. Tao, "A predictive maintenance strategy using deep learning quantile regression and kernel density estimation for failure prediction," *IEEE Transactions on Instrumentation and Measurement*, vol. 72, pp. 1–12, 2023.

[22] T. Meng, X. Jing, Z. Yan, and W. Pedrycz, "A survey on machine learning for data fusion," *Information Fusion*, vol. 57, pp. 115–129, 2020. [Online]. Available: https://www.sciencedirect.com/science/article/pii/S1566253519303902

[23] M. G. Kapteyn and K. E. Willcox, "From physics-based models to predictive digital twins via interpretable machine learning," *arXiv preprint arXiv:2004.11356*, 2020.

[24] *On Digital Twin Condition Monitoring Approach for Drivetrains in Marine Applications*, ser. International Conference on Offshore Mechanics and Arctic Engineering, vol. Volume 10: Ocean Renewable Energy, 06 2019. [Online]. Available: https://doi.org/10.1115/OMAE2019-95152

[25] Y. Tan, C. Niu, H. Tian, and J. Zhang, "A digital twin based design of the semi-physical marine engine room simulator for remote maintenance assistance," in *2021 5th International Conference on Vision, Image and Signal Processing (ICVISP)*, 2021, pp. 137–141.

[26] J. Walker, A. Coraddu, L. Oneto, and S. Kilbourn, "Digital twin of the mooring line tension for floating offshore wind turbines," in *OCEANS 2021: San Diego – Porto*, 2021, pp. 1–7.

[27] S. Eriksen and M. Lützen, "The impact of redundancy on reliability in machinery systems on unmanned ships," *WMU Journal of Maritime Affairs*, vol. 21, no. 2, pp. 161–177, 2022. [Online]. Available: https://doi.org/10.1007/s13437-021-00259-7

[28] I. Errandonea, S. Beltrán, and S. Arrizabalaga, "Digital twin for maintenance: A literature review," *Computers in Industry*, vol. 123, p. 103316, 2020. [Online]. Available: https://www.sciencedirect.com/science/article/pii/S0166361520305509

[29] J. C. Neely, S. Pekarek, S. Glover, J. Finn, O. Wasynczuk, and B. Loop, "An economical diesel engine emulator for micro-grid research," in *International Symposium on Power Electronics Power Electronics, Electrical Drives, Automation and Motion*, 2012, pp. 175–179.

[30] C. J. Doktorcik, "Modeling and simulation of a hybrid ship power system," Ph.D. dissertation, Purdue University, 2011, copyright - Database copyright ProQuest LLC; ProQuest does not claim copyright in the individual underlying works; Last updated - 2023-03-04. [Online]. Available: https://proxy.lib.umich.edu/login?url=https://www.proquest.com/dissertations-theses/modeling-simulation-hybrid-ship-power-system/docview/903968276/se-2

[31] H. Akbarian, P. Pillay, and L. Lopes, "Design of a power electronic emulator for parallel operation of renewable energy resources in microgrids," in *2015 IEEE International Electric Machines & Drives Conference (IEMDC)*, 2015, pp. 1532–1537.

[32] D. C. Aliprantis, B. T. Kuhn, S. D. Sudhoff, and T. J. McCoy, "A detailed synchronous machine model," *SAE Transactions*, vol. 111, pp. 778–788, 2002. [Online]. Available: http://www.jstor.org/stable/44718488

[33] M. Torres and L. Lopes, "Inverter-based diesel generator emulator for the study of frequency variations in a laboratory-scale autonomous power system," *Energy and Power Engineering*, vol. 05, pp. 274–283, 01 2013.

[34] H. Akbarian, "Design of a power electronics based diesel engine generator emulator for study of microgrid related applications," Ph.D. dissertation, Concordia University, 2015.

[35] A. L. Gattozzi, J. D. Herbst, R. E. Hebner, J. A. Blau, K. R. Cohn, W. B. Colson, J. E. Sylvester, and M. A. Woehrman, "Power system and energy storage models for laser integration on naval platforms," in *2015 IEEE Electric Ship Technologies Symposium (ESTS)*, 2015, pp. 173–180.

[36] A. Manohar, "Enabling self-adaptive health monitoring systems on crewless vessels via a network of tensor networks," Ph.D. dissertation, University of Michigan, 2024.

[37] Manohar, A., Arrigan, C.W., Singer, D.J., Olson, S.A., McCoy, T.J. (2023), "A novel through-life tensor network and ontological commitment inspired approach for a self-adaptive health monitoring system for crewless vessels," in *Proceedings of the 10th International Conference on Computational Methods in Marine Engineering , Madrid, Spain.*, 2023.

[38] Z. Ding, S. K. Srivastava, D. A. Cartes, and S. Suryanarayanan, "Dynamic simulation-based analysis of a new load shedding scheme for a notional destroyer-class shipboard power system," *IEEE Transactions on Industry Applications*, vol. 45, no. 3, pp. 1166–1174, 2009.

[39] J. Momoh, J. Zhu, and S. Kaddah, "Optimal load shedding study of naval-ship power system using the everett optimization technique," *Electric Power Systems Research*, vol. 60, no. 3, pp. 145–152, 2002. [Online]. Available: https://www.sciencedirect.com/science/article/pii/S0378779601001614

[40] B. Papari, R. Cox, C. S. Edrington, G. Ozkan, P. H. Hoang, and N. Deb, "Enhancement of energy management in the shipboard power systems based on recursive distributed load shedding model," in *2019 IEEE Electric Ship Technologies Symposium (ESTS)*, 2019, pp. 605–611.

[41] Z. Ding, S. Srivastava, and D. Cartes, "Expert system based dynamic load shedding scheme for shipboard power systems," in *Conference Record of the 2006 IEEE Industry Applications Conference Forty-First IAS Annual Meeting*, vol. 3, 2006, pp. 1338–1344.

[42] H. Liu, Y. Yang, X. Wang, P. C. Loh, F. Blaabjerg, W. Wang, and D. Xu, "An enhanced droop control scheme for resilient active power sharing in paralleled two-stage pv inverter systems," in *2016 IEEE Applied Power Electronics Conference and Exposition (APEC)*, 2016, pp. 1253–1260.

[43] M. M. S. Khan and M. O. Faruque, "Energy storage management for mvdc power system of all electric ship under different load conditions," in *2017 IEEE Electric Ship Technologies Symposium (ESTS)*, 2017, pp. 192–199.

[44] Z. Jin, L. Meng, J. M. Guerrero, and R. Han, "Hierarchical control design for a shipboard power system with dc distribution and energy storage aboard future more-electric ships," *IEEE Transactions on Industrial Informatics*, vol. 14, no. 2, pp. 703–714, 2018.

[45] S. A. Olson and et al., "Prediction of seawater cooling system performance for autonomous vessels using artificial intelligence techniques," in *Proceedings of The Intelligent Ships Symposium*. ASNE, 2023.

[46] I. J. Karassik and T. McGuire, *Pump Operation at Off-Design Conditions*. Boston, MA: Springer US, 1998, pp. 558–591. [Online]. Available: https://doi.org/10.1007/978-1-4615-6604-5_22

[47] D. P. Kingma and J. Ba, "Adam: A method for stochastic optimization," *arXiv preprint arXiv:1412.6980*, 2014.

[48] MATLAB, *version 7.10.0 (R2010a)*. Natick, Massachusetts: The MathWorks Inc., 2010.

[49] E. M. Brocken, "Improving the reliability of ship machinery - a step towards unmanned shipping," Delft University of Technology, Tech. Rep., 2016. [Online]. Available: http://repository.tudelft.nl/

[50] M.-D. Wang, T.-H. Lin, K.-C. Jhan, and S.-C. Wu, "Abnormal event detection, identification and isolation in nuclear power plants using lstm networks," *Progress in Nuclear Energy*, vol. 140, p. 103928, 2021. [Online]. Available: https://www.sciencedirect.com/science/article/pii/S0149197021002882

[51] P. Wang, J. Zhang, J. Wan, and S. Wu, "A fault diagnosis method for small pressurized water reactors based on long short-term memory networks," *Energy*, vol. 239, p. 122298, 2022. [Online]. Available: https://www.sciencedirect.com/science/article/pii/S0360544221025469

[52] Chen, X., Zhang, B. & Gao, D., "Bearing fault diagnosis base on multi-scale cnn and lstm model," *J Intell Manuf*, vol. 32, p. 971–987, 2021. [Online]. Available: https://doi-org.proxy.lib.umich.edu/10.1007/s10845-020-01600-2

[53] K. Guo, N. Wang, D. Liu, and X. Peng, "Uncertainty-aware lstm based dynamic flight fault detection for uav actuator," *IEEE Transactions on Instrumentation and Measurement*, vol. 72, pp. 1–13, 2023.

[54] V. Veerasamy, N. I. A. Wahab, M. L. Othman, S. Padmanaban, K. Sekar, R. Ramachandran, H. Hizam, A. Vinayagam, and M. Z. Islam, "Lstm recurrent neural network classifier for high impedance fault detection in solar pv integrated power system," *IEEE Access*, vol. 9, pp. 32 672–32 687, 2021.

[55] X. Li, Q. Ding, and J.-Q. Sun, "Remaining useful life estimation in prognostics using deep convolution neural networks," *Reliability Engineering & System Safety*, vol. 172, pp. 1–11, 2018. [Online]. Available: https://www.sciencedirect.com/science/article/pii/S0951832017307779